DISSERTATIONES
CHIMICAE
UNIVERSITATIS
TARTUENSIS
210

MAARJA PAALO

Synthesis and characterization of novel carbon electrodes for high power density electrochemical capacitors

DISSERTATIONES CHIMICAE UNIVERSITATIS TARTUENSIS

210

DISSERTATIONES CHIMICAE UNIVERSITATIS TARTUENSIS

210

MAARJA PAALO

Synthesis and characterization of novel carbon electrodes for high power density electrochemical capacitors

UNIVERSITY OF TARTU
Press
1632

Institute of Chemistry, Faculty of Science and Technology, University of Tartu, Estonia.

The dissertation is accepted for the commencement of the degree of Doctor of Philosophy in Chemistry on February 9th, 2022, by the Council of Institute of Chemistry, University of Tartu.

Supervisors:	Prof. Enn Lust University of Tartu, Estonia
	PhD Thomas Thomberg University of Tartu, Estonia
	PhD Indrek Tallo
Opponent:	PhD Olivier Crosnier University of Nantes, France
Commencement:	29.03.2022 at 12:15. Auditorium 1020, Ravila 14a, Tartu

European Union
European Regional
Development Fund

Investing
in your future

ISSN 1406-0299
ISBN 978-9949-03-843-5 (print)
ISBN 978-9949-03-844-2 (pdf)

University of Tartu Press
www.tyk.ee

TABLE OF CONTENTS

1. LIST OF ORIGINAL PUBLICATIONS

I **M. Pohl**, H. Kurig, I. Tallo, A. Jänes, E. Lust, Novel sol-gel synthesis route of carbide-derived carbon composites for very high power density supercapacitors, Chemical Engineering Journal 320 (2017) 576–587.

II **M. Pohl,** I. Tallo, A. Jänes, T. Romann, E. Lust, Increasing the stability of very high potential electrical double layer capacitors by operando passivation, Journal of Power Sources 402 (2018) 53–61.

III **M. Paalo**, I. Tallo, T. Thomberg, A. Jänes, E. Lust, Enhanced power performance of highly mesoporous sol-gel TiC derived carbons in ionic liquid and non-aqueous electrolyte based capacitors, Journal of The Electrochemical Society 166 (13) (2019) A2887–A2895.

Author's contribution:

Paper I: Performed all the material synthesis, electrochemical measurements and analysis of data. Mainly responsible for the preparation of the manuscript.

Paper II: Performed all the material synthesis, electrochemical measurements and analysis of data. Mainly responsible for the preparation of the manuscript.

Paper III: Performed all the material synthesis, electrochemical measurements and analysis of data. Responsible for the preparation of the manuscript.

2. ABBREVIATIONS AND SYMBOLS

ac	alternating current
AN	acetonitrile
BET	Brunauer-Emmett-Teller
C	capacitance
C_{CC}	specific capacitance calculated from constant current charge/discharge data
C_m	specific capacitance
$C_{m;CV}$	specific capacitance calculated from cyclic voltammetry data
C_p	parallel capacitance
C_s	series capacitance
CCCD	constant current charge/discharge method
CDC	carbide derived carbon
CNT	carbon nanotube
CV	cyclic voltammetry
ΔE	cell potential
E	energy
$E_{ac}(t)$	*ac* potential
$E_{0,ac}$	*ac* potential amplitude
E_{in}	energy density stored/accumulated
E_{max}	maximum amplitude of *ac* potential
E_{out}	energy density released
EDLC	electrical double-layer capacitor
EIS	electrochemical impedance spectroscopy
$EMImBF_4$	1-ethyl-3-methylimidazolium tetrafluoroborate
Et_3MeNBF_4	triethylmethylammonium tetrafluoroborate
ESR	equivalent series resistance
f	frequency in Hz
f_{int}	frequency of interception points
F	Farad
g	gram
$I_{ac}(t)$	*ac* current
$I_{0,ac}$	*ac* current amplitude
i	current density
j	imaginary number
m	mass
NLDFT	non-local density functional theory
P	power
PTFE	polytetrafluoroethylene
PVDF	polyvinylidene fluoride
$P(\omega)$	active power
p/p_0	relative pressure
q	charge

$Q(\omega)$	reactive power
R_p	parallel resistance
R_s	high frequency series resistance
R_{pore}	pore resistance
RTIL	room temperature ionic liquid
SAIEUS	Solution of Adsorption Integrated Equation Using Splines
sgTiC	titanium carbide synthesized by sol gel method
S_{DFT}	specific surface area
SC	supercapacitor
SEM	scanning electron microscopy
$S(\omega)$	complex power
t	time
$TBABF_4$	tetra-n-butylammonium tetrafluoroborate
TiC	titanium carbide
TiC-CNT	titanium carbide and carbon nanotube composite
v	potential scan rate
XRD	X-ray diffraction
XRF	X-ray fluorescence
Z	impedance
Z'	real part of impedance
Z''	imaginary part of impedance
wt%	weight percentage
σ	charge density
η_{coul}	coulombic efficiency
η_{en}	energy efficiency
θ	phase angle between voltage and current
τ_R	characteristic time constant
Ω	ohm
ω	angular frequency

3. INTRODUCTION

In recent years, the demand for versatile energy storage systems has risen quite fast. The environmental impact of energy consumption for some regions has additionally increased the necessity for new energy storage devices with high power and energy densities needed for the stable integration of sustainable, but fluctuating photovoltaic, wind, and concentrated solar power generation systems into very large-scale electricity grids [1–5].

Modern electrical energy conversion/storage systems can be divided into four groups like supercapacitors, batteries, electrolysers, and fuel cells. Supercapacitors and batteries are more suitable for so-called short- and medium-term electricity storage. Electrolysers and fuel cells combined can be used for the long term and even for seasonal electricity storage and regeneration of electricity [1–3,6–15].

The commercialization of supercapacitors vastly increased due to their extremely high power delivery characteristics that fill the gap between the dielectric capacitors and traditional batteries. Supercapacitors complement batteries and fuel cells in applications where high power and energy densities are important such as peak power sources, hybrid electric vehicles, space devices, digital communication devices, mobile phones, and industrial applications [6–9,16–19].

Supercapacitors have gained much attention because they have high specific capacitance, very long cycle life, very high power density, and very low maintenance costs [6,20]. The energy storage characteristics of supercapacitors are largely determined by the electrical capacitance, system resistance, and maximum cell potential all dependent on electrolyte properties used. Energy density is proportional to capacitance and is highly dependent on the micro-mesoporous structure of electrodes used [6–12,17,21,22].

One of the most used electrode materials in supercapacitors are different porous carbon materials, like activated carbons, carbon aerogels, carbon cloth, carbon black, etc. as well as carbide derived carbons. The unique porous structure of carbide derived carbon with the narrow pore size distribution and a possibility to fine-tune the pore size and volume has given them great potential as electrode materials in supercapacitors [9,17,23–27].

One limiting factor in achieving high energy and power density is the moderate working cell potential of different electrolytes that can be applied for supercapacitors [16,28–30].

To achieve an excellent performance of a supercapacitor it is important to optimise the characteristics of components like electrodes and electrolytes. For electrodes, it is important to tune the micro-mesoporosity, pore size distribution, and thickness. For the used electrolyte it is important that it has a high electrochemical window and that the electrolyte ions suit the selected electrode material and separator.

Sol-gel technology is a versatile technology, making it possible to produce a wide variety of materials like powders, fibers, coatings, and monoliths [31,32]. In the sol-gel method CNTs, dispersion, and liquid matrix precursors are mixed at a molecular level which allows homogeneous CNTs dispersion and a molecular interaction with the matrix [33,34].

The main results and research directions of this work are:

1. Modify the sol-gel synthesis methods for preparation of well developed micro- and mesoporous electrodes with optimal hierarchical structure. The sol-gel method gives additional mesoporosity to the initial carbide material that results also in the derived carbon material, unlike when the commercially synthesized titanium carbide is used as a precursor for the chlorination reaction to synthesize carbon material.
2. Development of operando activation and passivation methods for future enlargement of ideal polarizability region of electrodes and therefore electrical double layer supercapacitors power and energy densities.
3. Application of modified novel porous carbon electrodes for preparation of high power and energy density symmetrical ideally polarizable electrical double layer supercapacitors and detailed testing and characterization of completed two electrode cells using various physical and electrochemical methods.

4. LITERATURE OVERVIEW

4.1. Sol-gel process

4.1.1. Synthesis of transition metal oxide by sol-gel process

The sol-gel process is a wet chemical method used for the synthesis of different oxide materials. The technology can also be used in the preparation of non-oxide materials like nitrides, carbides, fluorides, sulphides, etc. The sol-gel process involves the generation of colloidal suspensions ("sols") which then are subsequently converted to viscous gels and after thermal treatment are converted to solid materials, for example, different powders and films (Fig. 1) [31, 35–38].

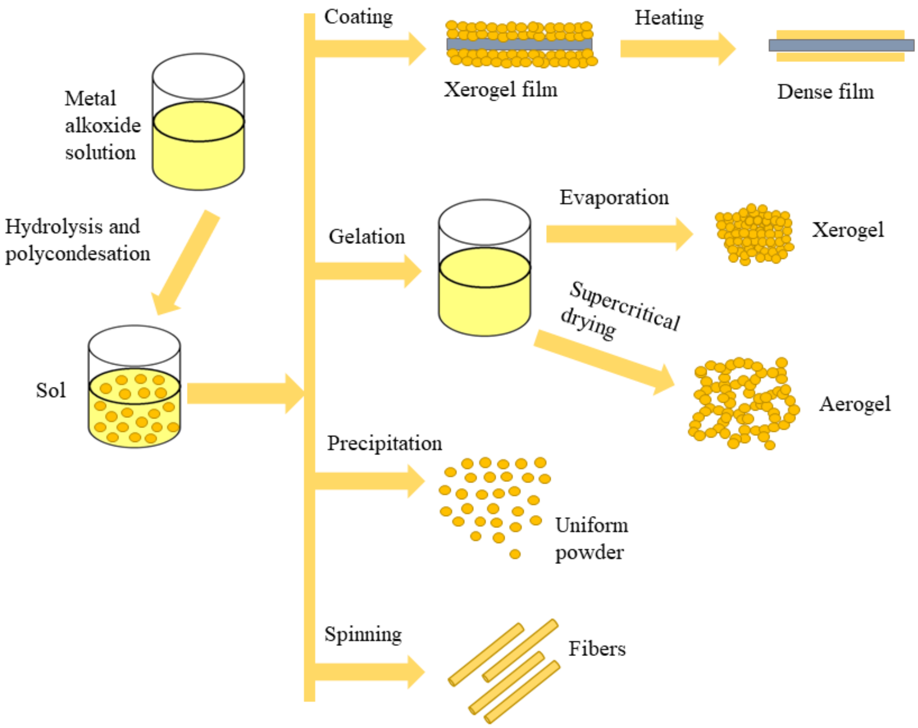

Figure 1. Sol-gel synthesis.

Most used precursors are different metal alkoxides M-$(OR)_n$ that go under hydrolysis and polycondensation reactions. In the hydrolysis process a reactive metal hydroxy group M-$(OH)_n$ is generated according to Reaction 1:

$$M\text{-}(OR)_n + nH\text{-}OH \rightarrow M\text{-}(OH)_n + nR\text{-}OH. \quad (1)$$

Polycondensation will start as soon as hydroxo groups are generated and three competitive mechanisms (depending on the chemical reaction conditions) occur: alcoxolation, oxolation, and olation. Alcoxolation (Reaction 2) occurs when the alkoxy precursor reacts with the hydrolysed precursor:

$$M\text{-}OH + M\text{-}OR \rightarrow M\text{-}O\text{-}M + R\text{-}OH, \quad (2)$$

oxolation (Reaction 3) occurs when hydrolysed precursor reacts with other hydrolysed precursors:

$$M\text{-}OH + M\text{-}OH \rightarrow M\text{-}O\text{-}M + H\text{-}OH, \quad (3)$$

and olation (Reaction 4) occurs when bridging hydroxo groups are formed through the elimination of a solvent molecule:

$$M\text{-}OH + M \rightarrow M\text{-}O\text{-}M + R\text{-}OH. \quad (4)$$

Olation occurs when the full coordination of the metal atom is not satisfied in the alkoxide formation. As a result of the three condensation mechanisms oligo- and polymeric chains $(\text{-M-O-})_n$ are formed and this leads to the formation of a 3D network. Dominating mechanism depends on the pH, water/alkoxide ratio, the concentration of the alkoxide, and the reaction temperature. Also, it is important to control the hydrolysis and polycondensation reactions to produce a homogeneous metal oxide network. For the metal alkoxide to go under full polycondensation reaction, the compound used for the carbon source must have at least two or more hydroxy groups. After the processes of hydrolysation and condensation, the gelation process takes place, where the formation of a 3D-network of sol particles will occur. The gelation process begins with the interaction of the particles in the sol with each other and forming clusters that aggregate until a 3D-network, also called gel, is formed. The interaction can occur either via hydrogen bonding or via coalescence with the formation of M–O–M bridges. After the gelation process, the forming of the gel network can be dried to form a porous xerogel [31,32,35–41].

4.1.2. Synthesis of carbide precursor by sol-gel process

For synthesizing metal carbide precursor xerogel by sol-gel process, the metal alkoxide polycondensation is carried out by transesterification of the OR groups in metal alkoxide $M\text{-}(OR)_n$ by adding ligands which act as bridging ligands. For bridging ligands, diols or other chemicals are used that have two or more reactive OH groups [42,43]. The transesterification (Reaction 5) followed by poly-condensation (Reaction 6) of $M(OR)_n$ is shown in sequent reactions as follows:

$$M\text{-}(OR)_n + HO\text{-}X\text{-}OH \rightarrow (OR)_{n\text{-}1}\text{-}M\text{-}O\text{-}X\text{-}OH + ROH \quad (5)$$

$$(OR)_{n-1}\text{-M-O-X-OH} \rightarrow \text{-}\left[\text{O-M}(OR)_{n-2}\text{O-X-}\right]_m + ROH \quad (6)$$

The transesterification process is necessary to increase the carbon content of carbon in precursor gel for carbothermal reduction to synthesize stoichiometry metal carbides [36].

After the polycondensation reactions, the solvent is evaporated, and dried powder is obtained. This is followed by sequential heat treatments. Firstly, the pyrolysis of the dried gel results in metal oxide and carbon mixture. Final metal carbide is obtained via carbothermal reduction (in inert atmosphere) reaction of the resulting oxide and carbon according to Reaction 7 [44,45]:

$$MeO_n + (n+1)C \rightarrow MeC + nCO. \quad (7)$$

4.2. Electrical double layer theory

An electrical double layer forms whenever two conducting phases meet at an interface. Usually, one of the phases is positively charged and the other phase is balanced by a counter charge so it is negatively charged [46].

There are many different electrical double layer models that include Helmholtz, Gouy-Chapman, Stern, Grahame, and more modern models like Amokrane-Badiali and Kornyshev-Vorotyntsev models.

The term "electrical double layer" comes from the Helmholtz model that he created in 1853. In the Helmholtz model, two layers of charges are formed at the interface of electrode and solution (electrolyte) having opposite polarity and these layers are separated by a short distance (order of few angstroms). According to the Helmholtz model, the variation of the potential of the double layer with distance into the solution is linear and the electrical double layer leads to a difference of potential between the solid electrode and the liquid (electrolyte) phase. There are a few limitations that the Helmholtz model has. Firstly, it does not take into account that in a solution (due to the thermal motion of liquid molecules) there may not be a rigid array of charges at the interface. The model assumes a fixed layer of oppositely charged ions in a solution. Secondly, the Helmholtz model predicts a constant capacitance for the electrical double layer. Experimentally it is found that the capacitance is not constant with the cell potential. And thirdly, it does not consider the different properties of the double layer with concentration of electrolyte and temperature [6,17,47,48].

The Gouy-Chapman theory is an expansion of the Helmholtz model that was proposed in the early 1900s. Gouy-Chapman's model considers that at the interface the electrical double layer is not fixed but there is a diffuse double layer. The diffuse layer means that one layer is fixed on the electrode and the oppositely charged layer is diffused in the electrolyte (the ions are spread out into the solution). The potential change from one layer to another is not linear but exponential. The Gouy-Chapman model considers the properties of double layer change with electrolyte concentration and temperature and that the capacitance of the double layer changes with the electrode potential. Thus, the capacitance in the double layer is not constant and it depends upon the applied potential across the electrodes and the concentration of the electrolyte [6,17,47,48].

The Stern theory combines the essentials of Helmholtz and Gouy-Chapman theories and was proposed in 1924. According to Stern theory, the electrical double layer has two layer regions. One layer is fixed at the electrode surface (Helmholtz layer) and the oppositely charged layer (diffused layer) consists of two parts. The first part remains almost fixed to the electrode (approximately of single ion thickness) and forms a compact layer near the electrode and the second part is distributed through the electrolyte and is thought to move freely along with the liquid. The variation of potential in the Stern model is that in the first layer (Helmholtz layer) there is a linear change in the potential but in the diffuse layer the potential change is exponential. The capacitance of the interface depends on the electrode potential and the concentration of electrolyte solution [6,17,47,48].

More modern double layer models developed by Amokrane-Badiali and Kornyshev-Vorotyntsev are taking into account that the metal electrodes as well carbon electrodes are not ideal conductors (so called ideal metals). There is a potential drop inside of the electrode surface layer (a thin film of a metal surface) depending on the electronic characteristics of the metal, i.e. on the metal dielectric constant and the effective mass of the electron as well as on the number of electrons in the volume of the metal unit [49–52].

4.3. Supercapacitors

The first electrochemical capacitor or so called supercapacitor device was patented by General Electric's H.I. Becker in 1957 but the first theory about the electrical energy storage at the electrode|electrolyte interface goes back to the late 1800s as mentioned in the previous chapter [53].

Supercapacitors are one of the main energy storage devices that also include conventional capacitors, batteries, and fuel cells. Supercapacitors fill the gap between batteries, that have a high energy density, and electrolytic capacitors, that have high power density (Fig. 2) [8,17,54].

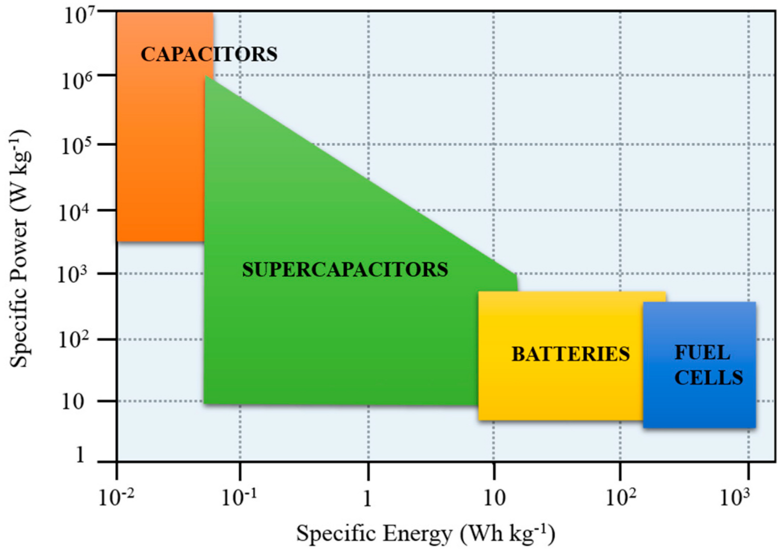

Figure 2. Ragone plot for different energy devices [8,55].

Depending on their charge storage mechanism, electrochemical capacitors can be subcategorized in three different ways: electrical double layer capacitors (EDLCs), pseudocapacitors, and hybrid electrochemical capacitors. When the EDLC is connected to a power supply, the surface of electrodes is charged and attracts ions of the opposite charge form together an electrical double layer, where energy is stored (Fig. 3). The major difference of EDLCs compared to other types of electrochemical capacitors like pseudo and hybrid capacitors is that there are no redox reactions involved in the energy storage process, and the charges are stored only at the surface of the carbon electrode electrostatically. Pseudocapacitors store charges with fast and reversible faradic redox reactions and hybrid electrochemical supercapacitors use both electrical double layer and faradic mechanisms to store charges [5,6,17,20,28,48,56–61].

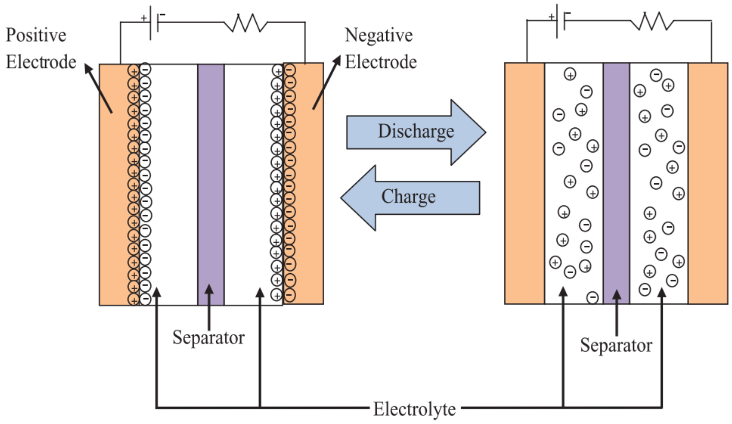

Figure 3. Mechanism of charge and discharge process of EDLC [61].

Supercapacitors are mainly used to generate high power pulses. The power density or the charge/discharge time for EDLCs will be determined by how fast the ions transport within the electrode material takes place [61]. The power density [56] of the EDLC cell can be expressed as Eq. 1:

$$P = \frac{(\Delta E)^2}{4R_s} \tag{1}$$

where R_s is the equivalent series resistance (ESR) and ΔE is the maximal cell potential. To see how long the power lasts, the energy density is also calculated according to Eq. 2:

$$E = \frac{C(\Delta E)^2}{2} \tag{2}$$

where C is the series capacitance and ΔE is the maximal cell potential.

The main technical specifications besides energy and power density that electrochemical supercapacitors have and what we must consider as a whole set to get a good performance of an EDLC are: capacitance, equivalent series resistance, cycle-life, self-discharge rate, and thermal stability [10,11].

Supercapacitor consists of four main elements: electrodes, electrolyte, separator (or membrane), and casing. Since those components each make up the overall price of the device, it is important to modify all components together to get the best performance and the biggest price reduction. The biggest share of the cost is usually the electrode materials (28%) and the electrolyte (27%). Separator makes up to 23% of the overall cost and casing and production 22% [60]. In the next chapters, the 3 main elements are viewed.

4.3.1. Carbide derived carbon as an electrode material

Carbide derived carbons (CDCs) are porous carbons that are synthesized via halogenation (commonly chlorination with Cl_2 gas) of metal or nonmetal carbides. The final structure of the carbon can be ordered or disordered which depends on the temperature of the halogenation reaction and the initial carbide used. The size of the pores in the final CDC is influenced by the distribution of carbon atoms in the initial carbide, the amount of chlorides formed and chlorine trapped in the CDC, the size of the chloride molecule, the presence of catalytic particles, and the effect of optional post-treatments, such as activation, or mild oxidation. Secondly, there is a temperature effect on the halogenation reaction kinetics and on the pore size distribution of the final carbon. Increasing CDC synthesis temperature generally leads to larger pores and eventually to a broader distribution of pore sizes. The optimum synthesis temperature for large specific surface area CDC would correspond to the conditions when all the pores formed in the CDC are open and large enough to be accessible to inert gases and are free from contaminants. Thirdly, CDCs final porosity is also affected by the porosity of the initial carbide. CDCs synthesized from carbide single crystals do not possess macroporosity, unlike carbons produced from porous sintered samples of carbides having initial porosity up to 16% by volume. This means that the meso-and microporosity in the initial carbide does not change noticeably during the chlorination process and can be controlled by controlling the porosity of carbides. Thus, the total volume and characteristic dimensions of meso- and nanopores can be predicted and achieved by the selection of carbides, and variation of the chlorination process parameters. For example, synthesizing the initial carbide via the sol-gel method gives the initial carbide additional porosity which also results in the final micro- and mesoporous carbon material. Micro- and mesoporous CDC with open pores is a nearly ideal material for high power density supercapacitor devices [25,62–64].

4.3.2. Electrolytes

There are mainly three types of electrolytes used in supercapacitors: aqueous, organic, and ionic liquid electrolytes. All these electrolytes have their advantages and disadvantages. Aqueous electrolytes have high ionic conductivity but the disadvantage is the small electrochemical thermodynamic stability window of water (up to 1.23 V), thus high energy and power densities (that correspond to a voltage that can be applied to the supercapacitor) are hard to achieve. On the other hand, aqueous electrolytes are the cheapest and since electrolyte cost is substantial to the overall cost of the supercapacitor, then it is another advantage.

The second most common electrolyte used is an organic electrolyte (salt + organic solvent). Organic electrolytes have a larger electrochemical window (up to 3 – 3.5 V) but they have lower conductivity and are pricier than aqueous electrolytes.

The third electrolyte type applied and studied is ionic liquids. The ionic liquid electrolytes have the largest electrochemical window (up to 4 – 5 V) but have high viscosity and low ionic conductivity and the cost of some room temperature ionic liquids is very high [56,60,65].

4.3.3. Separators

To prevent the short circuiting of the supercapacitor, the electrodes need to be physically separated. For that, electrically insulating separator material is used. Although it must be porous so the ions of the electrolyte can pass through the separator for charge compensation during charging and discharging. The most used separators are made from porous polymeric membranes, such as cellulose, polypropylene, polyvinylidene fluoride (PVDF), and polytetrafluoroethylene (PTFE). Also, some other qualities that the separator must possess are chemical inertness to solvents and salts, thermal stability, good wettability, mechanical stability, and low weight and volume [60,66].

4.4. Physical characterization methods

4.4.1. X-ray diffraction and Raman spectroscopy

To characterize EDLC electrode materials, widely used techniques are X-ray diffraction and Raman spectroscopy analysis methods.

X-ray diffraction (XRD) is a non-destructive technique for characterizing crystalline materials. XRD gives information about phases, structures, and their parameters, like grain size, crystallinity, and crystal defects. XRD patterns can be used to determine the deviation of a particular component from its ideal composition and/or structure. XRD peaks are produced by constructive interference of a monochromatic beam of X-rays scattered at specific angles from each set of lattice planes in the sample. The peak intensities are determined by the atomic positions within the lattice planes. For EDLC electrodes, amorphous carbon materials are used, therefore the XRD pattern measured for non-crystalline materials (amorphous solids), is essentially continuous in appearance, hence no solid peaks are determined but more of continuous bumps are shown in the diffractogram. However, for porous carbon materials synthesized from carbides, a typical diffractogram shows continuous wide diffraction peaks 002 ($2\theta \sim 26°$) and 100/101 ($2\theta \sim 43°$). The 002 peak corresponds to parallel-oriented graphite layers and 100/101 peak characterizes the size of the graphite layer [67–71].

Raman spectroscopy is an optical, vibrational spectroscopic technique that provides detailed information about molecular composition and molecular structure of material under examination. For disordered amorphous carbon materials, Raman spectra demonstrate two peaks which are typical for amorphous carbon materials including carbons synthesized from carbides. The first peak is so-called G-peak at 1590 cm^{-1} and the second is so-called D-peak at 1350 cm^{-1} [65,72–75].

4.4.2. Gas sorption method

The gas sorption method is used to analyse the porosity of the electrode materials. IUPAC classification of pore sizes are as follows: micropore diameter is below 2nm, mesopore diameter varies from 2 to 50 nm and macropores have diameter above 50 nm. Pores can be opened and/or closed. When the material has closed pores, then that means that no substances can get into those pores. For CDCs pore structure, the most used method is low-temperature nitrogen sorption. The resulting isotherm is analysed and applying an appropriate theory, we can conclude if the material is micro-, meso- or macroporous. For more precise characterization CO_2 and Ar are also used and the isotherm and pore size distribution analysis is a combined method of two or more gases [65,76–78].

For comparison of different materials, quantitative analysis of isotherm data is required and for this, several methods are used. The most common methods are Brunauer-Emmett-Teller (BET) and non-local density functional theory (NLDFT). The NLDFT is well suited for the analysis of micro- and mesoporous materials. In recent years, Micromeritics company has developed SAIEUS (Solution of Adsorption Integrated Equation Using Splines) program that uses the 2D-NLDFT model, that tries to take into account the energetic heterogeneity of the carbon surface [65,77,79–81].

4.5. Electrochemical characterization methods

4.5.1. Cyclic voltammetry

Cyclic voltammetry (CV) is very commonly used to characterize the behaviour of an electrochemical cell conducting or an electrode material characteristics if a three electrode system is used. Cyclic voltammetry measures the current that flows through an electrochemical cell as the voltage is swept over a voltage range. In CV measurements the voltage is swept between the two limiting potentials and a pair of sweeps in opposite directions is called a cycle. The scan rate shows the rate of voltage change over time during each of these cycles. In the case of an ideal EDLC, the C, ΔE plot shape is rectangular and it is symmetrical relative to the zero current line [82–85].

The total capacitance of a two-electrode cell can be calculated from the CV data (current density vs voltage curves) according to Eq. 3:

$$C = \frac{I}{v} \tag{3}$$

where I is current in amperes and $v = d\Delta E/dt$ is the potential scan rate. With this equation we assume that the total capacitance of the cell is constant, a series resistance is very small $R_s \rightarrow 0$, and therefore the current $I \rightarrow 0$. For more correct analysis the medium capacitance values can be calculated over the cell potential range ΔE using the integrated total charge density (σ) values, obtained according to Eq. 4:

$$\sigma = \int_{\Delta E_1}^{\Delta E_2} i(\Delta E)dt \equiv \int_{\Delta E_1}^{\Delta E_2} i(\Delta E)\frac{d(\Delta E)}{E}. \tag{4}$$

This equation can be used only within the region of moderate cell potential scan rates (if the values of current density i are small) as only in these conditions the potential drop due to cell resistance $R \rightarrow 0$ is negligible. When the electrochemical cell consists of a symmetrical two-electrode system (electrodes are in series) then the specific capacitance C_m (F g^{-1}) can be calculated with the following Eq. 5:

$$C_m = \frac{2C}{m} \tag{5}$$

where m is the mass of the carbon material in one electrode. For this equation, the positively and negatively charged electrodes have the same capacitance at fixed ΔE [22,63,86–90].

4.5.2. Constant current charge/discharge method

The constant current charge/discharge method (CCCD) is a standard technique to evaluate the performance and cycle life of EDLCs and batteries. In CCCD, the constant current density is applied to the electrochemical cell against time and the dependence of potential going through the cell is measured. For ideal EDLCs, the measured potential vs time plot is symmetrical and linear. The capacitance of the real cell is calculated by using the integration of the discharge curve:

$$C_{CC} = \frac{\int_{\Delta E_2}^{\Delta E_2} idt}{d(\Delta E)} \tag{6}$$

where i is the current density, dt is the change in time and ΔE is the change in cell potential [70,91].

The cycling efficiency (coulombic efficiency η_{coul}) is calculated as a ratio of charge densities released and accumulated during the discharging and charging steps. For more correct analysis energy efficiency (η_{en}) is calculated i.e., the CCCD curves are integrated, and the energy densities stored (E_{in}) and released (E_{out}) are calculated by Eq. 7:

$$E_{in,out} = i\int_{t(\Delta E_{min})}^{t(\Delta E_{max})} \Delta E(t)dt \quad (7)$$

where t is time in seconds and E_{max} and E_{min} are maximal and minimal cell potentials applied. The value of η_{en} is calculated according to Eq. 8:

$$\eta_{en} = \frac{E_{out}}{E_{in}} \cdot 100\% \quad (8)$$

where E_{out} is energy released and E_{in} is the energy accumulated during constant current charging cycle [65,91].

4.5.3. Electrochemical impedance spectroscopy

Electrochemical impedance spectroscopy (EIS) is an electrochemical technique to measure the impedance of a system independence on *ac* frequency. EIS is a popular technique because it allows separating the influences of different components, like the contribution of the electron transfer resistance, double layer capacitance, faradaic reaction capacitance, and more.

In EIS measurement, a sinusoidal potential signal (Eq. 9) is applied to the system and the corresponding current (Eq. 10) is measured:

$$E_{ac}(t) = E_{0,ac} sin(\omega t) \quad (9)$$

$$I_{ac}(t) = I_{0,ac} sin(\omega t + \theta) \quad (10)$$

where $E_{0,ac}$ is the *ac* potential amplitude, $I_{0,ac}$ is the amplitude of the *ac* current, ω is the angular frequency ($2\pi f$), t is the time and θ is the phase angle. For complicated electrical circuits, the current and potential are often out of phase, the potential is lagging the current and for the ideal capacitor, the phase angle value is −90° [92,93].

In real electrochemical systems, consisting of resistive and capacitive elements, i.e. with corresponding components, the complex impedance is presented as follows:

$$Z(\omega) = Z'(\omega) + jZ''(\omega) \quad (11)$$

where $Z'(\omega) = R_s$ is the real part of impedance (θ = 0°) and $Z''(\omega) = (-1)/\omega C$ ($\theta = -90°$) is the imaginary part of impedance [92,93].

EIS measurement data can be presented in different ways. The first and most common one is the Nyquist plot, $Z''(\omega)$ vs. $Z'(\omega)$. The second one is called the Bode plot, $|Z(\omega)|$ vs. *ac* frequency, and the third one is the phase angle graph, θ vs. *ac* frequency [7,17,18,87,94–96].

The Nyquist plot for a typical EDLC consists of three parts: a semicircle at higher *ac* frequencies, a −45° slope region at intermediate *ac* frequencies, and a vertical line at the low *ac* frequency range. The semicircle at higher frequencies corresponds to charge storage steps, the series resistance of the electrode material, charge transfer resistance inside the electrode material structure, and the mass transfer resistance. The intermediate frequency region with a slope of –45° is characteristic of the mass transfer limited process with adsorption boundary conditions in the electrode matrix. In the low-frequency *ac* region, so-called double-layer capacitance region (finite length region), there is a line with a slope of −90°, which indicates the adsorption step rate limited process inside the electrodes. The "knee" frequency (where the –45° slope becomes −90°) indicates accessibility of ions into the pores and the higher the "knee" frequency value, the easier access of electrolyte ions into the pores of the electrode material and better performance of the EDLC at fast charge and discharge conditions. In the case of an ideal EDLC, only the vertical line (capacitance) of the $Z''(\omega)$ vs. $Z'(\omega)$ plot is constant over the entire frequency range [6,8,17,93–99].

The value of series capacitance is calculated according to Eq. 12:

$$C_s(\omega) = \frac{-1}{\omega Z''(\omega)} \tag{12}$$

where ω is an angular frequency ($2\pi f$) [6,65,97,98].

The values of complex power can be expressed as:

$$S(\omega) = P(\omega) + jQ(\omega) \tag{13}$$

where the active power $P(\omega)$ is:

$$P(\omega) = \omega C''(\omega)|\Delta E_{rms}|^2 \tag{14}$$

and the reactive power $Q(\omega)$ is:

$$Q(\omega) = -\omega C'(\omega)|\Delta E_{rms}|^2 \tag{15}$$

with $|\Delta E_{rms}|^2 = \frac{\Delta E_{max}}{\sqrt{2}}$ and E_{max} is the maximum amplitude of *ac* potential. In the case of an ideal capacitor, there is no real part and there is only the reactive contribution to the complex power, so Eq. 13 simplifies as follows:

$$S(\omega) = jQ = -\frac{j\Delta E_{rms}^2}{|Z''|} = -j\omega C\Delta E_{rms}^2. \tag{16}$$

Systems with ideal resistive behaviour have no imaginary part and the equation for complex power takes the form:

$$S(\omega) = \frac{\Delta E_{rms}^2}{|Z''|}. \tag{17}$$

Characteristic charging/discharging time constant τ_R values can be calculated from the frequency of interception points f_{int} of the $|P|/|S|$ and $|Q|/|S|$ curves:

$$\tau_R = \frac{1}{2\pi f_R}. \quad (18)$$

The time constant τ_R shows how much time it takes to release half of the stored energy [6,17,94–96,100].

4.5.4. Constant power method

In the constant power method, the power is held constant, i.e. as the potential decrease in discharge step the current is gradually increased:

$$P = I \cdot \Delta E = const \quad (19)$$

where P is the power, I is the current and ΔE is the cell potential.

Plotting energy (specific energy Wh kg^{-1} or energy density Wh dm^{-3}) and power (specific power kW kg^{-1} or power density W dm^{-3}) relationship we get the so-called Ragone plots. The Ragone plot is a useful tool to compare various energy storage devices, like batteries, fuel cells, capacitors, *etc*. because it shows the optimal working areas of different energy storage devices [6,10,101, 102].

To get the Ragone graphs, the energy stored in the studied system is measured (released) at different constant powers, and energy is calculated according to the following equation taking into account the system mass or volume:

$$E[W \cdot h] = P[W] \cdot t[h] \quad (20)$$

where t is the time during which the system is discharged at constant power. Usually, the system is discharged to half of the maximal cell potential as then 75% of the stored energy is received.

5. EXPERIMENTAL

5.1. Synthesis of carbide derived carbons

In this work sol-gel process was used to synthesize titanium carbide and then the synthesized carbides were chlorinated to obtain micro-mesoporous titanium carbide derived carbons. To increase the mesoporosity of the carbide derived carbon and increase the material conductivity, carbon nanotubes were added in various concentrations.

5.1.1. Sol-gel synthesis of titanium carbide precursor

As a metal source, titanium tetrabutoxide, $Ti(OC_4H_9)_4$ (99+%, Alfa-Aesar), was used and benzene-1,4-diol, $C_6H_6O_2$ (99.0%, Sigma-Aldrich), was used as a carbon source. 1 mol $Ti(OC_4H_9)_4$ was dissolved in ~2.7 mol 1-butanol (C_4H_9OH, ≥99.7%, Sigma-Aldrich) under argon in a three-neck flask. The solution was heated up to 80°C. For extra carbon source, $C_6H_6O_2$ in 1-butanol was added to the heated solution (for 1 mol $Ti(OC_4H_9)_4$, 0.55 mol $C_6H_6O_2$ was added). $C_6H_6O_2$ in 1-butanol was added dropwise, followed by heating the solution to 105 – 115°C and holding it at that temperature for two and a half hours for the reaction to be complete. Butanol was removed with simple distillation and a xerogel was received after the sample was dried completely. The dried sample was ground into a homogeneous powder. The synthesis scheme is drawn out in Fig. 4.

One sample was prepared without the addition of carbon nanotubes (CNT) and for two samples various amounts of CNTs (multiwall carbon nanotubes, 0.5 – 200 µm long, outer diameter 7 – 15 nm, inner diameter 3 – 6 nm, bundle, >95%, Aldrich) were added (1 wt% and 2 wt%). For the dispersion of CNTs, the surfactant of polyvinylpyrrolidone, $(C_6H_9NO)_m$ (avg. M=40 000g mol^{-1}, Sigma-Aldrich) was used. 1-butanol was used as a solvent. The molar ratio of surfactant/CNTs was 10:1. All solutions were treated with an ultrasonic probe (UP 200S, amplitude 50%, cycle 0.5) for three hours.

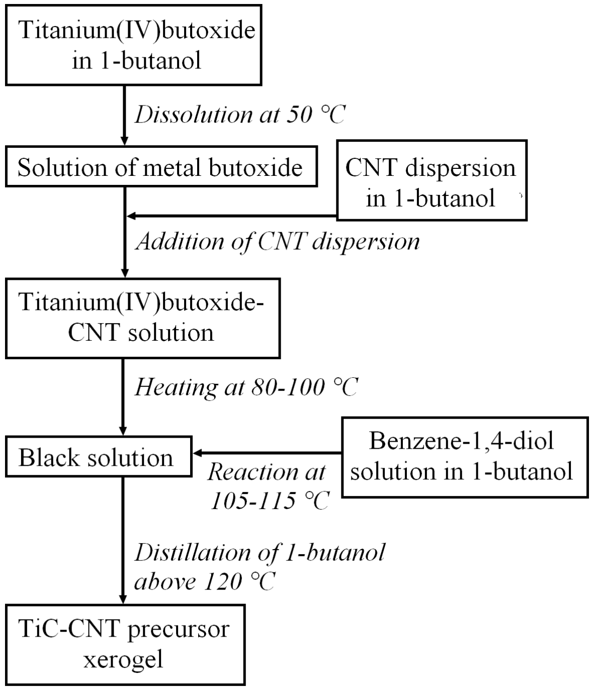

Figure 4. The scheme for the synthesis of titanium carbide precursor xerogel.

5.1.2. Pyrolysis, carbothermal reduction and chlorination

All sol-gel precursor materials were heat treated (pyrolyzed) at 800°C under argon atmosphere for 1h (reaction 8). The heating rate was adjusted to 200 °C h^{-1} and held at 800°C for 1 hour.

$$\text{TiC precursor} \xrightarrow{800°\text{C}} \text{TiO}_2 + \text{C} \tag{8}$$

Pyrolyzed precursor materials were reduced via carbothermic reaction (reaction 9) at 1350 °C in a vacuum at $7 - 8 \cdot 10^{-2}$ mbar in a tube furnace (WEBB 107) and the carbothermal reduction time at the maximum temperature was 120 min. The heating rate was adjusted to 200 °C h^{-1}.

$$\text{TiO}_2\text{+3C} \xrightarrow{1350°\text{C}} \text{TiC+2CO}\uparrow \tag{9}$$

The carbothermal reduction of titanium carbide takes place in a sequence of solid reaction products as follows: TiO_2 → Magneli phase (Ti_4O_7) → Ti_3O_5 → Ti_2O_3 → $TiOxC_{1-x}$ → TiC. When the carbothermal reduction sequence is not fully completed, then the final carbide might have oxygen or oxycarbide left in its structure. This might happen because the reduction temperature is too low and/or pressure is too high [36,103].

The synthesized titanium carbide and carbon nanotube composite (TiC-CNT) materials were then chlorinated using a tube furnace. The powder materials were placed into a quartz boat and then at T=950 °C chlorination reaction took place under steady flow of Cl_2 (AGA, 99.99%):

$$\mathrm{TiC} + 2\mathrm{Cl_2}\uparrow \rightarrow \mathrm{C} + \mathrm{TiCl_4}\uparrow. \qquad (10)$$

The flow rate of Cl_2 was fixed at 50 ml min^{-1}.

After chlorination, the CDC was treated with clean electrolytic H_2 at 900 °C for 1.5 h to dechlorinate thoroughly the CDC powders as well as to remove the residual chlorides, chlorine, and oxygen-containing functional groups from the surface of the porous carbon [104].

5.2. Physical characterization of carbon materials

For the physical characterization of the carbon materials X-ray diffraction, Raman spectroscopy, scanning electron microscopy methods were used and for the porosity analysis sorption measurements were performed.

XRD analysis was carried out at room temperature. The diffractograms were recorded using CuKα radiation (45 kV, 35 mA, λ = 0.154056 nm) with a step size 0.01° of glancing angle θ and with the holding time of 2 s at fixed θ on Bruker D8 Advance diffractometer (Bruker Corporation).

The Raman spectra were recorded using spectrometer Renishaw micro-Raman (setup equipped with 514 nm continuous mode argon ion laser, laser power 1.3 mW) and the spectral resolution was approximately 1.5 cm^{-1}.

The structures of the samples were studied using a scanning electron microscopy (SEM) using FEI Helios Nanolab 600.

Sorption measurements with nitrogen were carried out using the 3Flex system (Micromeritics) and secondly the carbon dioxide ASAP 2020 system (Micromeritics) was used. The specific surface area, S_{DFT}, was calculated according to NLDFT. The BET model was used for better comparison with previously published data [105,106]. Pore size distributions have been calculated by applying non-local density functional theory to N_2 adsorption isotherms and CO_2 adsorption isotherms applying program: Solution of Adsorption Integral Equation Using Splines (SAIEUS, Micromeritics). The models used for pore size distribution calculation were Carbon-N2-77, 2D-NLDFT Heterogeneous, and Carbon-CO2-273, 2D-NLDFT Het Surface [107,108].

5.3. Electrochemical characterization

For electrochemical measurements, the EDLC electrodes were composed of an aluminium current collector and a mixture of the synthesized CDC material and a 6 wt% binder (PTFE, 60 % dispersion in H_2O). This mixture was laminated and roll-pressed (HS-160N, Hohsen Corporation, Japan) together to form a flexible layer of the active electrode material with a thickness of 150 ± 5 μm. After drying under vacuum, the pure Al layer (2 μm) was deposited onto one side of the electrode by magnetron sputtering method. A two-electrode standard Al test cell (HS Test Cell, Hohsen Corporation) with two identical electrodes (geometric area of about 2.0 cm^2) was completed inside a glove box (Labmaster sp, MBraun; O_2 and H_2O concentrations lower than 0.1 ppm). A carefully dried 25 μm thick TF4425 (Nippon Kodoshi) separator sheet was used for mechanical separation of electrodes. All electrochemical experiments were carried out at room temperature ($T = 20°$).

Electrochemical measurements were carried out using two different electrolytes: the organic solvent based 1 M Et_3MeNBF_4 + AN and room temperature ionic liquid (RTIL) $EMImBF_4$.

Because of the high viscosity of the ionic liquid electrolyte, the completed cell was left to stand for a day to allow the electrodes thoroughly wet with the electrolyte. Before measurements, all the cells were cycled up to 3 V until a stable CV curve was achieved, and we were assured that the whole system was wetted with the electrolyte. The electrolyte was added in small excess to ensure the complete filling of all the pores.

Electrochemical characteristics have been studied by cyclic voltammetry, constant current charge/discharge, and the electrochemical impedance spectroscopy methods using a SI1287 Solartron potentiostat and 1252A frequency response analyzer over *ac* frequency, *f*, range from 1 mHz to 300 kHz at 5 mV modulation. Constant power tests were performed on a BT2000 testing system (Arbin Instruments, USA). For the passivation of TiC-CDC electrodes, step by step (100 mV) widening of the potential region (from 3.0 to 3.7 V) and repetitive (up to 3.4 V) cell potential cycling (up to 2500 times) was applied.

6. RESULTS

6.1. Sol-gel synthesized carbon materials

6.1.1. Physical characterization results

6.1.1.1. X-ray diffraction analysis

The XRD diffractograms in Fig. 5 are demonstrating the formation of TiC (111 and 200 reflections) after the carbothermal reduction process. The material containing 2 wt% CNTs also exhibits very small reflection near 25 – 26°, which can be related to the 002 peak of graphitic carbon originating from CNT. As titanium carbide and titanium oxycarbide have nearly the same lattice parameters, it was not possible to determine the exact stoichiometry of the synthesized TiO_xC_{1-x}/TiC materials based on the XRD measurements conducted. It has been shown by other authors that the exact stoichiometry depends noticeably on the carbothermal treatment temperature and duration [103,109]. XRF measurements conducted for TiC and TiC/2%CNT materials show that some oxygen is left in the final carbide material (Table 1). The stoichiometric carbide should contain about 80 wt% of titanium and 20 wt% of carbon. From Table 1 we can see that the carbides contain 74 – 79 wt% of titanium, 10 – 13 wt% of oxide, and 11 – 13 wt% of oxygen.

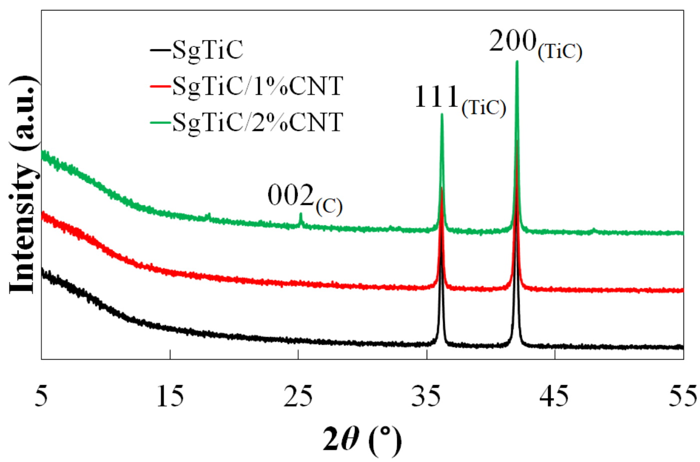

Figure 5. XRD patterns for synthesized carbides.

Table 1. XRF determination of C, O, and Ti in titanium carbide and titanium carbide carbon nanotube composites.

Element	TiC (wt%)	TiC/2%CNT (wt%)
C	11	13
O	10	13
Ti	79	74

Even though the carbothermal reduction process did not lead to a fully stoichiometric TiC, the CDC materials obtained (Fig. 6) after the high temperature chlorination process exhibit classical XRD diffractograms characteristics of the highly disordered micro- and mesoporous carbons [67,68,70,71,86,110]. For porous carbon materials synthesized from carbides, a typical diffractogram shows continuous bumpy diffraction peaks 002 (2θ ~ 26°) and 100/101 (2θ ~ 43°). The wide 002 peak corresponds to parallel-oriented graphite layers and 100/101 peak characterizes the size of the graphite layer [62–66].

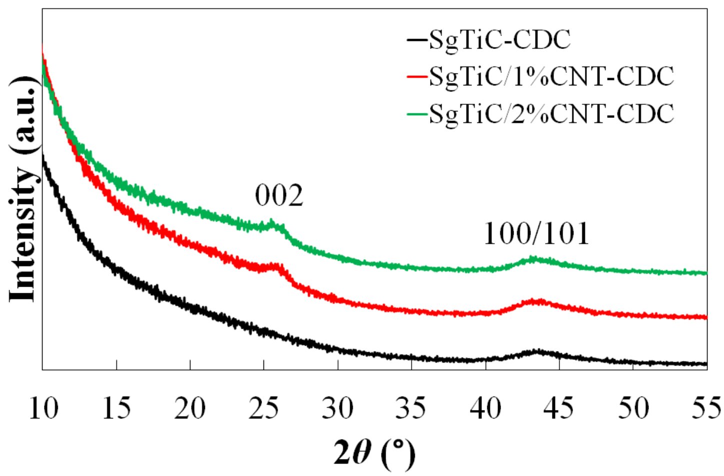

Figure 6. XRD patterns for synthesized carbide derived carbons.

6.1.1.2. Raman spectroscopy data

The Raman spectra show two main peaks for all the synthesized materials: at wavenumber 1348 cm^{-1}, the so-called D-peak that originates from the edges of the ordered areas (for example from defect regions in carbon structure) and at wavenumber 1587 cm^{-1}, the so-called G-peak that originates from the sp^2 carbon areas [65,111]. The Raman spectra (Fig. 7) for synthesized sol-gel derived carbon materials are characteristic of highly disordered micro and mesoporous carbons [71,110]. The addition of CNTs to the precursor carbide makes the resulting carbon material more disordered, evident of the intensity of the D-peak. For the carbon material with 2 wt% CNT addition, a well-developed 2D-peak can be seen at 2700 cm^{-1} (2D-peak, the second-order peak of D-band) which characterizes the well-developed graphitization and stacking of sp^2 layers [65,110,111].

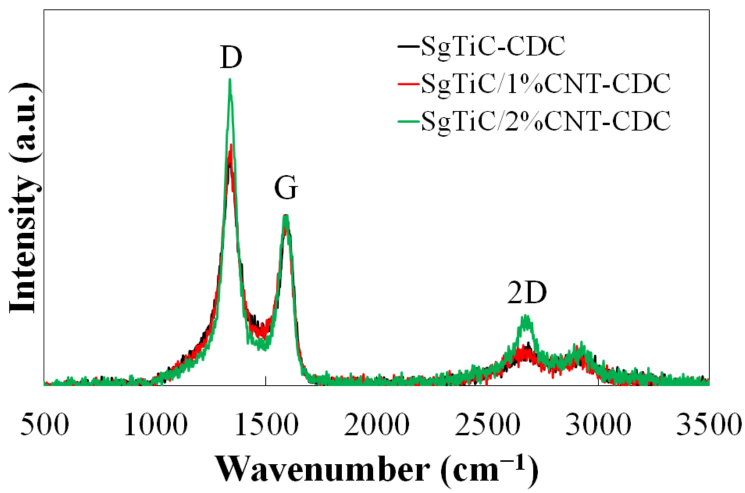

Figure 7. Raman spectra for synthesized carbide derived carbons.

6.1.1.3. Porosity characteristics

The specific surface areas and pore size distributions have been calculated from combined N_2 and CO_2 adsorption isotherms using two-dimensional non-local density functional theory and heterogeneous surface model (2D-NLDFT-HS) [80]. The adsorption/desorption isotherms show hysteresis loops for synthesized carbides (Fig. 8a) and carbon (Fig. 8b) materials; thus, all the materials are micro- and mesoporous.

The pore size distribution data corresponds to the isotherm data that the materials (both carbides and carbons) are micro- and mesoporous and have a big amount of micropores below 2 nm and a well-expressed amount of mesopores above 2 nm (Fig. 9).

Compared to commercial titanium carbide derived carbon, the sol-gel synthesized carbide derived carbon also has mesopores (Fig. 10).

The S_{DFT} data (Table 2) show that the carbon material without CNTs has the highest DFT specific surface area (1710 m^2 g^{-1}) and a high degree of mesoporosity in addition to microporosity.

Table 2. Results of the sorption measurements for the synthesized sol-gel titanium carbide and corresponding derived carbon (calculated by applying non-local density functional theory).

Sample	Carbide	Carbon		
	S_{DFT} ($m^2\ g^{-1}$)	S_{DFT} ($m^2\ g^{-1}$)	V_{micro} ($cm^3\ g^{-1}$)	V_{tot} ($cm^3\ g^{-1}$)
SgTiC-CDC	244	1710	0.45	2.85
SgTiC/1%CNT-CDC	152	1560	0.39	2.99
SgTiC/2%CNT-CDC	276	1510	0.38	2.94

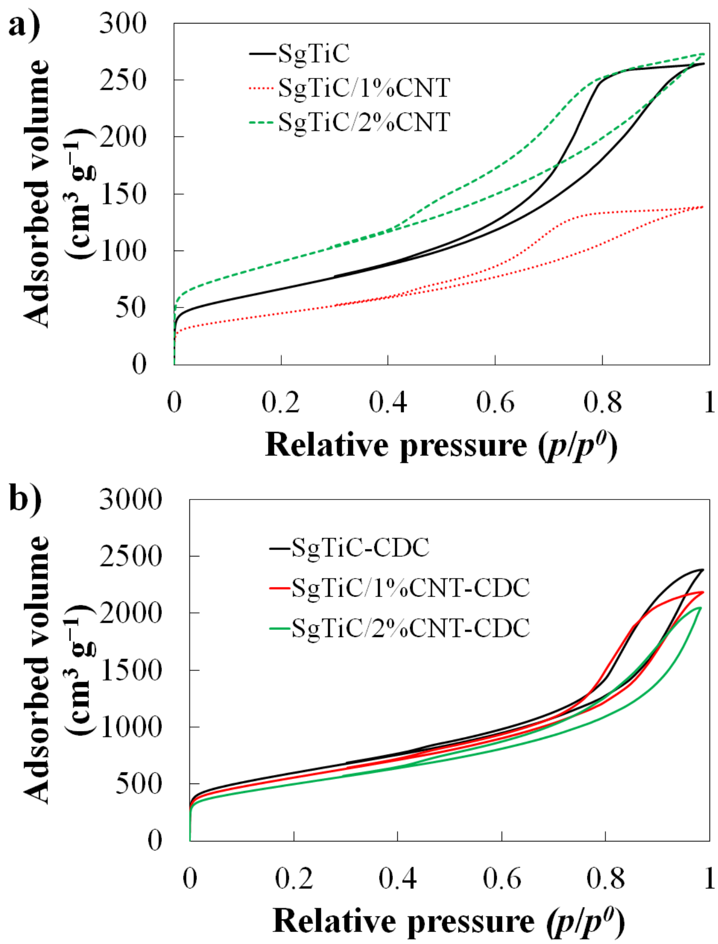

Figure 8. N_2 and CO_2 adsorption/desorption isotherms for synthesized a) carbides and b) carbons.

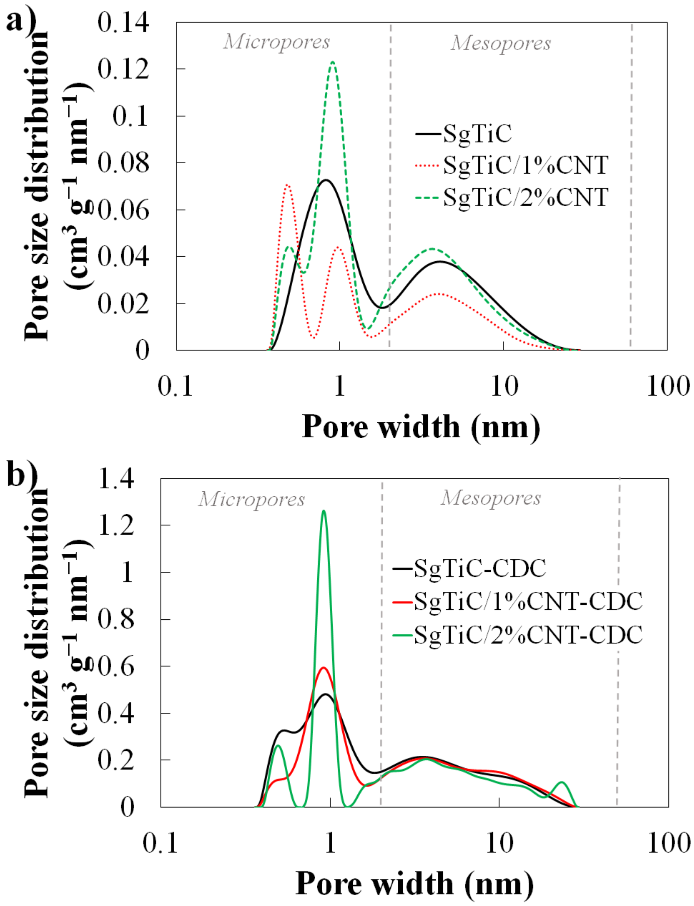

Figure 9. Differential pore size distribution vs. pore width plots for synthesized a) carbides and b) carbons.

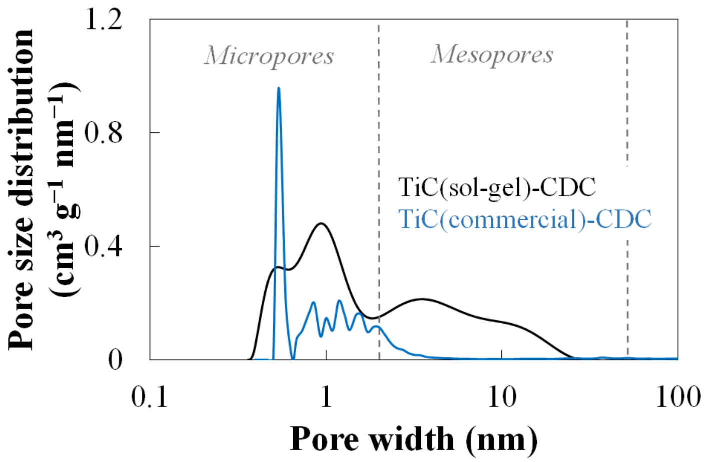

Figure 10. Differential pore size distribution vs. pore width plots for carbon derived from sol-gel synthesized titanium carbide and commercially available titanium carbide.

6.1.1.4. Scanning electron microscopy analysis

The scanning electron microscopy (SEM) images show that the precursor carbides synthesized via the sol-gel method have wide particle size distribution (Fig. 11a). Carbon material particle sizes without CNT addition (Fig. 11b) and with 1 wt% – 2 wt% CNT addition (Figs. 11c and 11d) vary from 1 μm to 20 μm. Carbon nanotubes can be seen in the carbon sample with 1 wt% CNT addition (Fig. 11c). Partially bundled carbon nanotubes can be seen on the surface of carbon particles in the sample with 2 wt% CNT addition (Fig. 11d). Big, crystallised particles can be seen in Figs. 11a – 11c, with exposed surface roughness. However, in Fig. 11b, very big particles with comparatively flat surfaces can be seen.

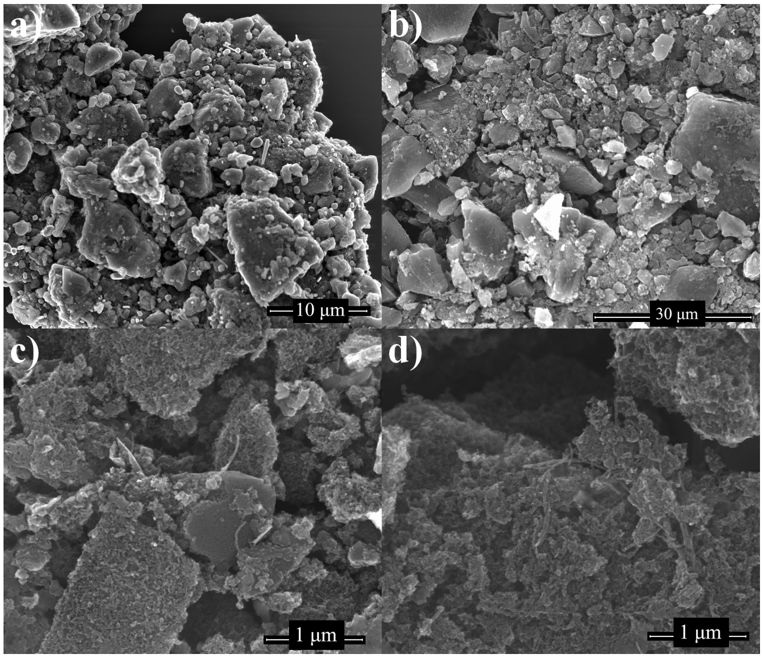

Figure 11. SEM images of the sol-gel synthesized a) TiC/2%CNT, b) TiC-CDC, c) TiC/1%CNT-CDC and d) TiC/2%CNT-CDC materials.

6.1.2. Electrochemical characterization

6.1.2.1. Cyclic voltammetry data

The cyclic voltammograms (CVs) for EDLC cells were measured within various cell potential regions ΔE (up to 3.8 V) at potential scan rates (v) from 1 to 500 mV s^{-1}.

The specific capacitance ($C_{m;CV}$) vs. cell potential (ΔE) curves for all samples (Figs. 12 – 14) demonstrate that there is a small, but clearly recognizable dependence of capacitance on the CNT fraction in the TiC-CDC powders. This could be explained by the specific surface area differences or that the pores or surfaces formed due to the inclusion of CNTs are not suitable for the formation of the electrical double layer [89]. All sol-gel TiC-CDC synthesized materials based EDLCs demonstrate practically ideal capacitive behaviour at cell potential scan rate $v = 500$ mV s^{-1} and up to $\Delta E = 3.4$ V in 1 M Et_3MeNBF_4 + AN and up to $\Delta E \leq 3.8$ V in ionic liquid $EtMeImBF_4$. The carbon material without CNT additions shows ideal capacitive behaviour up to $\Delta E \leq 3.6$ V at cell potential scan rate $v \leq 100$ mV s^{-1} (Fig. 15).

Comparison of CV curves shows that the capacitance values for 1 M Et_3MeNBF_4 + AN electrolyte based EDLC are 15 – 20% lower than those for $EtMeImBF_4$ based EDLC. At potential scan rate $v \geq 500$ mV s^{-1}, less expressed deviation of CV curves from the shape for ideally polarizable electrode has been observed for 1 M Et_3MeNBF_4 + AN electrolyte system explained by the lower viscosity and higher conductivity of RTIL electrolyte (Figs. 12 – 14).

The integral capacitance [6,64,112] values have been calculated over the cell potential range ΔE from 0 to 3.2 V using the integrated total charge density σ values obtained according to Eq. 4. In a symmetrical two-electrode system the specific capacitance $C_{m;CV}$ (F g^{-1}) for one activated carbon electrode can be calculated from cell capacitance C with Eq. 5. All the calculated data are given in Table 3. The capacitance values depend on the CNT additions in the resulting carbon material. The addition of CNT to TiC precursor material decreases the capacitance values of the EDLC. This can be explained by the decrease of specific surface area (Table 2) [70,85,113,114]. The highest integrated capacitance value 122 F g^{-1} at v = 10 mV s^{-1} from cyclic voltammetry data was obtained for the sample without CNT addition.

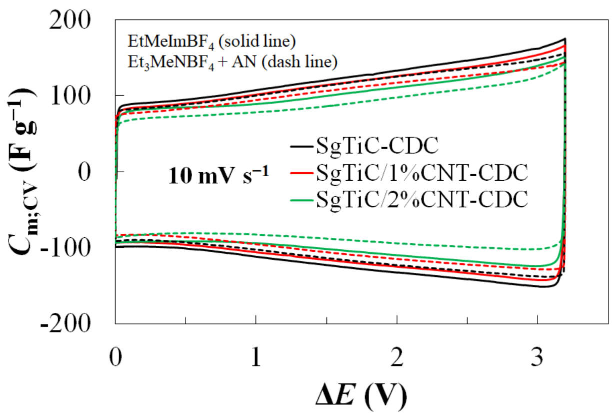

Figure 12. Specific capacitance vs. cell potential curves calculated from CV curves at potential scan rate v = 10 mV s^{-1}.

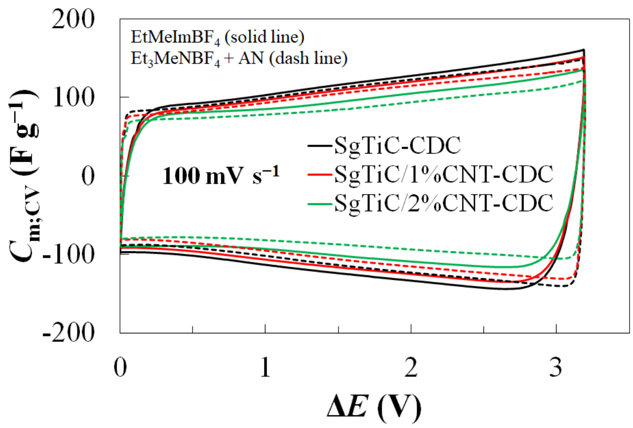

Figure 13. Specific capacitance vs. cell potential curves calculated from CV curves at potential scan rate $v = 100$ mV s^{-1}.

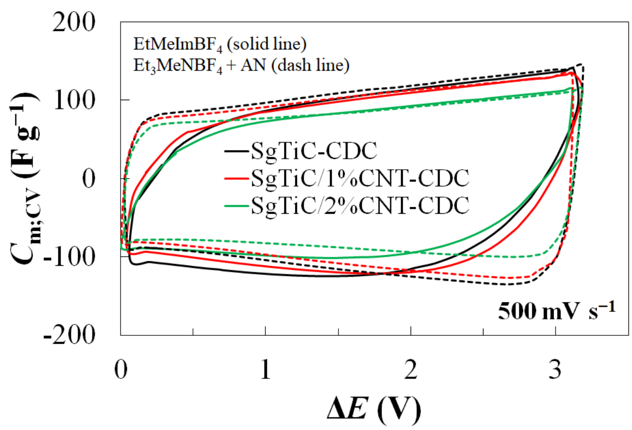

Figure 14. Specific capacitance vs. cell potential curves calculated from CV curves at potential scan rate $v = 500$ mV s^{-1}.

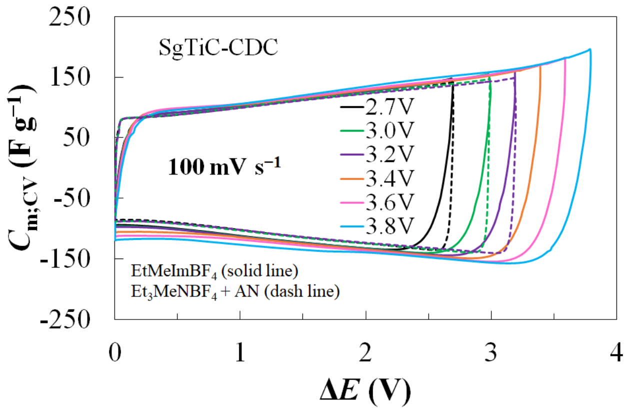

Figure 15. Specific capacitance vs. cell potential curves calculated from CV curves at different potentials at scan rate $v = 100$ mV s^{-1}.

For more detailed analysis $C_{m;CV}$ vs ΔE curves have been integrated and the charge density σ vs ΔE plots received are given in Fig. 16. This data shows that very high σ values have been achieved for all EDLCs tested. Data in Fig. 17 show that EDLCs completed using TiC-CDC material without CNT addition, σ vs ΔE plots are symmetrical within a very wide potential region (up to 3.6 V), and only at higher potentials very weak influence of faradaic processes can be seen.

Table 3. Integral specific capacitance values calculated from cyclic voltammetry data (ΔE from 0 V to 3.2 V; $v = 10$ mV s^{-1}; $v = 100$ mV s^{-1}; $v = 500$ mV s^{-1}).

Electrolyte	Electrode material	Capacitance $C_{m;CV}$ (F g^{-1})		
		10 mV s^{-1}	100 mV s^{-1}	500 mV s^{-1}
$EtMeImBF_4$	SgTiC-CDC	122	116	96
	SgTiC-CDC/1%CNT	115	109	94
	SgTiC-CDC/2%CNT	103	96	80
1 M Et_3MeNBF_4 + AN	SgTiC-CDC	112	111	106
	SgTiC-CDC/1%CNT	104	103	100
	SgTiC-CDC/2%CNT	93	92	89

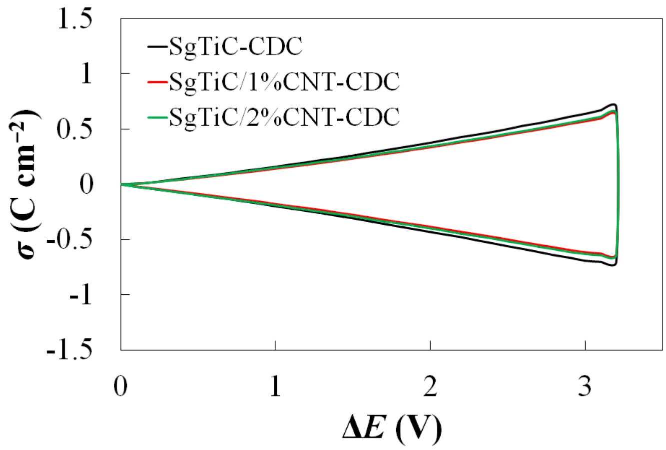

Figure 16. σ vs. ΔE plots for the EDLCs completed using different sol-gel titanium carbide derived carbon materials as electrodes, using $EtMeImBF_4$ electrolyte.

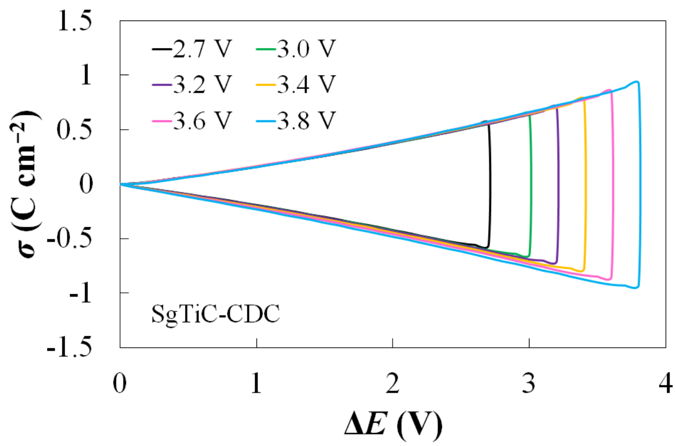

Figure 17. σ vs. ΔE plots for the EDLCs completed using sol-gel titanium carbide derived carbon material at different maximum cell potentials, using $EtMeImBF_4$ electrolyte.

Sol-gel synthesized TiC-CDC materials show one of the best capacitive behaviour at potentials over 3.2 V in 1 M Et_3MeNBF_4 + AN and at very high potential scan rates, while retaining good capacitive behaviour previously obtained only via different methods involving templating of CDC materials or electrospinning [115–118]. This indicates that even at such high potential scan rates (v = 500 mV s^{-1}), there is no significant potential drop arising from the slow mass-transfer step in the porous CDC matrix. This is probably due to the extra generated mesoporosity because the sol–gel synthesis method provides additional pores in the range from 4 to 10 nm.

6.1.2.2. Constant current charge/discharge data

The EDLCs were tested at constant current charge/discharge (CCCD) regimes (at current densities from 0.05 to 10 A g^{-1}) at the cell potentials from 0 to 3.8 V for $EtMeImBF_4$ based EDLC, and from 0 to 3.0 V for 1 M Et_3MeNBF_4 + AN based EDLC. The discharge and charge capacitances, C_{CC}, were calculated from the data of the third cycle according to Eq. 6.

The CCCD curves (Figs. 18 – 19) for the synthesized materials are nearly linear and symmetrical at all current densities applied (1–10 A g^{-1}), showing very good electrochemical reversibility. The nearly linear shape of CCCD curves at different current densities (1 A g^{-1} and 10 A g^{-1}) demonstrates that there is no significant contribution of the faradaic reactions inside of the micro-mesoporous carbon electrode structure. The IR-drop values are very low at current density 1 A g^{-1}. Only a very small IR-drop (from 0.05 V to 0.10 V) can be seen for EDLCs at 10 A g^{-1} charging/discharging current.

Very slightly different capacitance values obtained by CCCD method at discharge current density 10 A g^{-1} from CV method at v = 10 mV s^{-1} data (Tables 3 – 4) can be explained by physical differences in methods applied for charging/discharging of the electrodes and by the fact that at 10 A g^{-1} the full adsorption/desorption equilibrium has not been established yet.

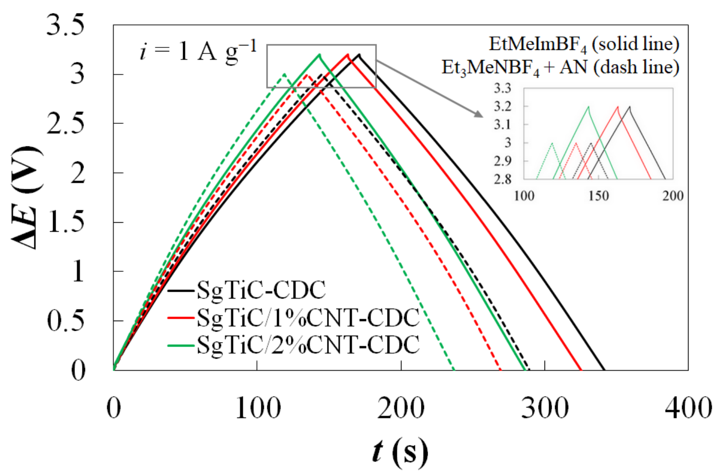

Figure 18. Constant current charge/discharge data at current density i = 1 A g^{-1}.

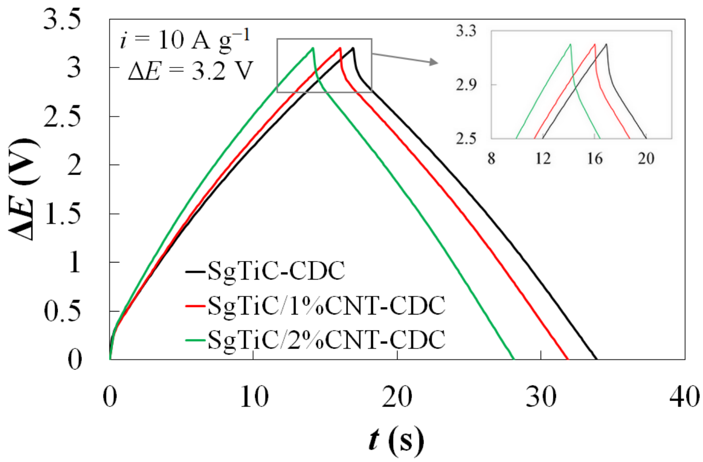

Figure 19. Constant current charge/discharge data at current density i = 10 A g^{-1} using $EtMeImBF_4$ electrolyte.

Table 4. Capacitance (C_{CC}) values calculated from constant current measurements (in $EtMeImBF_4$ ΔE = 3.2 V; in 1 M Et_3MeNBF_4+AN ΔE = 3.0 V; i = 1 A g^{-1} and i = 10 A g^{-1}).

Electrolyte	Electrode material	Capacitance C_{CC} (F g^{-1})	
		1 A g^{-1}	10 A g^{-1}
$EtMeImBF_4$	SgTiC-CDC	123	112
	SgTiC-CDC/1%CNT	117	106
	SgTiC-CDC/2%CNT	102	92
1 M Et_3MeNBF_4 + AN	SgTiC-CDC	111	N/A
	SgTiC-CDC/1%CNT	103	N/A
	SgTiC-CDC/2%CNT	90	N/A

The cycling efficiency or the so-called coulombic efficiency (η_{coul}) has been calculated as a ratio of charge densities released and accumulated ($\sigma_{discharge}/\sigma_{charge}$) during the discharging and charging steps of the EDLCs. The calculated data are given in Table 5. The η_{coul} values for all materials exceed 99%. For a more correct analysis of energy accumulation, the CCCD curves were integrated, and the energy densities stored (E_{in}) and released (E_{out}) were obtained based on Eq. 7. The values of energy efficiency η_{en} have been calculated based on Eq. 8 and given in Table 5. The η_{en} values vary from 93 to 95% at 1 A g^{-1}. Coulombic efficiency values (η_{coul} above 99%) show that sol-gel titanium carbide derived carbon materials combined with $EtMeImBF_4$ and 1 M Et_3MeNBF_4 + AN as electrolytes, are nearly ideal components for various energy/power storage complexes.

Table 5. Energy efficiency (η_{en}) and coulombic efficiency (η_{coul}) values calculated from constant current measurements (in $EtMeImBF_4$ ΔE = 3.2 V; in 1 M Et_3MeNBF_4 + AN ΔE = 3.0 V; i = 1 A g^{-1} and i = 10 A g^{-1}).

Electrolyte	Electrode material	1 A g^{-1}		10 A g^{-1}	
		η_{en}	η_{coul}	η_{en}	η_{coul}
$EtMeImBF_4$	SgTiC-CDC	95.10	99.99	83.08	99.58
	SgTiC-CDC/1%CNT	94.24	99.98	81.07	99.56
	SgTiC-CDC/2%CNT	93.51	99.9	80.04	99.07
1 M Et_3MeNBF_4 + AN	SgTiC-CDC	97.56	99.38	N/A	N/A
	SgTiC-CDC/1%CNT	97.75	99.96	N/A	N/A
	SgTiC-CDC/2%CNT	95.59	99.26	N/A	N/A

6.1.2.3. Impedance spectroscopy data

The Nyquist (−Z″, Z′) plots were measured in an *ac* frequency range from 1 mHz to 300 kHz at fixed cell potentials from 0 to 3.8 V for ionic liquid electrolyte $EtMeImBF_4$ and from 0 to 3.4 V for organic electrolyte 1 M Et_3MeNBF_4 + AN solution.

The shape of the Nyquist plot (Fig. 20) is independent of ΔE applied, if $\Delta E <$ 3.4V for $EtMeImBF_4$ and $\Delta E <$ 3.2V for 1 M Et_3MeNBF_4 + AN based EDLCs, indicating that there are no quick faradaic processes at or inside of the sol-gel synthesized TiC-CDC electrodes and there is no noticeable deviation from ideal polarizability conditions. The shape of the Nyquist plot in Fig. 21 shows that there is no noticeable deviation from ideal polarizability conditions for $EtMeImBF_4$ up to 3.6 V and for 1 M Et_3MeNBF_4 + AN up to 3.2 V.

The Nyquist plot for the studied materials consists mainly of two parts. First, the so-called ‘‘porous’’ region with a slope of nearly −45° in *ac* frequency region $0.1 < f < 100$ Hz, characteristic of the mass transfer limited process with adsorption boundary conditions in the micro-mesoporous carbon electrode matrix of an electrode [65,97]. In our EDLC completed with the synthesized sol-gel material, there is no semicircle visible in the Nyquist plots at higher *ac* frequencies, indicating that the mass transfer and adsorption steps are very quick inside of the synthesized carbon electrodes and the series resistance of a material, charge transfer resistance inside of the micro/mesoporous carbon structure as well as the mass transfer resistance (R_{CE}) are very low and practically independent of ΔE applied if $\Delta E \leq 3.2$ V.

The second region observed within the low-frequency *ac* region is the so-called double-layer capacitance region (finite length region) with a slope of a −90° that indicates the adsorption step rate limited process inside the porous electrodes are the rate determining for EDLC [65,97,114,119].

Sol-gel TiC-CDC without CNT addition has the highest value of “knee” frequency (0.38 Hz), which indicates easier accessibility of electrolyte ions into the pores and better performance at fast charging and discharging conditions

[99,120]. Comparison of the data for two electrolytes shows that the series resistance value depends noticeably on the electrolyte used, increasing from 1 M Et_3MeNBF_4 + AN to $EtMeImBF_4$. The so-called "porous region" length in Nyquist plot with slope −45° determining the mass transfer resistance value ($R_{pore} \leq 0.5$ and 2.5 Ω cm^2, respectively), is very short (3.5–4.0 times shorter) for AN based electrolyte, explained by the higher conductivity of 1 M Et_3MeNBF_4 + AN electrolyte.

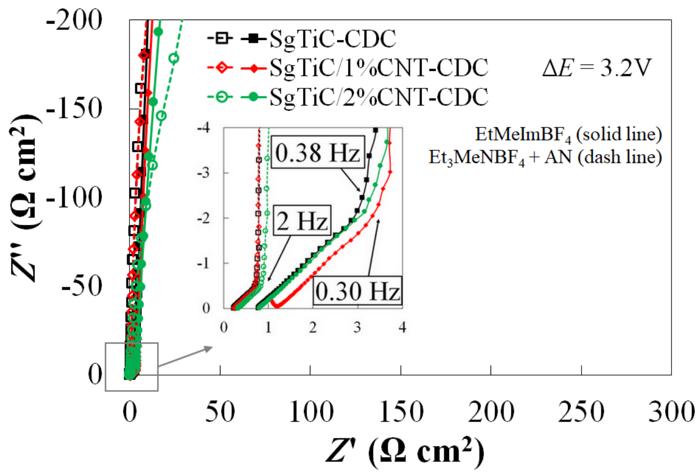

Figure 20. Nyquist plots for sol-gel titanium carbide derived carbon materials.

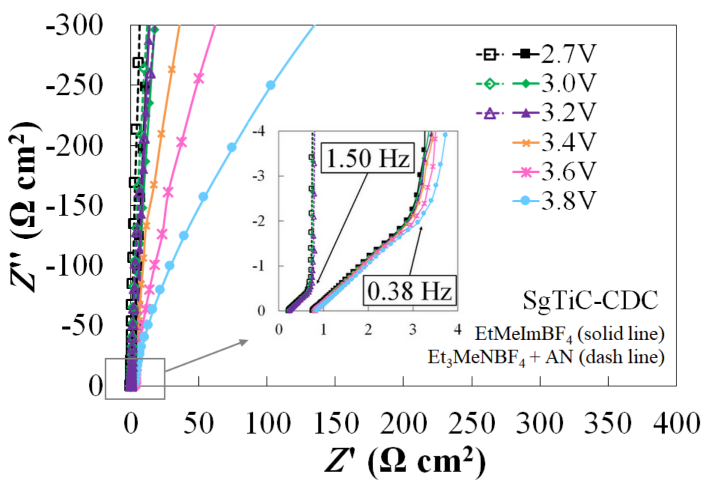

Figure 21. Nyquist plots for SgTiC-CDC at different maximum cell potentials.

The phase angle, θ, vs. *ac* frequency dependencies are shown in Fig. 22. For all synthesized materials, the phase angle θ was nearly −90° at $f \leq 0.1$ Hz demonstrating nearly ideal capacitive behaviour of systems under study [65,91, 97,98].

The phase angle values start to increase with increasing the cell potential $\Delta E \geq 3.3$ V (Fig. 23) because of the beginning of very slow faradaic reactions at the highly negatively and positively charged electrodes. Comparative analysis of impedance data with CV data indicates that these materials could be occasionally charged up to 3.2 or 3.4 V and as a result, only a slight loss in a lifetime could be expected due to the very slow rate of faradaic processes.

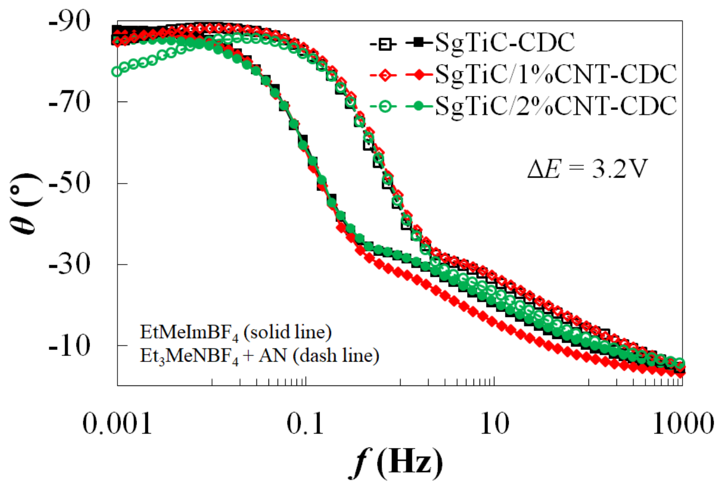

Figure 22. Phase angle vs. *ac* frequency dependencies.

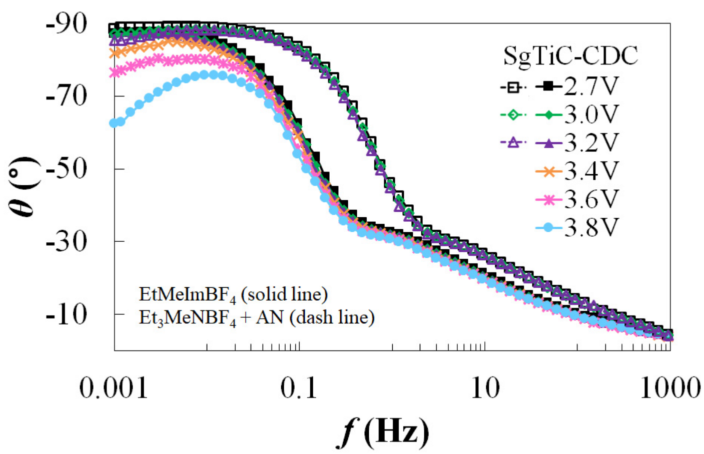

Figure 23. Phase angle vs. *ac* frequency dependencies for SgTiC-CDC at different maximum cell potentials.

The specific series capacitance, C_s values have been calculated from the impedance spectroscopy data at *ac* frequency $f = 1$ mHz according to Eq. 12. The C_s vs. f plots have long plateaus at $f < 1$ Hz and the highest capacitance value of 155 F g^{-1} (at 3.2 V) has been established for SgTiC-CDC (Fig. 24). This could be explained by the specific surface area differences [89]. For 1 M Et_3MeNBF_4 + AN based EDLCs the C_s values are somewhat lower (140 F g^{-1}) than those for ionic liquid based EDLC, explained by larger molar volume of Et_3MeN^+ than that for $EtMeIm^+$ or lower surface concentration of cation Et_3MeN^+ compared with $EtMeIm^+$ at the micro-mesoporous electrode surface. The series capacitance C_s vs. f plots for EDLC completed using Sg-TiC-CDC material (without CNT addition) (Fig. 25) have long plateaus at $f < 1$ Hz and C_s increases with the cell potential applied, explained by the increase of Gibbs adsorption of ions at higher positive and negative surface charge densities [121].

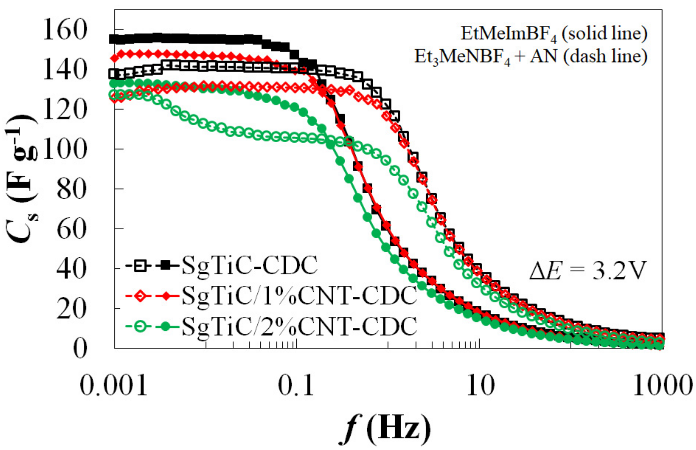

Figure 24. Specific series capacitance vs. *ac* frequency dependencies.

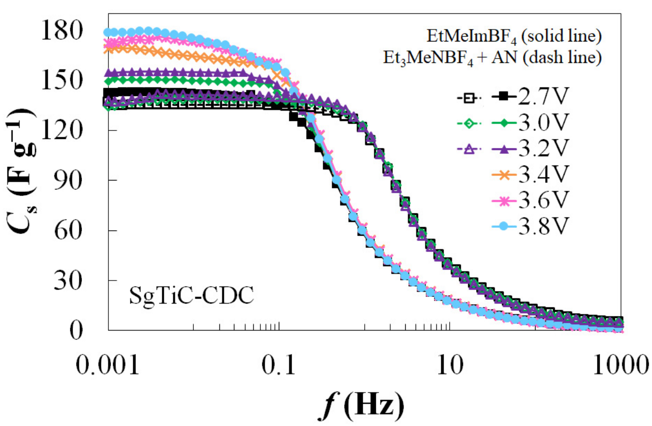

Figure 25. Specific series capacitance vs. *ac* frequency dependencies at different cell potentials.

According to electrochemical characterization, the high frequency series resistance R_s and so-called pore resistance R_{pore} were calculated, indicating that the different samples have quite similar electrochemical properties (Table 6).

Table 6. Electrochemical characteristics for different samples calculated using EIS data at cell potential ΔE = 3.0 V (R_s – high frequency series resistance, θ – phase angle at f = 1 mHz, R_{pore} – pore resistance, using 1 M Et_3MeNBF_4 + AN electrolyte.

Electrode material	R_s ($\Omega\cdot cm^2$)	θ (°)	R_{pore} ($\Omega\cdot cm^2$)
SgTiC-CDC	0.23	−87.0	0.45
SgTiC/1%CNT-CDC	0.22	−87.0	0.44
SgTiC/2%CNT-CDC	0.22	−86.0	0.46

The values of complex power were calculated according to Eq. 17 and the dependence of the normalised real part ($|P|/|S|$) and imaginary part ($|Q|/|S|$) of the complex power on *ac* frequency are presented in Fig. 26. Characteristic charging/discharging time constant τ_R values, also given in the Fig. 26 and Table 7, have been calculated from the frequency of interception points f_{int} of the $|P|/|S|$ and $|Q|/|S|$ curves. The τ_R value obtained for SgTiC-CDC|$EtMeImBF_4$ system (τ_R = 0.80 s) is substantially shorter compared with τ_R obtained for activated sucrose derived carbon (τ_R = 20 s) [122] carbon cloth (τ_R = 8s) [123], carbon material synthesized from commercially available TiC (τ_R = 1.76 s) [85] and D-glucose derived carbon (τ_R = 1.1 s) [120] systems in $EtMeImBF_4$.

Somewhat shorter τ_R value (τ_R = 0.15 s) have been calculated for SgTiC-CDC|1 M Et_3MeNBF_4 + AN (given in Fig. 26 and Table 7) system and for microporous TiC-CDC|Et_3MeNBF_4 + AN system (τ_R = 0.54 s) [66]. Extremely short characteristic time constants and high capacitance values indicate that synthesized materials can be used for completing very high power density EDLCs.

It should be noted that the relaxation time constant is a parameter that can somewhat change from cell to cell. The time constant depends both on the cell capacitance, but also on the cell resistance, the latter being mainly affected by the contact resistance between the electrode and the current collector, which probably varies between the cells used by different work groups and are, thus, not always very well comparable. However, in our work very high capacitance values indicate that the resistance values are very small in agreement with the data dismissed above, thus, very high power densities at high energy densities can be expected.

Table 7. Capacitance values calculated from impedance spectroscopy measurements (in $EtMeImBF_4$ ΔE = 3.2 V; in 1 M Et_3MeNBF_4 + AN ΔE = 3.0 V; f = 1 mHz) and time constant (τ_R) values for the electrode materials in different electrolytes applied.

Electrolyte	Electrode material	C_s (F g^{-1})	τ_R (s)
$EtMeImBF_4$	SgTiC-CDC	155	0.80
	SgTiC-CDC/1%CNT	147	0.86
	SgTiC-CDC/2%CNT	132	0.85
1 M Et_3MeNBF_4 + AN	SgTiC-CDC	139	0.15
	SgTiC-CDC/1%CNT	130	0.14
	SgTiC-CDC/2%CNT	117	0.14

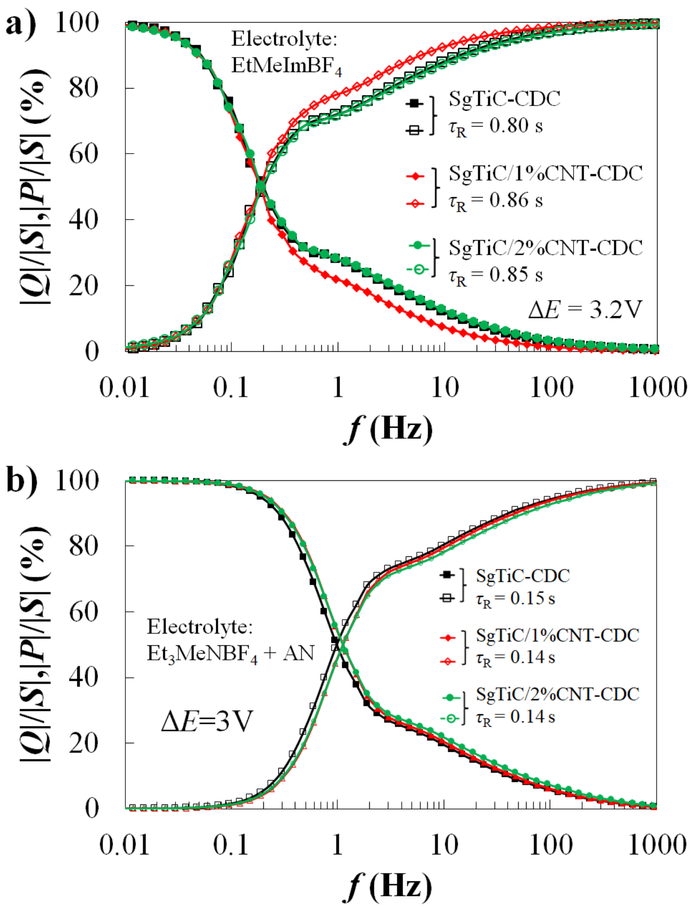

Figure 26. Normalised reactive power $|Q|/|S|$ and active power $|P|/|S|$ vs. *ac* frequency plot with corresponding time constants a) in $EtMeImBF_4$ electrolyte and b) 1 M Et_3MeNBF_4 + AN electrolyte.

6.1.2.4. Constant power measurement data

Ragone plots were experimentally measured from the constant power tests within the cell potential range from 3.2 V to 1.6 V for $EtMeImBF_4$ and 1 M Et_3MeNBF_4 + AN based EDLCs and the specific energy, *E*, vs. specific power, *P*, dependencies calculated to the total material weight of two electrodes. The Ragone plots show that at high specific energy 10 Wh kg^{-1} very high specific power ~100 kW kg^{-1} was achieved. Somewhat lower specific energy has been calculated for 1 M Et_3MeNBF_4 + AN based EDLCs at moderate power values because the densities of all systems (electrodes, membrane, and electrolyte) are higher for AN based EDLC compared with RTIL based EDLC (Fig. 27).

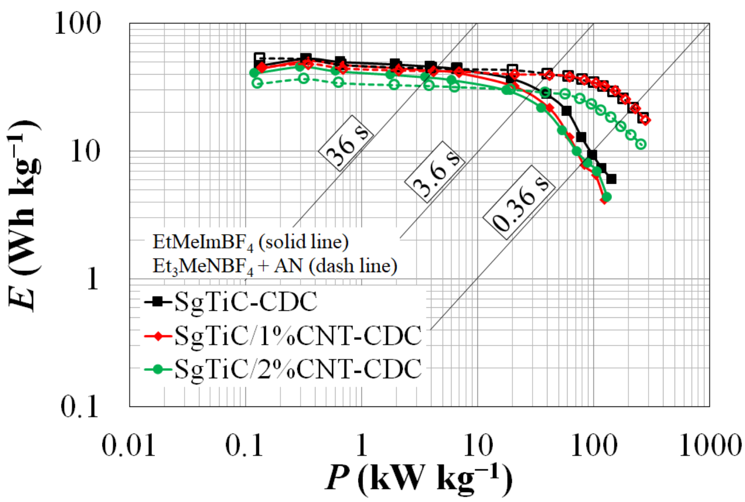

Figure 27. Gravimetric Ragone plot for EDLCs completed with synthesized materials.

The quicker decrease of specific energy for ionic liquid $EtMeImBF_4$ based EDLC is due to higher series resistance values caused by lower conductivity and higher viscosity of the ionic liquid electrolyte.

Good energy densities E = 7 Wh dm^{-3} at P = 10 kW dm^{-3} have been achieved as well (Fig. 28).

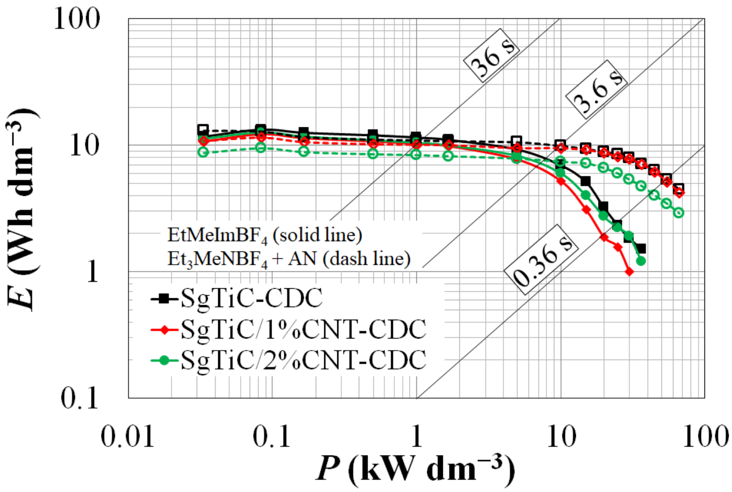

Figure 28. Volumetric Ragone plot for EDLCs completed with synthesized materials.

The EDLCs completed show weak influence of the CNT addition into the precursor carbide derived carbon electrode characteristics including on the stored specific energy and power values delivered by EDLCs completed using sol-gel synthesized carbon material based electrodes.

The comparison of Ragone plots with other EDLCs containing $EtMeImBF_4$ (ionic liquid) or 1 M Et_3MeNBF_4 + AN as an electrolyte is given in Fig. 29. The sol-gel synthesized TiC-CDC based EDLCs have higher specific energy at higher specific power values, compared to for example previously published works like microporous carbon derived from commercially available TiC [65], D-glucose derived carbon (GDAC-12h) [120], micro-mesoporous D-glucose derived carbon (MMP GDAC) [124], steam activated carbon derived from SiC [125] and carbon derived from granulated white sugar (GWS carbon) [113].

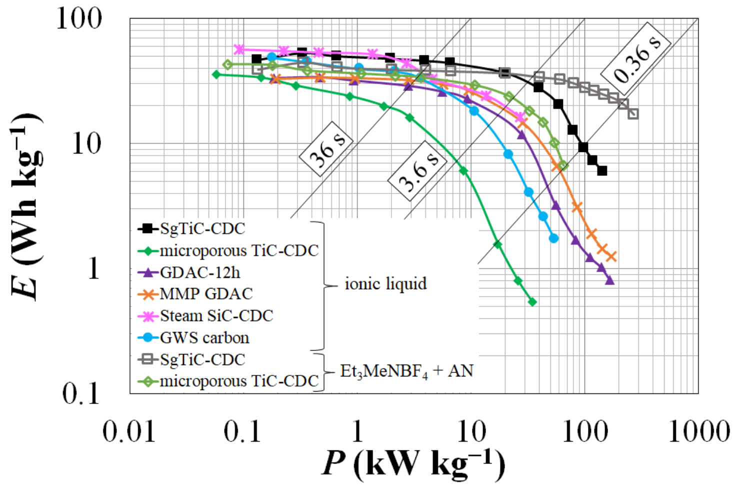

Figure 29. Ragone plot for EDLCs completed with different synthesized materials.

6.1.2.5. Lifetime test results

The combined cyclability testing method used for SgTiC-CDC and 1 M Et_3MeNBF_4 + AN system is shown schematically in Fig. 30 [126]. After cyclic voltammetry measurements (Fig. 31) and 500 galvanostatic charge/discharge cycles (1 A g^{-1}) within potential regions from 0 to 3.0 V (Fig. 32) and 10 h holding of the cell at 3.0 V, the impedance spectra were measured at 3.0 V (Fig. 33). Results in Fig. 31 indicate that there is a very slow decrease of cell capacitance calculated from cyclic voltammograms (from 130 to 125 F g^{-1}) as well as shortening of charging/discharging times 5 – 10 % (Fig. 32). The Nyquist plots shape is practically independent of cycle numbers applied, however, a very small increase of series resistance (6 – 7 %) from 0.28 to 0.30 Ω cm^2 takes place (inset in Fig. 33). According to series capacitance, C_s, calculations (Fig. 34) the capacitance values decrease less than 15 % during 2500 constant current charge/discharge cycles (total number) and 50 h (total holding) applied. Throughout the cyclability test, the electrode material demonstrated nearly ideal capacitive behaviour.

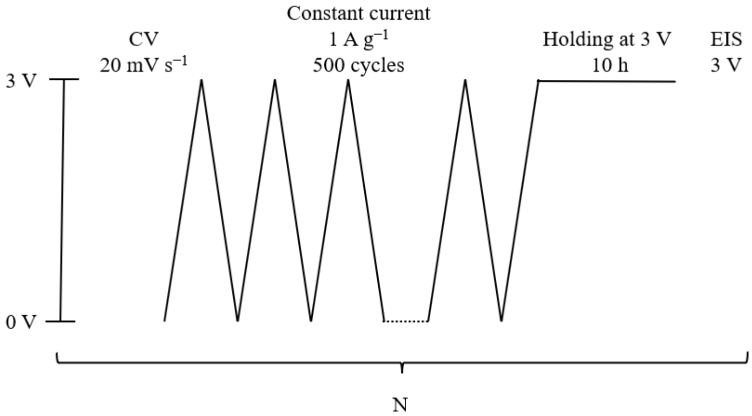

Figure 30. The electrochemical cyclability test's measurement setup cycle (N).

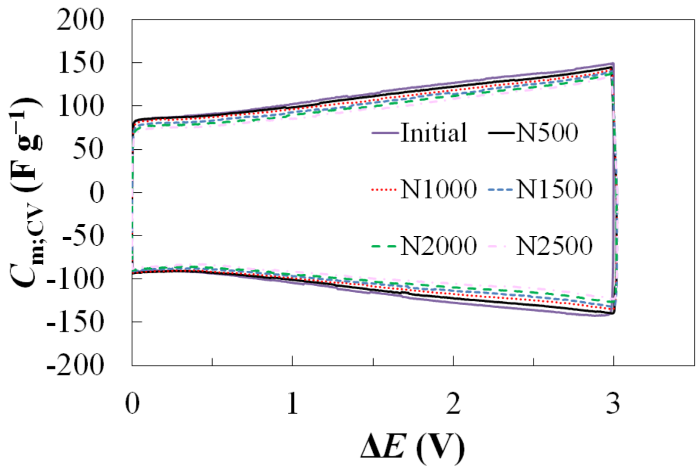

Figure 31. The electrochemical cyclability test's cyclic voltammograms measured within a cell potential range ΔE from 0 to 3.0 V using 1 M Et_3MeNBF_4 + AN electrolyte.

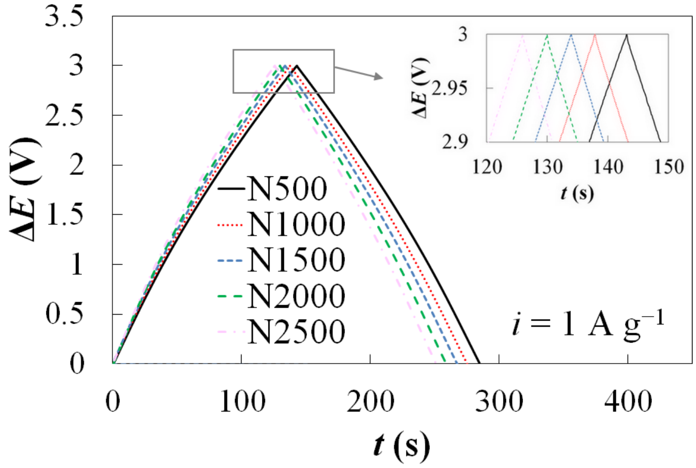

Figure 32. The electrochemical cyclability test's constant current charging/discharging curves measured within a cell potential range ΔE from 0 to 3.0 Vusing 1 M Et_3MeNBF_4 + AN electrolyte.

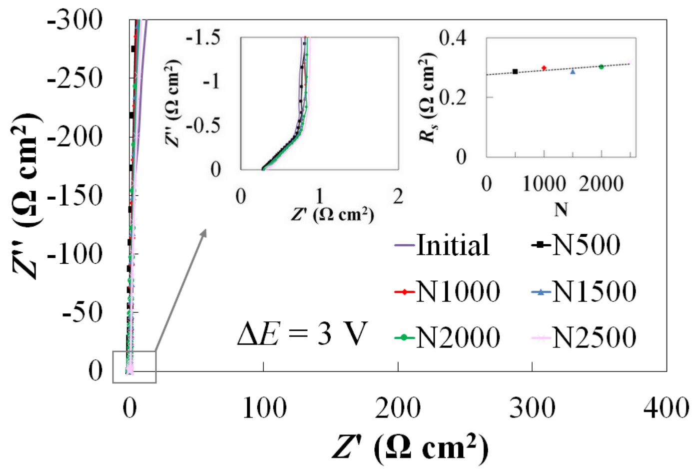

Figure 33. The electrochemical cyclability test's Nyquist plots measured at cell potential ΔE = 3.0 V using 1 M Et_3MeNBF_4 + AN electrolyte.

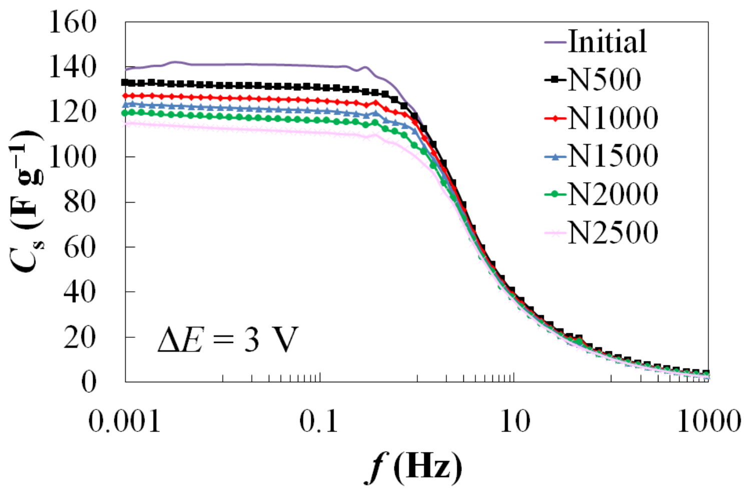

Figure 34. The electrochemical cyclability test's specific series capacitance vs. *ac* frequency dependencies measured at cell potential ΔE = 3.0 V using 1 M Et_3MeNBF_4 + AN electrolyte.

6.2. Operando passivation of electrodes

6.2.1. Characterization methods

For the passivation studies in 1 M Et_3MeNBF_4 + AN electrolyte the carbide derived carbon (TiC-CDC) was synthesized from the commercial titanium carbide (TiC, 99.5% purity, −325 mesh powder, Sigma-Aldrich) and the passivation of TiC-CDC electrodes was achieved by the step by step (100 mV) widening of the cell potential region (from 3.0 to 3.7 V) and repetitive (up to 3.4 V) potential cycling (up to 2500 times). The electrochemical characteristics of the completed EDLC cells were studied by the CV, CCCD, EIS, and the constant power methods.

Infrared spectra before and after electrochemical tests were recorded under nitrogen atmosphere with Perkin-Elmer Spectrum GX FT-IR (Fourier-transform infrared) system using ATR configuration [127,128]. Ge hemisphere and IR beam angle of 65° were applied and the Raman spectra were obtained with 514 nm excitation using Renishaw inVia Raman spectrometer. The electrode was placed into a closed argon-filled cell with a glass window.

6.2.2. Analysis of electrochemical data

Data in Fig. 35 show that for TiC-CDC two-electrode symmetrical cell no quick faradaic reactions occur up to 3.7 V if the widening of cell potential has been taken by small 100 mV steps. It should be noted that after measuring CVs at each potential window, the charge and discharge (CCCD) curves at constant current density were obtained. Thereafter an impedance spectrum was measured, thus after holding the TiC-CDC cell at the given maximum potential for ~90 min. Comparison of the $C_{m;CV}$ vs. ΔE curves measured at different potentials scan rates v from 5 to 500 mV s^{-1} (Fig. 36) indicates that the values of $C_{m;CV}$ do not decrease noticeably up to v = 200 mV s^{-1}, demonstrating that only very quick adsorption/desorption step rate limited reversible processes occur. At v = 500 mV s^{-1}, there is no ideal shape CVs for TiC-CDC EDLCs, indicating that the absorption equilibrium has not been established. A very good agreement of current (capacitance) values can be seen in Fig. 35, independent of the maximum cell potential (up to 3.7 V) applied. Thus, differently from the results of papers [129–133], there are no noticeable quick faradaic processes at the electrodes under study in agreement with the results of other works [127,128,134,135].

For operando electro-reduction of surface active functional groups, the cell was repetitively charged/discharged up to 3.4 V at scan rate v = 50 mV s^{-1} applying many (from 500 to 2500) CV cycles (Fig. 37), and nearly ideal polarizability has been observed for the 2 electrode EDLC system even after 2500 cycles.

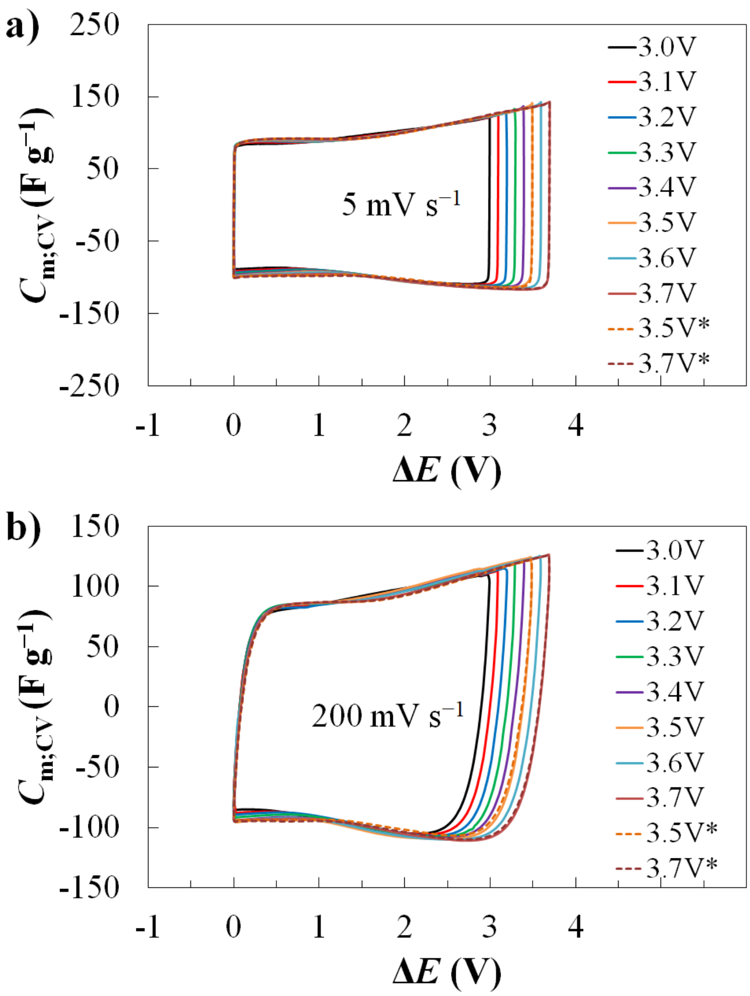

Figure 35. Specific capacitance vs. cell potential curves in 1 M Et_3MeNBF_4 + AN electrolyte calculated from CV curves at potential scan rates: a) 5 mV s^{-1} and b) 200 mV s^{-1} if the electrode potential was increased with 100 mV steps. * *denotes measurement after reaching 3.7 V.*

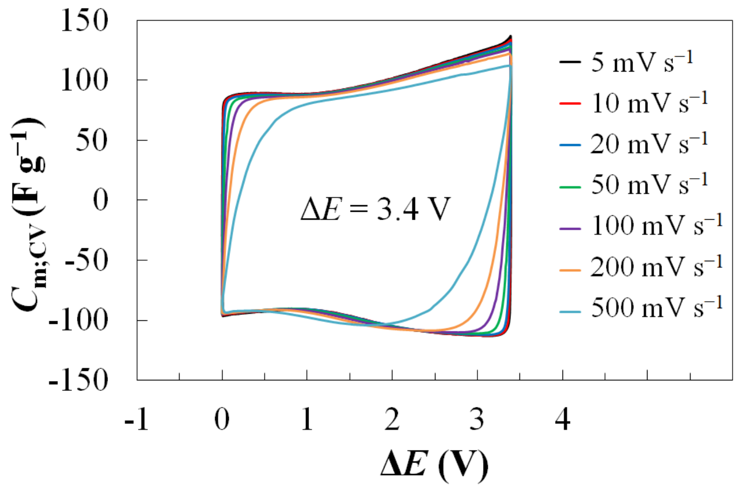

Figure 36. Specific capacitance vs. cell potential curves in 1 M Et_3MeNBF_4 + AN electrolyte calculated from CV curves measured at different scan rates at a fixed cell potential $\Delta E = 3.4$ V.

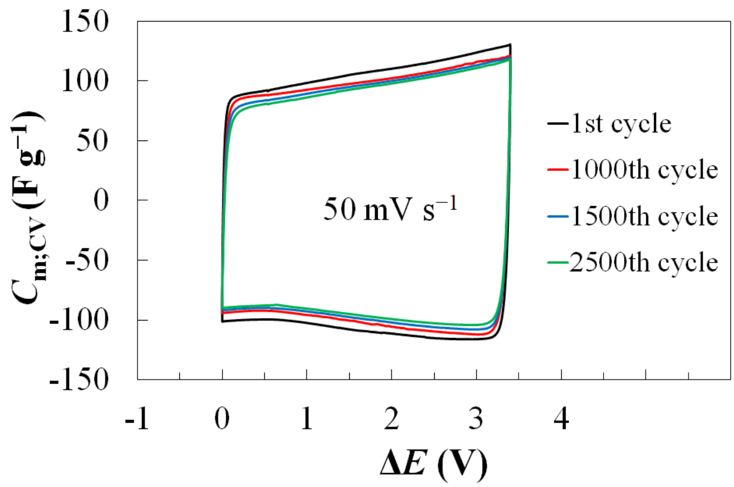

Figure 37. Specific capacitance vs. cell potential curves in 1 M Et_3MeNBF_4 + AN electrolyte calculated from CV curves measured at 50 mV s^{-1} (ΔE = 3.4V), after 1, 1000, 1500 and 2500 cycles.

The constant current charge/discharge (CCCD) plots obtained during longer ageing (holding at constant potential) tests (Fig. 38) are linear and have a symmetrical shape. The energetic efficiency values and the coulombic efficiency values have been calculated from CCCD plots and data established are given in Fig. 39. The values of energy efficiency are very high (90%), up to 240 h holding time of the two-electrode cell at ΔE = 3.4 V. At longer holding times, t > 240 h, a noticeable decrease in efficiency takes place. However, a noticeably quicker decrease of efficiency takes place for the TiC-CDC based cell without operando passivation.

The IR-drop values are very low for pre-treated partially passivated cells. IR-drop starts to increase only after polarization at 3.4 V for 300 h (Fig. 39) in agreement with CV and impedance data (Figs. 35 and 41). The increase of IR_{drop} is very low in the case of the passivated electrode system. However, the quick increase of IR_{drop} at ΔE = 3.4 V can be seen for the cells with unblocked (or not passivated) electrodes, similar to other results [130–133].

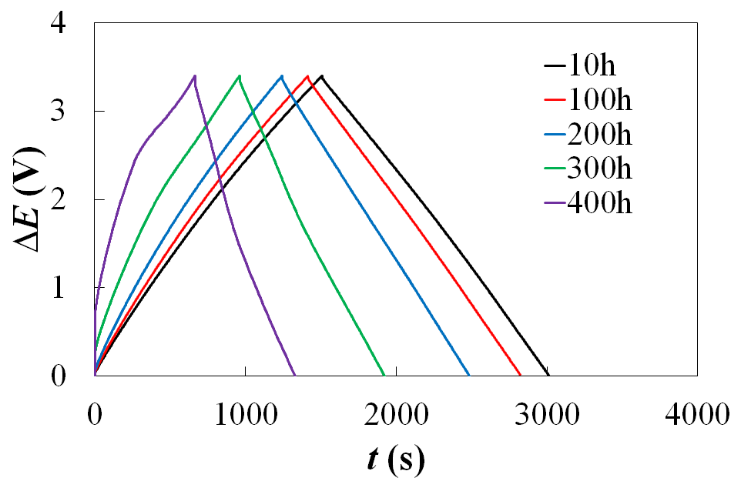

Figure 38. Constant current charge/discharge cycles in 1 M Et_3MeNBF_4 + AN electrolyte at current density i = 1 A g^{-1}. During the cell lifetime measurement, the CCCD curves have been measured after total holding at 3.4 V for the noted time for the system passivated at 3.7 V.

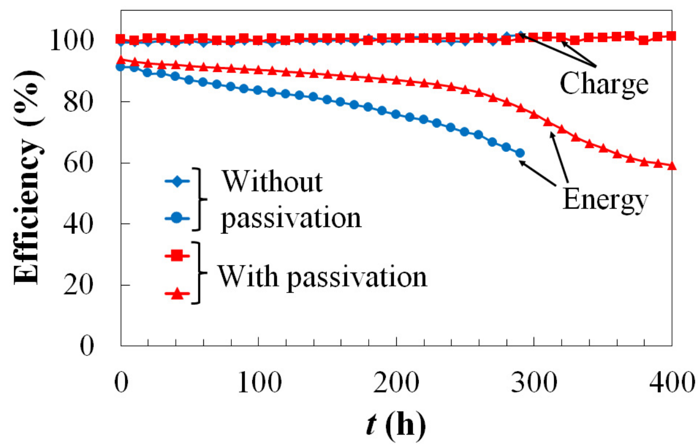

Figure 39. Charge and energy efficiencies vs. holding time plots in 1 M Et_3MeNBF_4 + AN electrolyte calculated from CCCD curves at 1 A g^{-1} (at testing times cycled from 0 to 3.4 V) for passivated and not passivated systems.

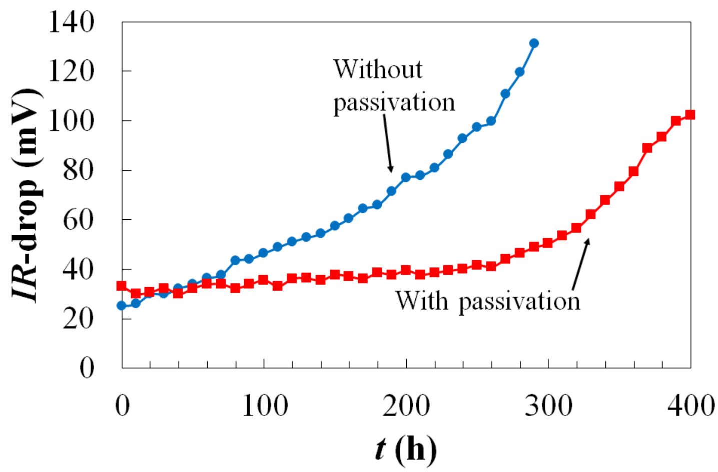

Figure 40. Internal ohmic drop for passivated and not passivated systems in 1 M Et_3MeNBF_4 + AN electrolyte.

The analysis of the Nyquist plots measured at fixed cell potentials, the noticeable deviation from ideal polarizability started at $\Delta E \geq 3.3$ V if the preliminary passivation process was not used (Fig. 41). For operando electro-reduction of surface active functional groups, the cell was repetitively charged/discharged up to 3.4 V applying many CV cycles (from 500 to 2500). After CV tests, the Nyquist plots were measured and data in Fig. 41 show that, surprisingly, after reaching the cell potentials up to $\Delta E \geq 3.5$ V, deviation from ideal polarizability decreases, and nearly ideal polarizability has been observed for the 2 electrode EDLC system even at ΔE = 3.7 V. For similar systems, without repetitive CV and CCCD measurements (Fig. 41) such passivation effect never occurred, no matter how long the system had been kept at the fixed ΔE = 3.4 V cell potential. Repetitive cell polarization up to $\Delta E \leq 3.4$ V generates the surface conditions, where a system subjected to very high potentials (polarized at $\Delta E \geq 3.5$ V) is much more stable at fixed $\Delta E \geq 3.4$ V than a system, which has never been polarized repeatedly at cell potential more than $\Delta E \geq 3.4$ V. Due to different electrode precondition treatment methods applied somewhat different behaviour of carbon electrodes in non-aqueous and ionic liquid electrolyte based EDLCs have been observed [130–133,136]. However, data in Fig. 41b inset show that during holding and impedance measurements at 3.4 V, the high-frequency series resistance increases nearly 20 – 25%, indicating that either a thin less conducting film has been deposited onto TiC-CDC electrode surfaces or some morphological changes have taken place in the electrodes.

Series resistance values are given in Figure 42. A slight increase in resistance that can be seen in Fig. 42a can be explained by adsorption of gases onto/into macropores of the TiC-CDC electrodes. It is interesting that the series resistance values (R_s) at low frequency (f = 0.001 Hz) only very weakly depend on the cell potential applied (Fig. 42b).

Data in Fig. 43 show that the so-called porous material resistance value (R_{pore}), usually connected with the mass transfer of ions in mesopores [6–12,21,22,69,96,135], weakly depends on cell potential applied and can be explained that there is only weak blocking of mesopores.

The R_{pore} data are in a very good agreement with log|−Z''|, log$f$ plot data [136], presented in Fig. 44, where two linear regions have been observed: first from 100 to 0.5 Hz (porous region) with −0.492 slope, i.e. nearly equal to that for ideal semi-infinite mass transfer process (for ideal process the slope is −0.5), and the second linear region (slope −0.992) at lower frequencies (from f < 0.5 Hz) which is equal to that for ideal adsorption step limited processes (slope −1.0). The shape of the log|−Z''|, log$f$ plot is clearly independent of the cell potential applied. It demonstrates that the capacitance values are nearly independent of cell potential and CV or CCCD cycle number applied. Thus, based on Orazem et al. [136] and previous papers published in our workgroup [66,119,137,138], the systems under study are ideally polarizable up to 3.7 V, if very careful passivation (pre-treatment of electrodes, i.e. repetitive potential cycling up to 3.4 V and step by step widening of cell potential up to 3.7 V) has been applied. Only at the high frequency region, there is an increase of log|−Z''| values explained by the formation of gases or dielectric layer between carbon electrodes and Al current collectors (mainly positively charged current collector).

The θ vs. f plot results in Fig. 45 are in agreement with the Nyquist plot. At fixed ΔE = 3.4 V, when the system was never subjected to repetitive cell polarization or for CV cycling to higher cell potentials $\Delta E \geq 3.5$ V, the absolute phase angle θ values decrease at very low $f \leq 3$ mHz. However, after some hundred CV and CCCD cyclization steps and polarizing of the system at potentials $\Delta E \geq 3.5$ V, the absolute values of phase angle θ started to increase indicating that some passivation (or stabilization) in the cell takes place. Surprisingly, the cells retain nearly ideal polarizability even up to 3.7 V.

The values of series capacitance have been calculated according to Eq. 12 and are given in Fig. 46. The C_s vs. f plots have long plateaus at $f < 1$ Hz and C_s weakly increases with the cell potential applied (explained by the increase of Gibbs adsorption of ions at higher positive and negative surface charge densities). Long linear plateaus at $f \rightarrow 0$ indicate that equilibrium capacitance values have been established and the systems under study are nearly ideally polarizable up to 3.4 V (without passivation/stabilization) and even up to 3.7 V if the TiC-CDC electrodes have been carefully passivated/stabilized at $\Delta E \geq 3.5$ V.

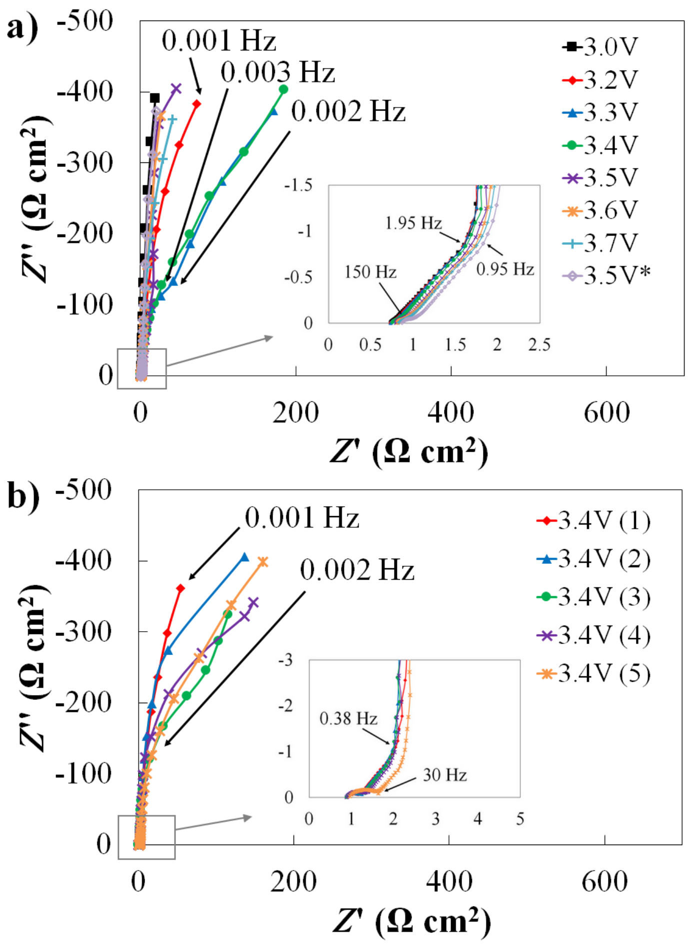

Figure 41. Nyquist plots for system in 1 M Et_3MeNBF_4 + AN electrolyte subjected a) to passivation up to 3.7 V, b) after measurement CV cyclation up to maximum potential 3.4 V. * *denotes measurement after reaching 3.7 V and (1) – (5) in (b) denotes measurement after 500, 1000, 1500, 2000 and 2500 cycles at 50 mV s^{-1}.*

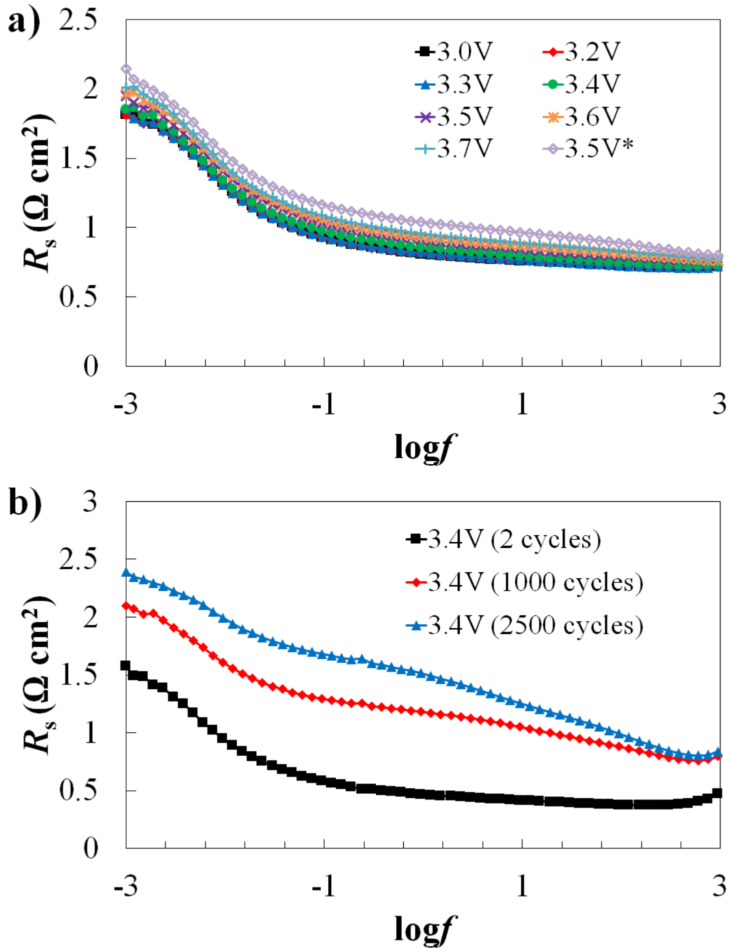

Figure 42. Series resistance vs. log*f* plots in 1 M Et_3MeNBF_4 + AN electrolyte a) for system subjected to passivation at 3.7 V, b) for system at a fixed cell potential 3.4 V after 2, 1000, and 2500 cycles. * *denotes measurement after reaching 3.7 V.*

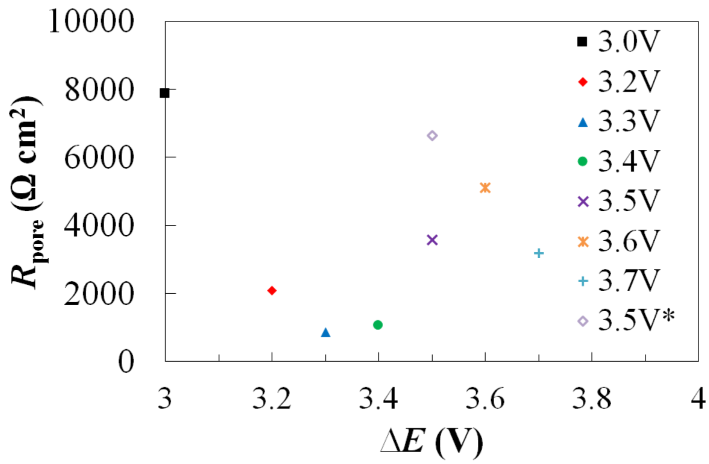

Figure 43. Pore resistance vs. cell potential plot for a system in 1 M Et_3MeNBF_4 + AN electrolyte subjected to passivation for different ΔE up to 3.7 V at f = 1 mHz. * *denotes measurement after reaching 3.7 V.*

Experimental Ragone plots for the two-electrode EDLC cells completed are given in Fig. 47, indicating that very high energy and power densities, higher than those for traditional AN based TiC-CDC electrodes (ideally polarizable only up to 3.0 V), have been achieved. The P and E values obtained are comparable with corresponding data for sol-gel method synthesized TiC-CDC electrodes and ionic liquid based systems.

For time-stability analysis, the holding tests were conducted (Fig. 48). It is very well visible that the cell is more stable after systematic step by step repetitive treatment at high cell potentials ($\Delta E \geq 3.5$ V) than the cell without the special passivation steps. Very stable energy densities at fixed power density have been observed for the first 150 h test for electrochemically operando modified electrodes differently from non-passivated TiC-CDC electrodes.

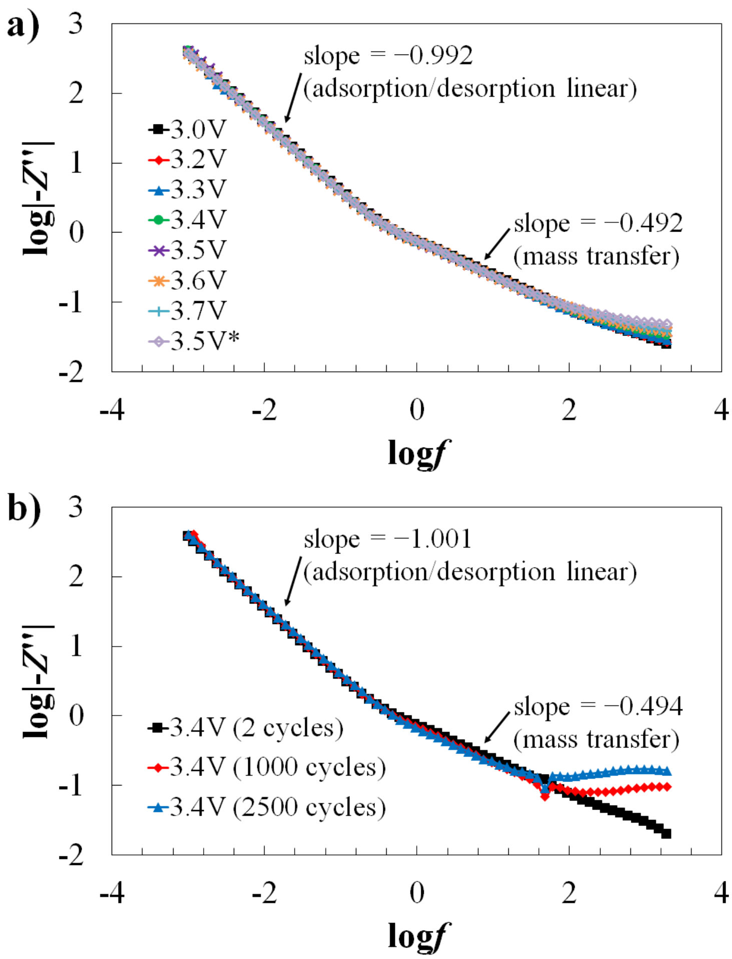

Figure 44. log│$-Z''$│ vs. log*f* plots in 1 M Et_3MeNBF_4 + AN electrolyte a) for a passivated system (measured from 0 to 3.7 V), b) for system at a fixed cell potential of 3.4 V, after 2, 1000, and 2500 cycles. * *denotes measurement after reaching 3.7 V.*

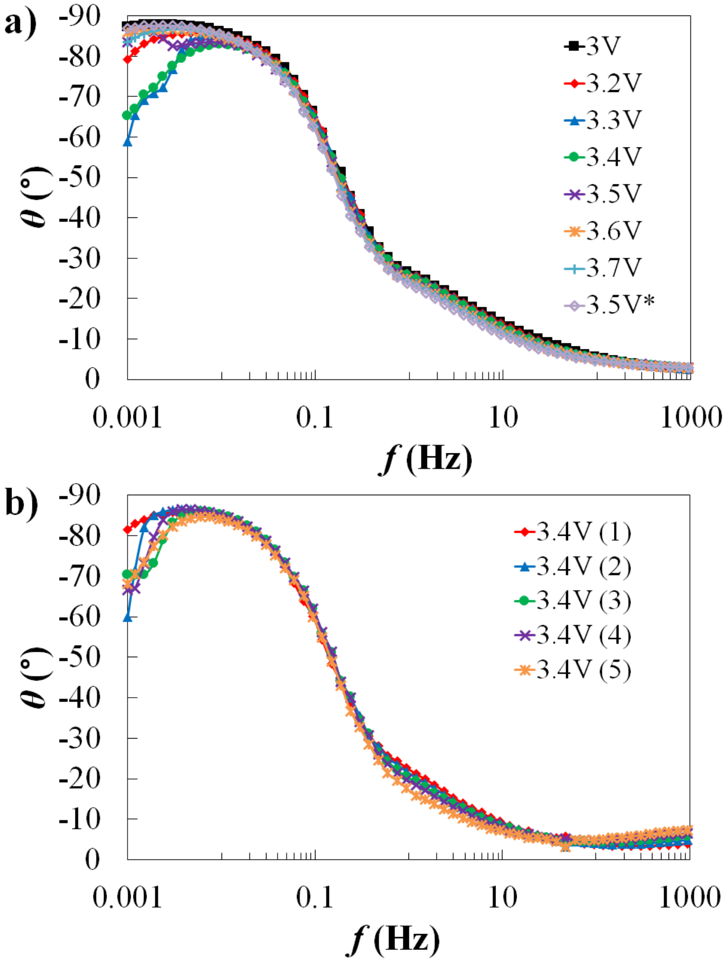

Figure 45. Phase angle vs. *ac* frequency dependencies for a system in 1 M Et_3MeNBF_4 + AN electrolyte a) subjected to selected potentials to passivation at 3.7 V and b) repeated impedance measurements after potential cycling up to maximum potential at 3.4 V. * *denotes measurement after reaching 3.7 V (a) and (1) – (5) in (b) denotes measurement after 500, 1000, 1500, 2000 and 2500 cycles at 50 mV* s^{-1}.

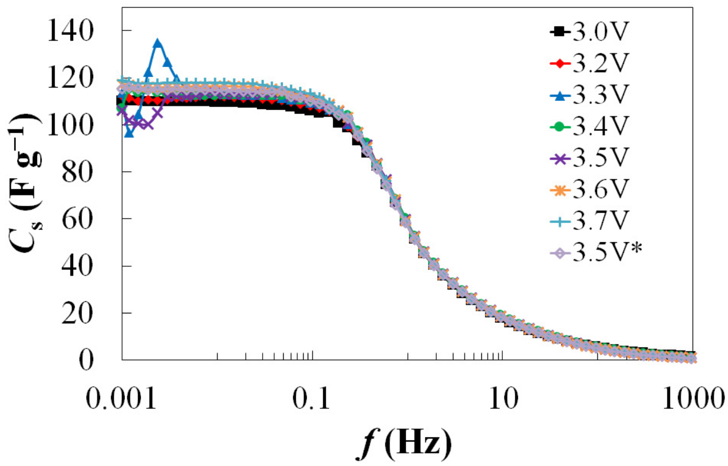

Figure 46. Specific series capacitance vs. *ac* frequency dependencies in 1 M Et_3MeNBF_4 + AN electrolyte.

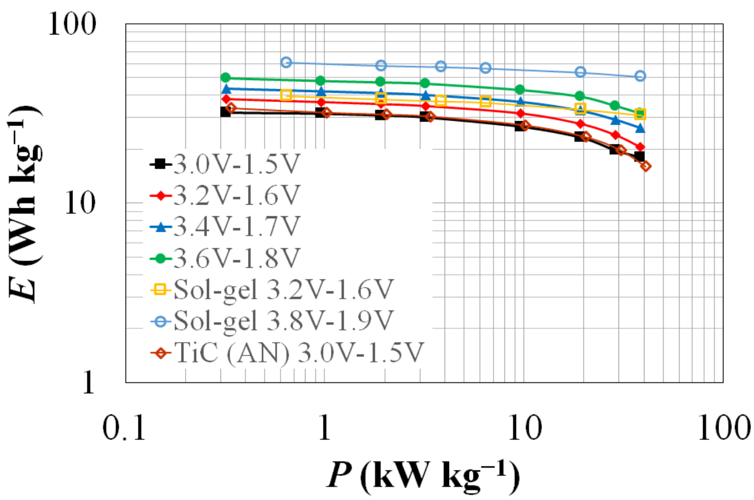

Figure 47. Ragone plots for the passivated system measured at different potential regions in 1 M Et_3MeNBF_4 + AN electrolyte

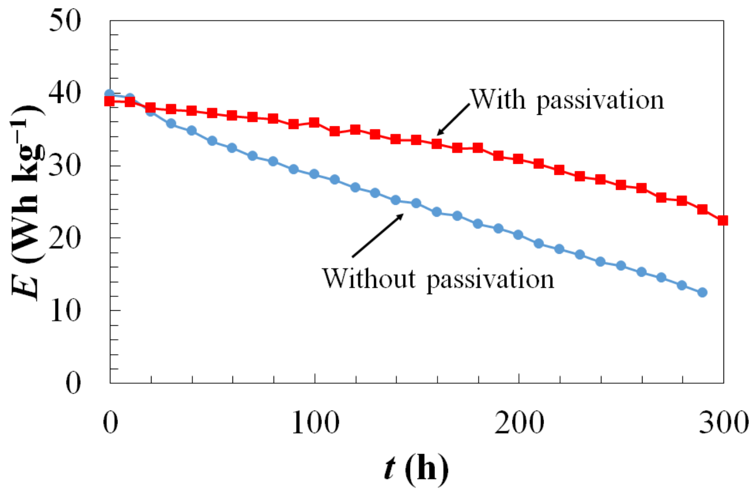

Figure 48. Energy densities calculated from the CCCD curves at 1 A g^{-1} measured from 0 to 3.4 V for the passivated and the non-passivated system in 1 M Et_3MeNBF_4 + AN electrolyte.

6.2.3. Results of spectroelectrochemical measurements

IR peaks characteristic of CH_3CNBF_3 and its decomposition products were not noticeable in the IR spectra (Fig. 49) differently from those measured at platinum electrode surface for tetra-n-butylammonium tetrafluoroborate ($TBABF_4$) oxidation at + 2 V (vs. Ag wire in 0.01 M $AgNO_3$ + 0.01 $TBABF_4$ in AN). Foley et al. concluded that the products formed are CH_3CNBF_3 and fluorinated acetonitrile [139].

Our data indicate that at the carbon electrodes the intermediates are either soluble in acetonitrile or therefore have been removed during the electrode washing process before FTIR measurements. Another possible explanation is that only very thin polymeric compound films have been formed at the most active carbon sites, however due to the very low surface concentration, not detectable by FTIR.

Fluorinated carbon IR peaks should appear within the range from ~1000 to 1100 cm^{-1}. However, based on the experimental details, carbon fluorination is unlikely to happen to a large extent because it can proceed only at much higher cell potentials than 3.7 V, but so high potentials have never been applied in this work [127,134,135,140]. This effect has previously been tested in the case of $EtMeIm^+BF_4^-$ systems [140]. Conducted infrared spectroscopy study (Fig. 49) only identified the anions and/or cations of $(C_2H_5)_3CH_3NBF_4$ salt in the porous carbon structure. The corresponding signal of BF_4^- peaks was stronger at a positively charged electrode and, thus, the amount of adsorbed BF_4^- ions were larger for passivated positively polarized electrode if compared with negatively polarized electrode data.

Raman spectroscopy data for the passivated positive electrode show some increase in the carbon G- and 2D-peak heights (Fig. 50), thus, indicating some increase in the relative amount of graphitized areas (probably due to dissolution of sp^3 amorphous carbon areas at high positive potentials) at the surface of passivated positively polarized carbon grains [129].

It may be concluded that careful repetitive overvoltage treatment at $\Delta E \geq 3.5$ V causes dissolution (through many oxidation/reduction steps) of some amorphous sp^3 carbon areas from the TiC-CDC surface and (relative) increase in the graphitic sp^2 carbon areas (Fig. 51). This effect has been systematically established in all 4 experiments conducted under identical experimental conditions, thus these results are statistically reproducible.

Similar effects were not observed at negatively passivated electrodes, and when the maximum potential did not exceed 3.2 V. Possibly the electrochemical oxidation/reduction reaction at high cell potentials eliminates electroactive surface trace groups from the porous carbon TiC-CDC surface, such as -Cl, -H, OH, =O, Si, Fe, etc [127,134,135,140–142]. The remaining cleaned TiC-CDC surface is more graphitic and therefore electrochemically less active [129] and higher cell potentials can be applied to the EDLC cell without initiating the fast faradaic processes. Due to reduction reactions and probable gas evolution taking place at the negatively overcharged electrode at $\Delta E > 3.7$ V, probably the PTFE binder degenerated at more high negative surface charge densities [130–133,141,142]. Thus, there is slow hydrogen evolution at negatively overcharged electrode [85,85,127,128,134,141,142,142,143], but only soluble (or very thin film) compound formation at the positively overcharged electrode, which explains why negatively charged electrode starts degrading somewhat faster than the positively charged electrode at cell potentials $\Delta E \geq 3.7$ V.

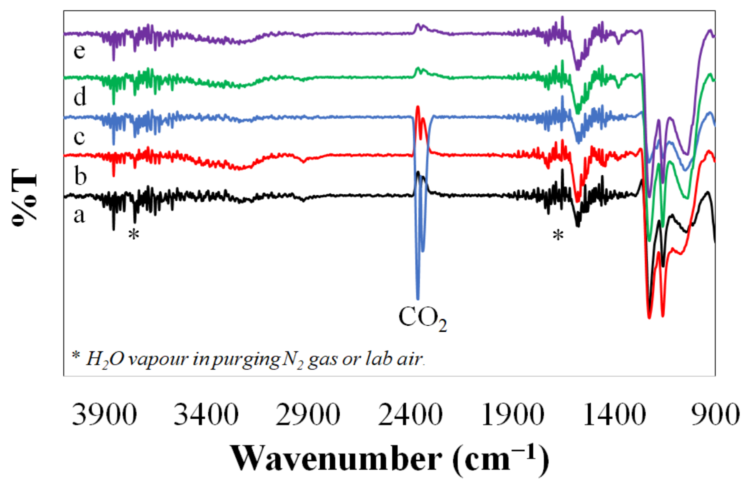

Figure 49. Baseline corrected IR spectra for a) regular electrode, b) positively charged electrode, and c) negatively charged electrode at a cell potential 3.2 V, d) positively charged electrode, and e) negatively charged electrode passivated at cell potential 3.7 V.

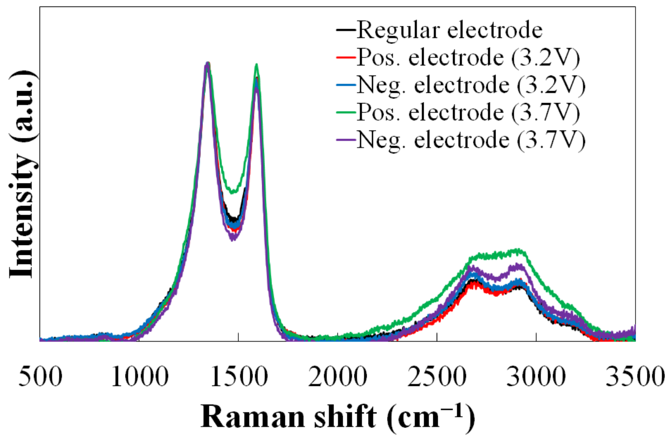

Figure 50. Raman spectra of regular, positively, and negatively charged electrodes at 3.2 V.

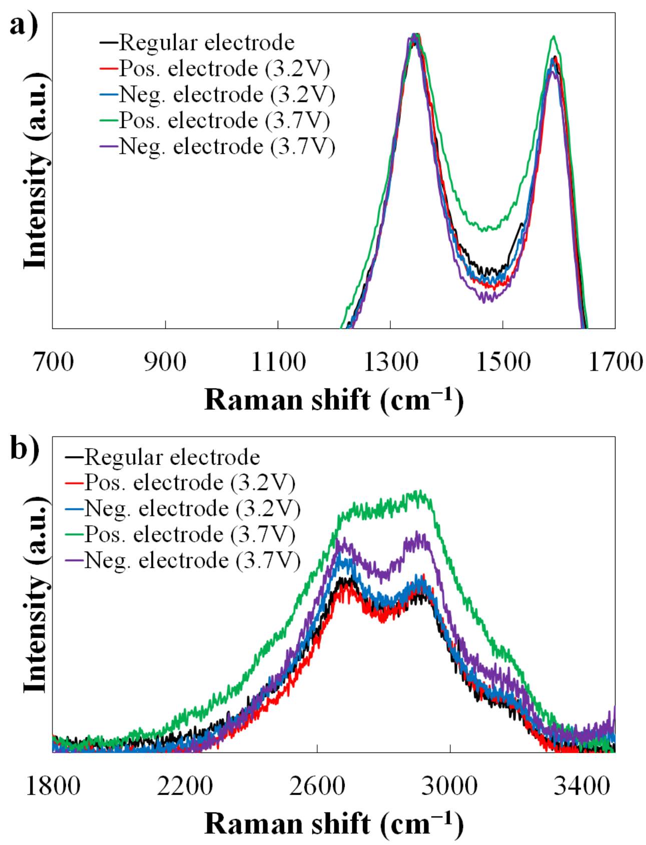

Figure 51. Zoom in of a) D- and G-peak and b) 2D-peak range of Raman spectra of regular, positively, and negatively charged electrode at 3.2 V.

SUMMARY

The sol-gel synthesis process was applied to prepare the titanium carbide (TiC) and titanium carbide/carbon nanotubes (CNT) composites. Samples with two different CNT wt% (1 wt% and 2 wt%) concentrations were prepared to study the possibilities to improve the electrochemical properties of the resulting carbide derived carbon (CDC) materials. Synthesized CDCs were used as electrode materials for very high power density supercapacitors.

Both the initial carbides and the final carbon material powders synthesized have micropores and mesopores. The density functional theory (DFT) specific surface area (S_{DFT}) values of the carbides vary between 152 and 274 $m^2 g^{-1}$. The synthesized CDCs have high S_{DFT} values, up to 1710 $m^2 g^{-1}$, which are somewhat higher values than usually obtained for chlorinated TiC-CDC (1350 – 1500 $m^2 g^{-1}$).

The addition of CNTs decreases the overall specific surface area, although the pore size distribution remains mostly unchanged. The increase in mesoporosity and S_{DFT} values may be caused by the non-stoichiometric structure of TiC and the existence of TiO_xC_{1-x} inside the raw carbide powder. The oxygen left inside the raw complex material as titanium oxycarbide is reacting with the formed carbon (forming CO_2 or CO) and as a result, a more porous hierarchical structure will be created.

The energy-related properties of the electrical double layer capacitors (EDLCs) based on 1-ethyl-3-methylimidazolium tetrafluoroborate ($EtMeImBF_4$) ionic liquid and 1 M triethylmethylammonium tetrafluoroborate (Et_3MeNBF_4) in acetonitrile (AN) electrolytes and on the electrode materials synthesized from sol-gel titanium carbide derived carbon (SgTiC-CDC) were investigated using the cyclic voltammetry (CV), galvanostatic charge/discharge (CCCD), electrochemical impedance spectroscopy (EIS) and constant power (CP) discharge methods.

CV data show that completed EDLCs demonstrate practically ideal capacitive behaviour at cell potential (ΔE) up to $\Delta E \leq 3.6$ V and at potential scan rates (v) up to $v \leq 500$ mV s^{-1}.

Very high specific series capacitance (C_s) value of 176 F g^{-1} at $\Delta E = 3.6$ V (155 F g^{-1} at $\Delta E = 3.2$ V) for $EtMeImBF_4$ system has been established. The electrochemical measurements data indicate that even at very high potential scan rates ($v \leq 500$ mV s^{-1}), there is no significant potential drop in the porous CDC matrix. This is probably caused by the extra developed mesoporosity because the sol-gel synthesis provides some amount of additional mesopores (from 4 to 10 nm). The highest specific series capacitance values from EIS data were obtained for the carbon material without CNT addition; $C_s = 176$ F g^{-1} for $EtMeImBF_4$ at $\Delta E = 3.6$ V and $C_s = 145$ F g^{-1} for 1 M Et_3MeNBF_4 + AN at $\Delta E = 3.0$ V. A little bit lower capacitance values have been observed if compared with materials that have CNT addition in a raw paste. Phase angle values above

−85° for all materials (at low frequencies) indicate that nearly ideally polarizable EDLCs have been completed and tested.

The calculated energy efficiency values vary within the range from 93% to 97% (at charging current density 1 A g^{-1}), while the calculated coulombic efficiency values exceed 99%. Very high specific power (> 100 kW kg^{-1}) at high specific energy (30 Wh kg^{-1}) has been achieved for 1 M Et_3MeNBF_4 + AN based EDLCs. For $EtMeImBF_4$ based EDLC somewhat lower specific energy 10 Wh kg^{-1} at specific power 100 kW kg^{-1} has been established.

Thus, in addition to optimised mesoporosity of the electrode material, the electrolyte viscosity should be reduced, and conductivity should be increased for very high energy density devices at extremely high power densities.

Also, it was demonstrated that it is possible to stabilize the EDLC based on TiC-CDC electrodes in 1 M Et_3MeNBF_4+ AN at cell potentials higher than 3.4 V if careful electrochemical pre-treatment of the system (step by step widening of potential cycling region and repetitive CV polarization up to 3.7 V) has been applied. The passivation effect can be explained by oxidation/reduction (electrochemical elimination of functional active groups from carbon surface) of the more amorphous and active sites, i.e., electrochemical dissolution of more active carbon sites from TiC-CDC surface and enrichment of the surface with more stable graphitic sp^2 regions or by the formation of the thin passive polymeric films.

The exact mechanism for the stabilization/passivation phenomenon cannot be determined in this PhD work but is definitely going to be studied in more detail using long-lasting cell potential cycling experiments applying in situ FTIR or by secondary ion mass spectrometry and synchrotron radiation based XPS methods. EDLCs with such high cell potential might not have the same very long-lasting stability as the current commercial supercapacitors (cell potential lower than 3.0 V), but they surpass the commercial EDLCs significantly in energy and power densities. These EDLCs can be used for applications, where extremely high power densities are inevitable.

REFERENCES

[1] S. O. Amrouche, D. Rekioua, T. Rekioua, S. Bacha, Overview of energy storage in renewable energy systems, Int. J. Hydrog. Energ. 41 (2016) 20914–20927. https://doi.org/10.1016/j.ijhydene.2016.06.243.

[2] W. Zuo, R. Li, C. Zhou, Y. Li, J. Xia, J. Liu, Battery-supercapacitor hybrid devices: recent progress and future prospects, Adv. Sci. 4 (2017). https://doi.org/10.1002/advs.201600539.

[3] H. D. Yoo, E. Markevich, G. Salitra, D. Sharon, D. Aurbach, On the challenge of developing advanced technologies for electrochemical energy storage and conversion, Mater. Today 17 (2014) 110–121. https://doi.org/10.1016/j.mattod.2014.02.014.

[4] M. M. Baig, I. H. Gul, S. M. Baig, F. Shahzad, The complementary advanced characterization and electrochemical techniques for electrode materials for supercapacitors, J. Energy Storage 44 (2021) 103370. https://doi.org/10.1016/j.est.2021.103370.

[5] S. Karthikeyan, B. Narenthiran, A. Sivanantham, L. D. Bhatlu, T. Maridurai, Supercapacitor: evolution and review, Mater. Today Proc. 46 (2021) 3984–3988. https://doi.org/10.1016/j.matpr.2021.02.526.

[6] B. E. Conway, Electrochemical supercapacitors: scientific fundamentals and technological applications, 1st ed., Springer US, 1999.

[7] A. Burke, Ultracapacitors: why, how, and where is the technology?, J. Power Sources 91 (2000) 37–50. https://doi.org/10.1016/S0378-7753(00)00485-7.

[8] R. Kötz, M. Carlen, Principles and applications of electrochemical capacitors, Electrochim. Acta 45 (2000) 2483–2498. https://doi.org/10.1016/S0013-4686(00)00354-6.

[9] P. Simon, Y. Gogotsi, Materials for electrochemical capacitors, Nat. Mater. 7 (2008) 845–854. https://doi.org/10.1038/nmat2297.

[10] A. Burke, M. Miller, The power capability of ultracapacitors and lithium batteries for electric and hybrid vehicle applications, J. Power Sources 196 (2011) 514–522. https://doi.org/10.1016/j.jpowsour.2010.06.092.

[11] J. R. Miller, P. Simon, Electrochemical capacitors for energy management, Science 321 (2008) 651–652. https://doi.org/10.1126/science.1158736.

[12] G. Salitra, A. Soffer, L. Eliad, Y. Cohen, D. Aurbach, Carbon electrodes for double-layer capacitors I. Relations between ion and pore dimensions, J. Electrochem. Soc. 147 (2000) 2486–2493. https://doi.org/10.1149/1.1393557.

[13] J. B. Goodenough, Energy storage materials: A perspective, Energy Storage Mater. 1 (2015) 158–161. https://doi.org/10.1016/j.ensm.2015.07.001.

[14] S. C. Singhal, Solid oxide fuel cells for power generation, Wiley Interdiscip. Rev. Energy Environ. 3 (2014) 179–194. https://doi.org/10.1002/wene.96.

[15] J. Y. Hwang, S. T. Myung, Y. K. Sun, Sodium-ion batteries: present and future, Chem. Soc. Rev. (2017). https://doi.org/10.1039/C6CS00776G.

[16] M. Mirzaeian, Q. Abbas, A. Ogwu, P. Hall, M. Goldin, M. Mirzaeian, H. F. Jirandehi, Electrode and electrolyte materials for electrochemical capacitors, Int. J. Hydrog. Energy 42 (2017) 25565–25587. https://doi.org/10.1016/j.ijhydene.2017.04.241.

[17] F. Beguin, E. Frackowiak, Supercapacitors: Materials, systems and applications, John Wiley & Sons, 2013.

[18] A. G. Pandolfo, A. F. Hollenkamp, Carbon properties and their role in supercapacitors, J. Power Sources 157 (2006) 11–27. https://doi.org/16/j.jpowsour.2006.02.065.
[19] H. Chen, T. N. Cong, W. Yang, C. Tan, Y. Li, Y. Ding, Progress in electrical energy storage system: A critical review, Prog. Nat. Sci. 19 (2009) 291–312. https://doi.org/10.1016/j.pnsc.2008.07.014.
[20] M. Winter, R. J. Brodd, What are batteries, fuel cells, and supercapacitors?, Chem. Rev. 104 (2004) 4245–4270. https://doi.org/10.1021/cr020730k.
[21] B. E. Conway, Transition from supercapacitor to battery behavior in electrochemical energy storage, J. Electrochem. Soc. 138 (1991) 1539–1548. https://doi.org/10.1149/1.2085829.
[22] B. E. Conway, W. G. Pell, Power limitations of supercapacitor operation associated with resistance and capacitance distribution in porous electrode devices, J. Power Sources 105 (2002) 169–81. https://doi.org/10.1016/S0378-7753(01)00936-3.
[23] P. R. Bandaru, H. Yamada, R. Narayanan, M. Hoefer, Charge transfer and storage in nanostructures, Mater. Sci. Eng. R Rep. 96 (2015) 1–69. https://doi.org/10.1016/j.mser.2015.06.001.
[24] M. Salanne, B. Rotenberg, K. Naoi, K. Kaneko, P. L. Taberna, C. P. Grey, B. Dunn, P. Simon, Efficient storage mechanisms for building better supercapacitors, Nat. Energy 1 (2016) 16070. https://doi.org/10.1038/nenergy.2016.70.
[25] Y. Gogotsi, A. Nikitin, H. Ye, W. Zhou, J. E. Fischer, B. Yi, H. C. Foley, M. W. Barsoum, Nanoporous carbide-derived carbon with tunable pore size, Nat. Mater. 2 (2003) 591–594. https://doi.org/10.1038/nmat957.
[26] E. Frackowiak, F. Beguin, Carbon materials for the electrochemical storage of energy in capacitors, Carbon 39 (2001) 937–950. https://doi.org/10.1016/S0008-6223(00)00183-4.
[27] J. Chmiola, C. Largeot, P. L. Taberna, P. Simon, Y. Gogotsi, Desolvation of ions in subnanometer pores and its effect on capacitance and double-layer theory, Angew. Chem. Int. Ed. 47 (2008) 3392–3395. https://doi.org/10.1002/anie.200704894.
[28] C. F. Liu, Y. C. Liu, T. Y. Yi, C. C. Hu, Carbon materials for high-voltage supercapacitors, Carbon 145 (2019) 529–548. https://doi.org/10.1016/j.carbon.2018.12.009.
[29] M. Anouti, E. Couadou, L. Timperman, H. Galiano, Protic ionic liquid as electrolyte for high-densities electrochemical double layer capacitors with activated carbon electrode material, Electrochim. Acta 64 (2012) 110–117. https://doi.org/10.1016/j.electacta.2011.12.120.
[30] A. Lewandowski, M. Galinski, Practical and theoretical limits for electrochemical double-layer capacitors, J. Power Sources 173 (2007) 822–828.
[31] S. Sakka, ed., Handbook of sol-gel science and technology: processing, characterization and applications. Volume I, Sol-gel, Kluwer Academic Publishers, 2005.
[32] C. J. Brinker, G. W. Scherer, Sol-Gel Science: The physics and chemistry of sol-gel processing, Academic Press, San Diego, 1990.
[33] S. Bi, L. Ma, B. Mei, Q. Tian, C. Liu, C. Zhong, Y. Xiao, Silicon carbide/carbon nanotube heterostructures: Controllable synthesis, dielectric properties and microwave absorption, Adv. Powder Technol. 25 (2014) 1273–1279.

[34] C. Zhang, L. Gao, Y. Chen, Fabrication of ceramic oxide-coated SWNT composites by sol–gel process with a polymer glue, J. Nanoparticle Res. 13 (2011) 3731–3740. https://doi.org/10.1007/s11051-011-0295-1.
[35] A. E. Danks, S. R. Hall, Z. Schnepp, The evolution of ′sol–gel′ chemistry as a technique for materials synthesis, Mater. Horiz. 3 (2016) 91–112. https://doi.org/10.1039/C5MH00260E.
[36] H. Preiss, L. M. Berger, D. Schultze, Studies on the carbothermal preparation of titanium carbide from different gel precursors, J. Eur. Ceram. Soc. 19 (1999) 195–206. https://doi.org/10.1016/S0955-2219(98)00190-3.
[37] J. D. Wright, N. A. J. M. Sommerdijk, Sol-gel materials chemistry and applications, CRC Press, 2000.
[38] C. Giordano, M. Antonietti, Synthesis of crystalline metal nitride and metal carbide nanostructures by sol–gel chemistry, Nano Today 6 (2011) 366–380. https://doi.org/10.1016/j.nantod.2011.06.002.
[39] B. Gaweł, K. Gaweł, G. Øye, Sol-Gel synthesis of non-silica monolithic materials, Materials 3 (2010) 2815–2833. https://doi.org/10.3390/ma3042815.
[40] J. Livage, M. M. Henry, C. Sánchez Sánchez, Sol-gel chemistry of transition metal oxides, Prog. Solid State Chem. (1988). https://doi.org/10.1016/0079-6786(88)90005-2.
[41] V. G. Kessler, The chemistry behind the sol–gel synthesis of complex oxide nanoparticles for bio-imaging applications, J. Sol-Gel Sci. Technol. 51 (2009) 264. https://doi.org/10.1007/s10971-009-1946-x.
[42] J. Zhong, S. Liang, J. Zhao, D. Wu, W. Liu, H. Wang, X.D. Chen, Y. Cheng, Formation of novel mesoporous TiC microspheres through a sol-gel and carbothermal reduction process, J. Eur. Ceram. Soc. 32 (2012) 3407–3414. https://doi.org/10.1016/j.jeurceramsoc.2012.04.047.
[43] M. Dolle, D. Gosset, D. Simeone, C. Bogicevic, F. Karolak, G. Baldinozzi, Synthesis of nano-sized zirconium carbide by a sol-gel route, J. Eur. Ceram. Soc. 27 (2007) 2061–2067. https://doi.org/10.1016/j.jeurceramsoc.2006.06.005.
[44] H. O. Pierson, Handbook of refractory carbides and nitrides: properties, characteristics, processing and applications, Noyes Publications, 1996.
[45] L. Berger, W. Gruner, E. Langholf, S. Stolle, On the mechanism of carbothermal reduction processes of TiO_2 and ZrO_2, Int. J. Refract. Hard Met. 17 (1999). https://doi.org/10.1016/S0263-4368(98)00077-8.
[46] W. Schmickler, Electrochemical theory: double layer, in: Ref. Module Chem. Mol. Sci. Chem. Eng., Elsevier, 2014. https://doi.org/10.1016/B978-0-12-409547-2.11149-7.
[47] A. Tyagi, R. Gupta, Carbon nanostructures from biomass waste for supercapacitor applications, in: Nanomaterials, CRC Press, 2016. https://doi.org/10.1201/b19168-11.
[48] E. Frackowiak, Q. Abbas, F. Béguin, Carbon/carbon supercapacitors, J. Energy Chem. 22 (2013) 226–240. https://doi.org/10.1016/S2095-4956(13)60028-5.
[49] S. Amokrane, J. P. Badiali, A new analysis of the differential capacitance of an ideally polarized electrode, J. Electroanal. Chem. Interfacial Electrochem. 266 (1989) 21–35. https://doi.org/10.1016/0022-0728(89)80212-8.
[50] S. Trasatti, E. Lust, The Potential of Zero Charge, in: Mod. Asp. Electrochem., Springer US, 1999. https://doi.org/10.1007/0-306-46917-0_1.

[51] M. A. Vorotyntsev, A. A. Kornyshev, Models to describe collective properties of the metal/solvent interface in electric double-layer theory, Russ. J. Electrochem. 20 (1984) 3–47.
[52] E. Lust, A. Jänes, V. Sammelselg, P. Miidla, K. Lust, Surface roughness of bismuth, antimony and cadmium electrodes, Electrochim. Acta 44 (1998) 373–383. https://doi.org/10.1016/S0013-4686(98)00084-X.
[53] A. K. Samantara, S. Ratha, Historical background and present status of the supercapacitors, in: Mater. Dev. Act. Compon. Supercapacitor, Springer, 2018. https://doi.org/10.1007/978-981-10-7263-5_2.
[54] N. A. Choudhury, S. Sampath, A. K. Shukla, Hydrogel-polymer electrolytes for electrochemical capacitors: an overview, Energy Environ. Sci. 2 (2008) 55–67. https://doi.org/10.1039/B811217G.
[55] S. Kulandaivalu, Y. Sulaiman, Recent advances in layer-by-layer assembled conducting polymer based composites for Ssupercapacitors, Energies 12 (2019) 2107. https://doi.org/10.3390/en12112107.
[56] C. Zhong, Y. Deng, W. Hu, J. Qiao, L. Zhang, J. Zhang, A review of electrolyte materials and compositions for electrochemical supercapacitors, Chem. Soc. Rev. 44 (2015) 7484–7539. https://doi.org/10.1039/C5CS00303B.
[57] J. Zhao, A. F. Burke, Electrochemical capacitors: Performance metrics and evaluation by testing and analysis, Adv. Energy Mater. 11 (2021) 2002192. https://doi.org/10.1002/aenm.202002192.
[58] F. Béguin, V. Presser, A. Balducci, E. Frackowiak, Carbons and electrolytes for advanced supercapacitors, Adv. Mater. 26 (2014) 2219–2251. https://doi.org/10.1002/adma.201304137.
[59] F. Wang, X. Wu, X. Yuan, Z. Liu, Y. Zhang, L. Fu, Y. Zhu, Q. Zhou, Y. Wu, W. Huang, Latest advances in supercapacitors: from new electrode materials to novel device designs, Chem. Soc. Rev. 46 (2017) 6816–6854. https://doi.org/10.1039/C7CS00205J.
[60] C. Schütter, S. Pohlmann, A. Balducci, Industrial requirements of materials for electrical double layer capacitors: impact on current and future applications, Adv. Energy Mater. 9 (2019) 1900334. https://doi.org/10.1002/aenm.201900334.
[61] N. Abdul Manaf, M. S. A. Bistamam, M. A. Azam, Development of high performance electrochemical capacitor: a systematic review of electrode fabrication technique based on different carbon materials, J. Solid State Sci. Technol. 2 (2013) M3101–M3119. https://doi.org/10.1149/2.014310jss.
[62] Y. Gogotsi, Nanomaterials Handbook, CRC Press, 2006.
[63] M. Pohl, H. Kurig, I. Tallo, A. Jänes, E. Lust, Novel sol-gel synthesis route of carbide-derived carbon composites for very high power density supercapacitors, Chem. Eng. J. 320 (2017) 576–587. https://doi.org/10.1016/j.cej.2017.03.081.
[64] M. Paalo, I. Tallo, T. Thomberg, A. Jänes, E. Lust, Enhanced power performance of highly mesoporous sol-gel TiC derived carbons in ionic liquid and non-aqueous electrolyte based capacitors, J. Electrochem. Soc. 166 (2019) A2887–A2895. https://doi.org/10.1149/2.0721913jes.
[65] R. Härmas, R. Palm, M. Härmas, M. Pohl, H. Kurig, I. Tallo, E. Tee, I. Vaas, R. Väli, T. Romann, O. Oll, R. Kanarbik, K. Liivand, J. Eskusson, J. Kruusma, T. Thomberg, A. Jänes, P. Miidla, E. Lust, Influence of porosity parameters and electrolyte chemical composition on the power densities of non-aqueous and ionic liquid based supercapacitors, Electrochim. Acta 283 (2018) 931–948. https://doi.org/10.1016/j.electacta.2018.06.115.

[66] K. Tõnurist, T. Thomberg, A. Jänes, T. Romann, V. Sammelselg, E. Lust, Influence of separator properties on electrochemical performance of electrical double-layer capacitors, J. Electroanal. Chem. 689 (2013) 8–20. https://doi.org/10.1016/j.jelechem.2012.11.024.
[67] H. P. Klug, L. E. Alexander, X-Ray diffraction procedures: for polycrystalline and amorphous materials, 2nd ed., Wiley, New Yoirk, 1974.
[68] B. Manoj, A. G. Kunjomana, Study of stacking structure of amorphous carbon by X-ray diffraction technique, Int. J. Electrochem. Sci. 7 (2012) 3127–3134.
[69] A. Jänes, T. Thomberg, H. Kurig, E. Lust, Nanoscale fine-tuning of porosity of carbide-derived carbon prepared from molybdenum carbide, Carbon 47 (2009) 23–29. https://doi.org/10.1016/j.carbon.2008.07.010.
[70] M. Härmas, T. Thomberg, H. Kurig, T. Romann, A. Jänes, E. Lust, Microporous–mesoporous carbons for energy storage synthesized by activation of carbonaceous material by zinc chloride, potassium hydroxide or mixture of them, J. Power Sources 326 (2016) 624–634. https://doi.org/10.1016/j.jpowsour.2016.04.038.
[71] T. Thomberg, H. Kurig, A. Jänes, E. Lust, Mesoporous carbide-derived carbons prepared from different chromium carbides, Microporous Mesoporous Mater. 141 (2011) 88–93. https://doi.org/10.1016/j.micromeso.2010.11.006.
[72] R. Härmas, R. Palm, H. Kurig, L. Puusepp, T. Pfaff, T. Romann, J. Aruväli, I. Tallo, T. Thomberg, A. Jänes, E. Lust, Carbide-derived carbons: WAXS and Raman spectra for detailed structural analysis, C. 7 (2021) 29. https://doi.org/10.3390/c7010029.
[73] P. Mallet-Ladeira, P. Puech, C. Toulouse, M. Cazayous, N. Ratel-Ramond, P. Weisbecker, G.L. Vignoles, M. Monthioux, A Raman study to obtain crystallite size of carbon materials: a better alternative to the Tuinstra–Koenig law, Carbon 80 (2014) 629–639. https://doi.org/10.1016/j.carbon.2014.09.006.
[74] A. C. Ferrari, Raman spectroscopy of graphene and graphite: Disorder, electron–phonon coupling, doping and nonadiabatic effects, Solid State Commun. 143 (2007) 47–57. https://doi.org/10.1016/j.ssc.2007.03.052.
[75] R. R. Jones, D. C. Hooper, L. Zhang, D. Wolverson, V. K. Valev, Raman techniques: fundamentals and frontiers, Nanoscale Res. Lett. 14 (2019) 231. https://doi.org/10.1186/s11671-019-3039-2.
[76] S. Lowell, J. E. Shields, M. A. Thomas, M. Thommes, Characterization of porous solids and powders: surface area, pore size and density, Kluwer Academic Publishers, 2004.
[77] J. Condon, Surface area and porosity determinations by physisorption, Elsevier, 2006.
[78] M. Thommes, K. Kaneko, A. V. Neimark, J. P. Olivier, F. Rodriguez-Reinoso, J. Rouquerol, K. S. W. Sing, Physisorption of gases, with special reference to the evaluation of surface area and pore size distribution (IUPAC Technical Report), Pure Appl. Chem. 87 (2015) 1051–1069. https://doi.org/10.1515/pac-2014-1117.
[79] A. M. Puziy, O. I. Poddubnaya, B. Gawdzik, M. Sobiesiak, Comparison of heterogeneous pore models QSDFT and 2D-NLDFT and computer programs ASiQwin and SAIEUS for calculation of pore size distribution, Adsorption 22 (2016) 459–464. https://doi.org/10.1007/s10450-015-9704-6.
[80] J. Jagiello, Stable numerical solution of the adsorption integral equation using splines, Langmuir 10 (1994) 2778–2785. https://doi.org/10.1021/la00020a045.

[81] J. Jagiello, J. P. Olivier, Carbon slit pore model incorporating surface energetical heterogeneity and geometrical corrugation, Adsorption 19 (2013) 777–783. https://doi.org/10.1007/s10450-013-9517-4.
[82] N. Elgrishi, K. J. Rountree, B. D. McCarthy, E. S. Rountree, T. T. Eisenhart, J. L. Dempsey, A practical beginner's guide to cyclic voltammetry, J. Chem. Educ. 95 (2018) 197–206. https://doi.org/10.1021/acs.jchemed.7b00361.
[83] J. Heinze, Cyclic voltammetry − "electrochemical spectroscopy". New analytical methods (25), Angew. Chem. Int. Ed. Engl. 23 (1984) 831–847. https://doi.org/10.1002/anie.198408313.
[84] L. E. Helseth, Comparison of methods for finding the capacitance of a supercapacitor, J. Energy Storage 35 (2021) 102304. https://doi.org/10.1016/j.est.2021.102304.
[85] H. Kurig, A. Jänes, E. Lust, Electrochemical characteristics of carbide-derived carbon | 1 -ethyl-3-methylimidazolium tetrafluoroborate supercapacitor cells, J. Electrochem. Soc. 157 (2010) A272–A279. https://doi.org/10.1149/1.3274208.
[86] A. Jänes, H. Kurig, E. Lust, Characterisation of activated nanoporous carbon for supercapacitor electrode materials, Carbon 45 (2007) 1226–1233. https://doi.org/10.1016/j.carbon.2007.01.024.
[87] P. L. Taberna, P. Simon, J. F. Fauvarque, Electrochemical characteristics and impedance spectroscopy studies of carbon-carbon supercapacitors, J. Electrochem. Soc. 150 (2003) A292–A300. https://doi.org/10.1149/1.1543948.
[88] E. Gileadi, Electrode kinetics for chemists, chemical engineers and materials scientists, Wiley, 1993.
[89] J. Chmiola, G. Yushin, R. Dash, Y. Gogotsi, Effect of pore size and surface area of carbide derived carbons on specific capacitance, J. Power Sources 158 (2006) 765–772. https://doi.org/10.1016/j.jpowsour.2005.09.008.
[90] M. Oschatz, E. Kockrick, M. Rose, L. Borchardt, N. Klein, I. Senkovska, T. Freudenberg, Y. Korenblit, G. Yushin, S. Kaskel, A cubic ordered, mesoporous carbide-derived carbon for gas and energy storage applications, Carbon 48 (2010) 3987–3992. https://doi.org/10.1016/j.carbon.2010.06.058.
[91] A. Laheäär, P. Przygocki, Q. Abbas, F. Béguin, Appropriate methods for evaluating the efficiency and capacitive behavior of different types of supercapacitors, Electrochem. Commun. 60 (2015) 21–25. https://doi.org/10.1016/j.elecom.2015.07.022.
[92] A. J. Bard, L. R. Faulkner, Electrochemical methods: fundamentals and applications, 2nd Ed., Wiley, 2000.
[93] M. E. Orazem, B. Tribollet, Electrochemical impedance spectroscopy, John Wiley & Sons, 2011.
[94] V. S. Bagotsky, Fundamentals of electrochemistry, John Wiley & Sons, 2005.
[95] C. M. A. Brett, A. M. O. Brett, Electrochemistry: principles, methods, and applications, Oxford University Press, 1993.
[96] E. Barsoukov, J. R. Macdonald, Impedance spectroscopy: theory, experiment, and applications, Wiley, John & Sons, 2005.
[97] M. Eikerling, A. A. Kornyshev, E. Lust, Optimized structure of nanoporous carbon-based double-layer capacitors, J. Electrochem. Soc. 152 (2005) E24–E33. https://doi.org/10.1149/1.1825379.
[98] J. B. Jorcin, M. E. Orazem, N. Pébère, B. Tribollet, CPE analysis by local electrochemical impedance spectroscopy, Electrochim. Acta 51 (2006) 1473–1479. https://doi.org/10.1016/j.electacta.2005.02.128.

[99] Q. Y. Li, H. Q. Wang, Q. F. Dai, J. H. Yang, Y. L. Zhong, Novel activated carbons as electrode materials for electrochemical capacitors from a series of starch, Solid State Ion. 179 (2008) 269–273. https://doi.org/10.1016/j.ssi.2008.01.085.
[100] F. Scholz, Electroanalytical methods: guide to experiments and applications, Springer, 2009.
[101] S. C. Lee, W. Y. Jung, Analogical understanding of the Ragone plot and a new categorization of energy devices, Energy Procedia. 88 (2016) 526–530. https://doi.org/10.1016/j.egypro.2016.06.073.
[102] T. Christen, M. W. Carlen, Theory of Ragone plots, J. Power Sources 91 (2000) 210–216. https://doi.org/10.1016/S0378-7753(00)00474-2.
[103] S. A. Rezan, G. Zhang, O. Ostrovski, Effect of gas atmosphere on carbothermal reduction and nitridation of titanium dioxide, Metall. Mater. Trans. B. 43 (2012) 73–81. https://doi.org/10.1007/s11663-011-9574-6.
[104] A. Ferrari, J. Robertson, Interpretation of Raman spectra of disordered and amorphous carbon, Mater. Sci. Phys. Rev. B. 61 (2000) 14095–14107. https://doi.org/10.1103/PHYSREVB.61.14095.
[105] F. Stoeckli, T. A. Centeno, On the determination of surface areas in activated carbons, Carbon 43 (2005) 1184–1190. https://doi.org/10.1016/j.carbon.2004.12.010.
[106] H. Kurig, M. Russina, I. Tallo, M. Siebenbürger, T. Romann, E. Lust, The suitability of infinite slit-shaped pore model to describe the pores in highly porous carbon materials, Carbon 100 (2016) 617–624. https://doi.org/10.1016/j.carbon.2016.01.061.
[107] J. Jagiello, C. Ania, J. Parra, C. Cook, Dual gas analysis of microporous carbons using 2D-NLDFT heterogeneous surface model and combined adsorption data of N_2 and CO_2, Carbon 91 (2015) 330–337. https://doi.org/10.1016/j.carbon.2015.05.004.
[108] J. Jagiello, J. P. Olivier, 2D-NLDFT adsorption models for carbon slit-shaped pores with surface energetical heterogeneity and geometrical corrugation, Carbon 55 (2013) 70–80. https://doi.org/10.1016/j.carbon.2012.12.011.
[109] B. Jiang, K. Huang, Z. Cao, H. Zhu, Thermodynamic study of titanium oxycarbide, Metall. Mater. Trans. A. 43 (2012). https://doi.org/10.1007/s11661-011-1032-1.
[110] E. Tee, I. Tallo, H. Kurig, T. Thomberg, A. Jänes, E. Lust, Huge enhancement of energy storage capacity and power density of supercapacitors based on the carbon dioxide activated microporous SiC-CDC, Electrochim. Acta 161 (2015) 364–370. https://doi.org/10.1016/j.electacta.2015.02.106.
[111] M. A. Pimenta, G. Dresselhaus, M. S. Dresselhaus, L. G. Cançado, A. Jorio, R. Saito, Studying disorder in graphite-based systems by Raman spectroscopy, Phys. Chem. Chem. Phys. 9 (2007) 1276–1290. https://doi.org/10.1039/B613962K.
[112] T. Thomberg, T. Tooming, T. Romann, R. Palm, A. Jänes, E. Lust, High power density supercapacitors based on the carbon dioxide activated D-glucose derived carbon electrodes and acetonitrile electrolyte, J. Electrochem. Soc. 160 (2013) A1834. https://doi.org/10.1149/2.091310jes.
[113] M. Härmas, T. Thomberg, T. Romann, A. Jänes, E. Lust, Carbon for energy storage derived from granulated white sugar by hydrothermal carbonization and

subsequent zinc chloride activation, J. Electrochem. Soc. 164 (2017) A1866–A1872. https://doi.org/10.1149/2.0681709jes.
[114] A. Jänes, L. Permann, M. Arulepp, E. Lust, Electrochemical characteristics of nanoporous carbide-derived carbon materials in non-aqueous electrolyte solutions, Electrochem. Commun. 6 (2004) 313–318. https://doi.org/10.1016/j.elecom.2004.01.009.
[115] Y. Korenblit, M. Rose, E. Kockrick, L. Borchardt, A. Kvit, S. Kaskel, G. Yushin, High-rate electrochemical capacitors based on ordered mesoporous silicon carbide-derived carbon, ACS Nano. 4 (2010) 1337–1344. https://doi.org/10.1021/nn901825y.
[116] M. Oschatz, M. Zeiger, N. Jäckel, P. Strubel, L. Borchardt, R. Reinhold, W. Nickel, J. Eckert, V. Presser, S. Kaskel, Emulsion soft templating of carbide-derived carbon nanospheres with controllable porosity for capacitive electrochemical energy storage, J. Mater. Chem. A. 3 (2015) 17983–17990. https://doi.org/10.1039/C5TA03730A.
[117] W. Nickel, M. Oschatz, M. von der Lehr, M. Leistner, G. P. Hao, P. Adelhelm, P. Müller, B. M. Smarsly, S. Kaskel, Direct synthesis of carbide-derived carbon monoliths with hierarchical pore design by hard-templating, J. Mater. Chem. A. 2 (2014) 12703–12707. https://doi.org/10.1039/C4TA02260B.
[118] C. Portet, Z. Yang, Y. Korenblit, Y. Gogotsi, R. Mokaya, G. Yushin, Electrical double-layer capacitance of zeolite-templated carbon in organic electrolyte, J. Electrochem. Soc. 156 (2009) A1. https://doi.org/10.1149/1.3002375.
[119] I. Tallo, T. Thomberg, H. Kurig, A. Jänes, K. Kontturi, E. Lust, Supercapacitors based on carbide-derived carbons synthesised using HCl and Cl2 as reactants, J. Solid State Electrochem. 17 (2013) 19–28. https://doi.org/10.1007/s10008-012-1850-0.
[120] T. Tooming, T. Thomberg, H. Kurig, A. Jänes, E. Lust, High power density supercapacitors based on the carbon dioxide activated d-glucose derived carbon electrodes and 1-ethyl-3-methylimidazolium tetrafluoroborate ionic liquid, J. Power Sources 280 (2015) 667–677. https://doi.org/10.1016/j.jpowsour.2015.01.157.
[121] M. Pohl, I. Tallo, A. Jänes, T. Romann, E. Lust, Increasing the stability of very high potential electrical double layer capacitors by operando passivation, J. Power Sources 402 (2018) 53–61. https://doi.org/10.1016/j.jpowsour.2018.09.018.
[122] L. Wei, G. Yushin, Electrical double layer capacitors with sucrose derived carbon electrodes in ionic liquid electrolytes, J. Power Sources 196 (2011) 4072–4079. https://doi.org/10.1016/j.jpowsour.2010.12.085.
[123] H. Kurig, M. Vestli, K. Tõnurist, A. Jänes, E. Lust, Influence of room temperature ionic liquid anion chemical composition and electrical charge delocalization on the supercapacitor properties, J. Electrochem. Soc. 159 (2012) A944–A951. https://doi.org/10.1149/2.022207jes.
[124] T. Tooming, T. Thomberg, L. Siinor, K. Tõnurist, A. Jänes, E. Lust, A type high capacitance supercapacitor based on mixed room temperature ionic liquids containing specifically adsorbed iodide anions, J. Electrochem. Soc. 161 (2014) A222–A227. https://doi.org/10.1149/2.014403jes.
[125] E. Tee, I. Tallo, E. Lust, A. Jänes, T. Thomberg, Electrical double layer capacitors based on steam and CO_2-steam co-activated carbon electrodes and ionic

liquid electrolyte, J. Electrochem. Soc. 166 (2019) A1558. https://doi.org/10.1149/2.0811908jes.
[126] D. Weingarth, A. Foelske-Schmitz, R. Kötz, Cycle versus voltage hold – which is the better stability test for electrochemical double layer capacitors?, J. Power Sources 225 (2013) 84–88. https://doi.org/10.1016/j.jpowsour.2012.10.019.
[127] T. Romann, O. Oll, P. Pikma, K. Kirsimäe, E. Lust, 4–10 V capacitors with graphene-based electrodes and ionic liquid electrolyte, J. Power Sources 280 (2015) 606–611. https://doi.org/10.1016/j.jpowsour.2015.01.153.
[128] T. Romann, E. Anderson, P. Pikma, H. Tamme, P. Möller, E. Lust, Reactions at graphene|tetracyanoborate ionic liquid interface – new safety mechanisms for supercapacitors and batteries, Electrochem. Commun. 74 (2017) 38–41. https://doi.org/10.1016/j.elecom.2016.11.016.
[129] M. Gara, R. G. Compton, Activity of carbon electrodes towards oxygen reduction in acid: a comparative study, New J. Chem. 35 (2011) 2647–2652. https://doi.org/10.1039/C1NJ20612E.
[130] D. Weingarth, D. Cericola, F. C. F. Mornaghini, T. Hucke, R. Kötz, Carbon additives for electrical double layer capacitor electrodes, J. Power Sources 266 (2014) 475–480. https://doi.org/10.1016/j.jpowsour.2014.05.065.
[131] M. M. Hantel, R. Nesper, A. Wokaun, R. Kötz, In-situ XRD and dilatometry investigation of the formation of pillared graphene via electrochemical activation of partially reduced graphite oxide, Electrochim. Acta 134 (2014) 459–470. https://doi.org/10.1016/j.electacta.2014.04.063.
[132] M. M. Hantel, D. Weingarth, R. Kötz, Parameters determining dimensional changes of porous carbons during capacitive charging, Carbon 69 (2014) 275–286. https://doi.org/10.1016/j.carbon.2013.12.026.
[133] N. Jäckel, D. Weingarth, A. Schreiber, B. Krüner, M. Zeiger, A. Tolosa, M. Aslan, V. Presser, Performance evaluation of conductive additives for activated carbon supercapacitors in organic electrolyte, Electrochim. Acta 191 (2016) 284–298. https://doi.org/10.1016/j.electacta.2016.01.065.
[134] J. Kruusma, A. Tõnisoo, R. Pärna, E. Nõmmiste, I. Tallo, T. Romann, E. Lust, Influence of the negative potential of molybdenum carbide derived carbon electrode on the in situ synchrotron radiation activated X-ray photoelectron spectra of 1-ethyl-3-methylimidazolium tetrafluoroborate, Electrochim. Acta 206 (2016) 419–426. https://doi.org/10.1016/j.electacta.2015.10.060.
[135] J. Kruusma, A. Tõnisoo, R. Pärna, E. Nõmmiste, I. Kuusik, M. Vahtrus, I. Tallo, T. Romann, E. Lust, The electrochemical behavior of 1-ethyl-3-methyl imidazolium tetracyanoborate visualized by in situ X-ray photoelectron spectroscopy at the negatively and positively polarized micro-mesoporous carbon electrode, J. Electrochem. Soc. 164 (2017) A3393. https://doi.org/10.1149/2.1861713jes.
[136] M. E. Orazem, N. Pébère, B. Tribollet, Enhanced graphical representation of electrochemical impedance data, J. Electrochem. Soc. 153 (2006) B129–B136. https://doi.org/10.1149/1.2168377.
[137] A. Jänes, L. Permann, M. Arulepp, E. Lust, Electrochemical characteristics of nanoporous carbide-derived carbon materials in non-aqueous electrolyte solutions, Electrochem. Commun. 3 (2004) 313–318. https://doi.org/10.1016/j.elecom.2004.01.009.
[138] R. Väli, A. Jänes, T. Thomberg, E. Lust, Synthesis and characterization of d-glucose derived nanospheric hard carbon negative electrodes for lithium- and

sodium-ion batteries, Electrochim. Acta 253 (2017) 536–544. https://doi.org/10.1016/j.electacta.2017.09.094.
[139] J. K. Foley, C. Korzeniewski, S. Pons, Anodic and cathodic reactions in acetonitrile/tetra-n-butylammonium tetrafluoroborate: an electrochemical and infrared spectroelectrochemical study, Can. J. Chem. 66 (1988) 201–206. https://doi.org/10.1139/v88-033.
[140] T. Romann, O. Oll, P. Pikma, H. Tamme, E. Lust, Surface chemistry of carbon electrodes in 1-ethyl-3-methylimidazolium tetrafluoroborate ionic liquid - an in situ infrared study, Electrochim. Acta 125 (2014) 183–190. https://doi.org/10.1016/j.electacta.2014.01.077.
[141] A. Tõnisoo, J. Kruusma, R. Pärna, A. Kikas, M. Hirsimäki, E. Nõmmiste, E. Lust, In situ XPS studies of electrochemically negatively polarized molybdenum carbide derived carbon double layer capacitor electrode, J. Electrochem. Soc. 160 (2013) A1084–A1093. https://doi.org/10.1149/2.042308jes.
[142] J. Kruusma, A. Tõnisoo, R. Pärna, E. Nõmmiste, M. Vahtrus, L. Siinor, I. Tallo, T. Romann, E. Lust, Influence of iodide ions concentration on the stability of 1-Ethyl-3-methylimidazolium tetrafluoroborate | molybdenum carbide derived carbon electrode interface, J. Electrochem. Soc. 164 (2017) A1110. https://doi.org/10.1149/2.0641706jes.
[143] R. Palm, H. Kurig, K. Tõnurist, A. Jänes, E. Lust, Electrical double layer capacitors based on 1-ethyl-3-methylimidazolium tetrafluoroborate with small addition of acetonitrile, Electrochim. Acta. 85 (2012) 139–144. https://doi.org/10.1016/j.electacta.2012.08.030.

SUMMARY IN ESTONIAN

Uudsete süsinikmaterjalide süntees ja karakteriseerimine suure võimusega superkondensaatorite rakendusteks

Titaankarbiidi (TiC) ja titaankarbiidi/süsiniknanotorude (TiC/CNT) komposiitide sünteesimiseks kasutati sool-geel meetodit ning vastava karbiidset päritolu süsinikmaterjali (CDC) elektrokeemiliste omaduste varieerimiseks ja uurimiseks valmistati kahe erineva CNT osakaaluga komposiiti (1% ja 2% massiprotsenti). Sünteesitud süsinikmaterjale kasutati elektroodide valmistamiseks väga suure võimsusega superkondensaatorite testrakkudes.

Nii algne TiC kui ka vastav CDC materjal omavad mikro- ja mesopoorsust. Karbiidide eripinnad jäävad vahemikku 152 and 274 $m^2 g^{-1}$ ning sool-geel meetodiga sünteesitud karbiidid ja nendele vastavate CDC eripinnad ulatuvad väärtuseni kuni 1710 $m^2 g^{-1}$, mis on kõrgem kui tavaliselt saavutatud kommertsiaalsest TiC sünteesitud süsinikmaterjalil (TiC-CDC) (1350 – 1500 $m^2 g^{-1}$). Sool-geel meetodiga sünteesitud titaankarbiidil põhinev süsinik omab suuremat mesopoorsust võrreldes kommertsiaalse TiC-CDC-ga.

Süsiniknanotorude lisamine vähendab üleüldist süsinikmaterjali eripinda, kuid ei mõjuta selle poorijaotust, mis jääb enamvähem samaks. Süsinikmaterjali mesopoorsuse ja eripinna suurenemine võib olla ühelt poolt tingitud titaankarbiidi mittestöhhiomeetrilisest struktuurist, aga võib olla põhjustatud ka oksükarbiidi olemasolust esialgses karbiidipulbris. Oksükarbiidis olev hapnik reageerib saadud süsinikuga (andes CO_2 või CO), mille tulemusena tekib poorsem hierarhilise struktuuriga süsinikmaterjal.

Elektrokeemiliste karakteristikute uurimiseks pandi kokku mitu erinevat elektrilise kaksikihi kondensaatori (EDLC) testrakku, mis koosnesid sünteesitud süsinikmaterjalidest, separaatorist ja elektrolüüdist. Elektrolüütidena kasutati nii ioonset vedelikku 1-etüül-3-metüülimidasooliumtetrafluoroboraati ($EtMeImBF_4$) kui ka 1 M trietüülmetüülammooniumtetrafluoroboraadi (Et_3MeNBF_4) lahust atsetonitriilis (AN). Kokkupandud testrakke testiti tsüklilise voltamperomeetria (CV), konstantse vooluga täis- ja tühjakslaadimise (CCCD), elektrokeemilise impedantsspektroskoopia (EIS) ja konstantse võimsuse (CP) meetodite abil.

Tsüklilise voltamperomeetria meetodi korral näitasid kõik uuritavad süsinikmaterjalidel põhinevad EDLC-d ligilähedaselt ideaalset mahtuvuslikku käitumist rakupotentsiaalini (ΔE) kuni 3.6 V ja potentsiaali laotuskiiruseni 500 mV s^{-1}. Isegi väga suuretel laotuskiirustel ($v \leq 500$ mV s^{-1}) puudub CDC maatriksis märkimisväärne potentsiaalilangus, mis tuleneb arvatavasti süsiniku maatriksis esinevast suuremast mesopoorsusest.

Suurimad järjestikmahtuvuse väärtused (C_s) 176 F g^{-1} (ΔE = 3.6 V, elektrolüüdiks $EtMeImBF_4$) ja 145 F g^{-1} (ΔE = 3.0 V, elektrolüüdiks 1 M Et_3MeNBF_4 + AN) saadi ilma nanotorude lisandita materjali korral. Kõikide testitud materjalide puhul näitasid kokku pandud EDLC testrakud ideaalset mahtuvuslikku käitumist, saavutades faasinurgad ligikaudu −85°.

Arvutatud energia efektiivsused jäid kõikide materjalide ja mõlema elektrolüüdi puhul 93–97 % vahele (laadimise voolutihedusel 1 A g^{-1}) ning elektrilised efektiivsused ületasid 99%.

Uuritavatel süsinikmaterjalidel põhinevad EDLC-d omavad ülihead võimsustihedust P > 100 kW kg^{-1} energiatiheduse E = 30 Wh kg^{-1} korral (elektrolüüdiks 1 M Et_3MeNBF_4 + AN). Ioonsel vedelikul $EtMeImBF_4$ põhineva EDLC omab samal võimsustihedusel (100 kW kg^{-1}) natukene väiksemat, aga siiski väga kõrget energiatihedust 10 Wh kg^{-1}. Seega lisaks elektroodimaterjali mesopoorsuse optimeerimisele tuleb vähendada ka elektrolüüdi viskoosust ning tõsta selle juhtivust, et saavutatada energiasalvestusseadmetel ülisuur võimsustihedus väga suurtel energiatihedustel.

Samuti näidati, et TiC-CDC elektroodidel põhinevat EDLC-d on võimalik stabiliseerida rakupotentsiaalidel üle 3.4 V, kasutades elektrolüüdina 1 M Et_3MeNBF_4 + AN kui rakendada süsteemile hoolikalt elektrokeemilist eeltöötlemist (potentsiaalitsükli piirkonna samm-sammult laiendamise ja korduva CV polariseerimisega kuni 3.7 V). Passiveerimise/stabiliseerimise efekt on selgitatav amorfsemate ja aktiivsemate kohtade (reaktsioonitsentrite) oksüdeerumise/redutseerimisega, mis tähendab, et toimub aktiivsemate funktsionaalsete rühmade elektrokeemiline lahustumine TiC-CDC pinnalt. Selle tulemusena toimub pinna rikastamine rohkema süsinikuga ja stabiilsemate grafiitsete sp^2 süsiniku piirkondadega. Samas võib passiveerimine toimuda ka õhukeste passiivsete polümeersete kilede moodustamise teel.

Stabiliseerimis-/passiveerimisnähtuse täpset mehhanismi ei saa käesolevas doktoritöös kindlaks teha, kuid seda uuritakse kindlasti üksikasjalikumalt edasi pikaajaliste katsete käigus, kasutades tulemuste analüüsimiseks in situ FTIR-i, sekundaarset ioonmassispektromeetriat ja sünkrotronkiirgusel põhinevaid XPS meetodeid. Nii suure rakupotentsiaaliga EDLC-del ei pruugi olla sama kauakestvat stabiilsust kui praegustel kommertsiaalsetel superkondensaatoritel (rakupotentsiaal alla 3.0 V), kuid energia- ja võimsustiheduse poolest ületavad need märkimisväärselt vastavate EDLC väärtuseid. Neid EDLC-sid saaks kasutada rakendustes, kus soovitakse saavutada ülisuuri võimsustihedusi.

ACKNOWLEDGMENTS

I would like to thank my supervisors. The greatest gratitude to Prof. Enn Lust for always being there; PhD Thomas Thomberg for helping me anytime I asked him and PhD Indrek Tallo for being there from the start of my master's program. I would also like to thank all the Chemicum fifth floor family – for all the interesting conversations and just sometimes having fun.

Special thanks to all the people who helped me with different measurements that I needed for my research: Riinu Härmas, Rasmus Palm and Heisi Kurig for sorption measurements, Jaan Aruväli for XRD and XRF measurements and Tavo Romann for infrared and Raman measurements.

I would like to acknowledge my family and friends – especially my husband who has always driven me to be my best.

This research was supported by the EU through the European Regional Development Fund (projects 2014-2020.4.01.15-0011, 3.2.0101–0030, 3.2.0302.10-0169 and 2014-2020.4.01.16-0131), Institutional Research grant IUT20-13, personal research grant PUT1033, PUT55 and Estonian Research Council's program RITA supported by ERDF.

PUBLICATIONS

CURRICULUM VITAE

Name: Maarja Paalo (née Pohl)
Date of birth: August 30th, 1990
Citizenship: Estonian
Address: Institute of Chemistry, University of Tartu
Ravila 14a, 50411 Tartu, Estonia
Telephone: +372 737 5184
E-mail: maarja.paalo@ut.ee

Education:

2016– … University of Tartu, Institute of Chemistry, PhD student
2014–2016 University of Tartu – Master's degree in material science
2010–2014 University of Tartu – Bachelor's degree in material science
1997–2009 Pirita Economy High School

Professional career:

2014–… University of Tartu, Institute of Chemistry, Chemist
2012–2014 University of Tartu, Institute of Physics, Laboratory Assistant

Awards:

2017 Estonian National Contest for University Students, 3rd prize, master's degree

List of publications:

1. M. Koppel, R. Palm, R. Härmas, M. Russina, N. Matsubara, M. Mansson, V. Grzimek, **M. Paalo**, J. Aruväli, T. Romann, O. Oll, E. Lust, In situ observation of pressure modulated reversible structural changes in the graphitic domains of carbide-derived carbons, Carbon 174 (2021) 190-200.
2. L. Naheed, M. Koppel, **M. Paalo**, K. Alsabawi, K. E. Lamb, E. MacA. Gray, A. Jänes, C. J. Webb, Hydrogen adsorption properties of carbide-derived carbons at ambient temperature and high pressure, International Journal of Hydrogen Energy 46 (2021) 15761−15772.
3. R. Jäger, P. Teppor, **M. Paalo**, M. Härmas, A. Adamson, O. Volobujeva, E. Härk, Z. Kochovski, T. Romann, R. Härmas, J. Aruväli, A. Kikas, E. Lust, Synthesis and characterization of cobalt and nitrogen co-doped peat-derived carbon catalysts for oxygen reduction in acidic media, Catalysts 11 (2021) ARTN 715.
4. M. Härmas, R. Palm, T. Thomberg, R. Härmas, M. Koppel, **M. Paalo**, I. Tallo, T. Romann, A. Jänes, E. Lust, Hydrothermal and peat-derived carbons as electrode materials for high-efficient electrical double-layer capacitors, Journal of Applied Electrochemistry 50 (2020) 15−32.
5. R. Jäger, P. Teppor, E. Härk, M. Härmas, A. Adamson, **M. Paalo**, O. Volobujeva, A. Kikas, T. Romann, R. Härmas, E. Lust, Cobalt and nitrogen co-

doped peat derived carbon based catalysts for oxygen reduction, ECS Transactions 97 (7) (2020) 605−613.

6. **M. Paalo**, I. Tallo, T. Thomberg, A. Jänes, E. Lust, Enhanced power performance of highly mesoporous sol-gel TiC derived carbons in ionic liquid and non-aqueous electrolyte based capacitors, Journal of The Electrochemical Society 166 (13) (2019) A2887-A2895.
7. R. Härmas, R. Palm, M. Russina, H. Kurig, V. Grzimek, E. Härk, M. Koppel, I. Tallo, **M. Paalo**, O. Oll, J. Embs, E. Lust, Transport properties of H_2 confined in carbide-derived carbons with different pore shapes and sizes, Carbon 155 (2019) 122−128.
8. R. Härmas, R. Palm, M. Härmas, **M. Pohl**, H. Kurig, I. Tallo, E. Tee, I. Vaas, R. Väli, T. Romann, O. Oll, R. Kanarbik, K. Liivand, J. Eskusson, J. Kruusma, T. Thomberg, A. Jänes, P. Miidla, E. Lust, Influence of porosity parameters and electrolyte chemical composition on the power densities of non-aqueous and ionic liquid based supercapacitors. Electrochimica Acta 283 (2018) 931−948.
9. **M. Pohl**, I. Tallo, A. Jänes, T. Romann, E. Lust, Increasing the stability of very high potential electrical double layer capacitors by operando passivation, Journal of Power Sources 402 (2018) 53–61.
10. **M. Pohl**, H. Kurig, I. Tallo, A. Jänes, E. Lust, Novel sol-gel synthesis route of carbide-derived carbon composites for very high power density supercapacitors, Chemical Engineering Journal 320 (2017) 576–587.

Participation in international conferences:

1. M. Pohl, H. Kurig, I. Tallo, A. Jänes, E. Lust, Novel sol-gel synthesis route of carbide-derived carbon for very high power density supercapacitors, 69th Annual Meeting of the International Society of Electrochemistry, Bologna, Italy, 2–7. August 2018 (poster presentation).
2. M. Paalo, H. Kurig, I. Tallo, A. Jänes, E. Lust, Combined sol-gel and carbothermal reduction synthesis route of carbide-derived carbon for very high power density supercapacitors, 7th Baltic Electrochemistry Conference, Tartu, Estonia, 4–7. November 2018 (poster presentation).

ELULOOKIRJELDUS

Nimi: Maarja Paalo (neiupõlvenimi Pohl)
Sünniaeg: 30. august 1990
Kodakondsus: Eesti
Aadress: Keemia instituut, Tartu Ülikool
Ravila 14a, Tartu, 50411, Eesti
Telefon: +372 737 5184
E-mail: maarja.paalo@ut.ee

Hariduskäik:

2016– … Tartu Ülikooli keemia instituut, doktorant
2014–2016 Tartu Ülikool – magistrikraad materjaliteaduses
2010–2014 Tartu Ülikool – bakalaureusekraad materjaliteaduses
1997–2009 Pirita Majandusgümnaasium

Teenistuskäik:

2014–… Tartu Ülikooli keemia instituut, keemik
2012–2014 Tartu Ülikooli füüsika instituut, laborant

Teaduspreemiad:

2017 Üliõpilaste teadustööde riiklik konkurss, III preemia, magistriõpe

Publikatsioonid:

1. M. Koppel, R. Palm, R. Härmas, M. Russina, N. Matsubara, M. Mansson, V. Grzimek, **M. Paalo**, J. Aruväli, T. Romann, O. Oll, E. Lust, In situ observation of pressure modulated reversible structural changes in the graphitic domains of carbide-derived carbons, Carbon 174 (2021) 190-200.
2. L. Naheed, M. Koppel, **M. Paalo**, K. Alsabawi, K. E. Lamb, E. MacA. Gray, A. Jänes, C. J. Webb, Hydrogen adsorption properties of carbide-derived carbons at ambient temperature and high pressure, International Journal of Hydrogen Energy 46 (2021) 15761−15772.
3. R. Jäger, P. Teppor, **M. Paalo**, M. Härmas, A. Adamson, O. Volobujeva, E. Härk, Z. Kochovski, T. Romann, R. Härmas, J. Aruväli, A. Kikas, E. Lust, Synthesis and characterization of cobalt and nitrogen co-doped peat-derived carbon catalysts for oxygen reduction in acidic media, Catalysts 11 (2021) ARTN 715.
4. M. Härmas, R. Palm, T. Thomberg, R. Härmas, M. Koppel, **M. Paalo**, I. Tallo, T. Romann, A. Jänes, E. Lust, Hydrothermal and peat-derived carbons as electrode materials for high-efficient electrical double-layer capacitors, Journal of Applied Electrochemistry 50 (2020) 15−32.
5. R. Jäger, P. Teppor, E. Härk, M. Härmas, A. Adamson, **M. Paalo**, O. Volobujeva, A. Kikas, T. Romann, R. Härmas, E. Lust, Cobalt and nitrogen co-

doped peat derived carbon based catalysts for oxygen reduction, ECS Transactions 97 (7) (2020) 605−613.

6. **M. Paalo**, I. Tallo, T. Thomberg, A. Jänes, E. Lust, Enhanced power performance of highly mesoporous sol-gel TiC derived carbons in ionic liquid and non-aqueous electrolyte based capacitors, Journal of The Electrochemical Society 166 (13) (2019) A2887-A2895.
7. R. Härmas, R. Palm, M. Russina, H. Kurig, V. Grzimek, E. Härk, M. Koppel, I. Tallo, **M. Paalo**, O. Oll, J. Embs, E. Lust, Transport properties of H_2 confined in carbide-derived carbons with different pore shapes and sizes, Carbon 155 (2019) 122−128.
8. R. Härmas, R. Palm, M. Härmas, **M. Pohl**, H. Kurig, I. Tallo, E. Tee, I. Vaas, R. Väli, T. Romann, O. Oll, R. Kanarbik, K. Liivand, J. Eskusson, J. Kruusma, T. Thomberg, A. Jänes, P. Miidla, E. Lust, Influence of porosity parameters and electrolyte chemical composition on the power densities of non-aqueous and ionic liquid based supercapacitors. Electrochimica Acta 283 (2018) 931−948.
9. **M. Pohl**, I. Tallo, A. Jänes, T. Romann, E. Lust, Increasing the stability of very high potential electrical double layer capacitors by operando passivation, Journal of Power Sources 402 (2018) 53–61.
10. **M. Pohl**, H. Kurig, I. Tallo, A. Jänes, E. Lust, Novel sol-gel synthesis route of carbide-derived carbon composites for very high power density supercapacitors, Chemical Engineering Journal 320 (2017) 576–587.

Rahvusvahelistel konverentsidel osalemine:

1. M. Pohl, H. Kurig, I. Tallo, A. Jänes, E. Lust, Novel sol-gel synthesis route of carbide-derived carbon for very high power density supercapacitors, 69th Annual Meeting of the International Society of Electrochemistry, Bologna, Italy, 2–7. August 2018 (poster presentation).
2. M. Paalo, H. Kurig, I. Tallo, A. Jänes, E. Lust, Combined sol-gel and carbothermal reduction synthesis route of carbide-derived carbon for very high power density supercapacitors, 7th Baltic Electrochemistry Conference, Tartu, Estonia, 4–7. November 2018 (poster presentation).

DISSERTATIONES CHIMICAE UNIVERSITATIS TARTUENSIS

1. **Toomas Tamm.** Quantum-chemical simulation of solvent effects. Tartu, 1993, 110 p.
2. **Peeter Burk.** Theoretical study of gas-phase acid-base equilibria. Tartu, 1994, 96 p.
3. **Victor Lobanov.** Quantitative structure-property relationships in large descriptor spaces. Tartu, 1995, 135 p.
4. **Vahur Mäemets.** The ^{17}O and ^{1}H nuclear magnetic resonance study of H_2O in individual solvents and its charged clusters in aqueous solutions of electrolytes. Tartu, 1997, 140 p.
5. **Andrus Metsala.** Microcanonical rate constant in nonequilibrium distribution of vibrational energy and in restricted intramolecular vibrational energy redistribution on the basis of slater's theory of unimolecular reactions. Tartu, 1997, 150 p.
6. **Uko Maran.** Quantum-mechanical study of potential energy surfaces in different environments. Tartu, 1997, 137 p.
7. **Alar Jänes.** Adsorption of organic compounds on antimony, bismuth and cadmium electrodes. Tartu, 1998, 219 p.
8. **Kaido Tammeveski.** Oxygen electroreduction on thin platinum films and the electrochemical detection of superoxide anion. Tartu, 1998, 139 p.
9. **Ivo Leito.** Studies of Brønsted acid-base equilibria in water and non-aqueous media. Tartu, 1998, 101 p.
10. **Jaan Leis.** Conformational dynamics and equilibria in amides. Tartu, 1998, 131 p.
11. **Toonika Rinken.** The modelling of amperometric biosensors based on oxidoreductases. Tartu, 2000, 108 p.
12. **Dmitri Panov.** Partially solvated Grignard reagents. Tartu, 2000, 64 p.
13. **Kaja Orupõld.** Treatment and analysis of phenolic wastewater with microorganisms. Tartu, 2000, 123 p.
14. **Jüri Ivask.** Ion Chromatographic determination of major anions and cations in polar ice core. Tartu, 2000, 85 p.
15. **Lauri Vares.** Stereoselective Synthesis of Tetrahydrofuran and Tetrahydropyran Derivatives by Use of Asymmetric Horner-Wadsworth-Emmons and Ring Closure Reactions. Tartu, 2000, 184 p.
16. **Martin Lepiku.** Kinetic aspects of dopamine D_2 receptor interactions with specific ligands. Tartu, 2000, 81 p.
17. **Katrin Sak.** Some aspects of ligand specificity of P2Y receptors. Tartu, 2000, 106 p.
18. **Vello Pällin.** The role of solvation in the formation of iotsitch complexes. Tartu, 2001, 95 p.
19. **Katrin Kollist.** Interactions between polycyclic aromatic compounds and humic substances. Tartu, 2001, 93 p.

20. **Ivar Koppel.** Quantum chemical study of acidity of strong and superstrong Brønsted acids. Tartu, 2001, 104 p.
21. **Viljar Pihl.** The study of the substituent and solvent effects on the acidity of OH and CH acids. Tartu, 2001, 132 p.
22. **Natalia Palm.** Specification of the minimum, sufficient and significant set of descriptors for general description of solvent effects. Tartu, 2001, 134 p.
23. **Sulev Sild.** QSPR/QSAR approaches for complex molecular systems. Tartu, 2001, 134 p.
24. **Ruslan Petrukhin.** Industrial applications of the quantitative structure-property relationships. Tartu, 2001, 162 p.
25. **Boris V. Rogovoy.** Synthesis of (benzotriazolyl)carboximidamides and their application in relations with *N*- and *S*-nucleophyles. Tartu, 2002, 84 p.
26. **Koit Herodes.** Solvent effects on UV-vis absorption spectra of some solvatochromic substances in binary solvent mixtures: the preferential solvation model. Tartu, 2002, 102 p.
27. **Anti Perkson.** Synthesis and characterisation of nanostructured carbon. Tartu, 2002, 152 p.
28. **Ivari Kaljurand.** Self-consistent acidity scales of neutral and cationic Brønsted acids in acetonitrile and tetrahydrofuran. Tartu, 2003, 108 p.
29. **Karmen Lust.** Adsorption of anions on bismuth single crystal electrodes. Tartu, 2003, 128 p.
30. **Mare Piirsalu.** Substituent, temperature and solvent effects on the alkaline hydrolysis of substituted phenyl and alkyl esters of benzoic acid. Tartu, 2003, 156 p.
31. **Meeri Sassian.** Reactions of partially solvated Grignard reagents. Tartu, 2003, 78 p.
32. **Tarmo Tamm.** Quantum chemical modelling of polypyrrole. Tartu, 2003. 100 p.
33. **Erik Teinemaa.** The environmental fate of the particulate matter and organic pollutants from an oil shale power plant. Tartu, 2003. 102 p.
34. **Jaana Tammiku-Taul.** Quantum chemical study of the properties of Grignard reagents. Tartu, 2003. 120 p.
35. **Andre Lomaka.** Biomedical applications of predictive computational chemistry. Tartu, 2003. 132 p.
36. **Kostyantyn Kirichenko.** Benzotriazole – Mediated Carbon–Carbon Bond Formation. Tartu, 2003. 132 p.
37. **Gunnar Nurk.** Adsorption kinetics of some organic compounds on bismuth single crystal electrodes. Tartu, 2003, 170 p.
38. **Mati Arulepp.** Electrochemical characteristics of porous carbon materials and electrical double layer capacitors. Tartu, 2003, 196 p.
39. **Dan Cornel Fara.** QSPR modeling of complexation and distribution of organic compounds. Tartu, 2004, 126 p.
40. **Riina Mahlapuu.** Signalling of galanin and amyloid precursor protein through adenylate cyclase. Tartu, 2004, 124 p.

41. **Mihkel Kerikmäe.** Some luminescent materials for dosimetric applications and physical research. Tartu, 2004, 143 p.
42. **Jaanus Kruusma.** Determination of some important trace metal ions in human blood. Tartu, 2004, 115 p.
43. **Urmas Johanson.** Investigations of the electrochemical properties of polypyrrole modified electrodes. Tartu, 2004, 91 p.
44. **Kaido Sillar.** Computational study of the acid sites in zeolite ZSM-5. Tartu, 2004, 80 p.
45. **Aldo Oras.** Kinetic aspects of dATPαS interaction with $P2Y_1$ receptor. Tartu, 2004, 75 p.
46. **Erik Mölder.** Measurement of the oxygen mass transfer through the air-water interface. Tartu, 2005, 73 p.
47. **Thomas Thomberg.** The kinetics of electroreduction of peroxodisulfate anion on cadmium (0001) single crystal electrode. Tartu, 2005, 95 p.
48. **Olavi Loog.** Aspects of condensations of carbonyl compounds and their imine analogues. Tartu, 2005, 83 p.
49. **Siim Salmar.** Effect of ultrasound on ester hydrolysis in aqueous ethanol. Tartu, 2006, 73 p.
50. **Ain Uustare.** Modulation of signal transduction of heptahelical receptors by other receptors and G proteins. Tartu, 2006, 121 p.
51. **Sergei Yurchenko.** Determination of some carcinogenic contaminants in food. Tartu, 2006, 143 p.
52. **Kaido Tämm.** QSPR modeling of some properties of organic compounds. Tartu, 2006, 67 p.
53. **Olga Tšubrik.** New methods in the synthesis of multisubstituted hydrazines. Tartu. 2006, 183 p.
54. **Lilli Sooväli.** Spectrophotometric measurements and their uncertainty in chemical analysis and dissociation constant measurements. Tartu, 2006, 125 p.
55. **Eve Koort.** Uncertainty estimation of potentiometrically measured ph and pK_a values. Tartu, 2006, 139 p.
56. **Sergei Kopanchuk.** Regulation of ligand binding to melanocortin receptor subtypes. Tartu, 2006, 119 p.
57. **Silvar Kallip.** Surface structure of some bismuth and antimony single crystal electrodes. Tartu, 2006, 107 p.
58. **Kristjan Saal.** Surface silanization and its application in biomolecule coupling. Tartu, 2006, 77 p.
59. **Tanel Tätte.** High viscosity $Sn(OBu)_4$ oligomeric concentrates and their applications in technology. Tartu, 2006, 91 p.
60. **Dimitar Atanasov Dobchev**. Robust QSAR methods for the prediction of properties from molecular structure. Tartu, 2006, 118 p.
61. **Hannes Hagu**. Impact of ultrasound on hydrophobic interactions in solutions. Tartu, 2007, 81 p.
62. **Rutha Jäger.** Electroreduction of peroxodisulfate anion on bismuth electrodes. Tartu, 2007, 142 p.

63. **Kaido Viht.** Immobilizable bisubstrate-analogue inhibitors of basophilic protein kinases: development and application in biosensors. Tartu, 2007, 88 p.
64. **Eva-Ingrid Rõõm.** Acid-base equilibria in nonpolar media. Tartu, 2007, 156 p.
65. **Sven Tamp.** DFT study of the cesium cation containing complexes relevant to the cesium cation binding by the humic acids. Tartu, 2007, 102 p.
66. **Jaak Nerut.** Electroreduction of hexacyanoferrate(III) anion on Cadmium (0001) single crystal electrode. Tartu, 2007, 180 p.
67. **Lauri Jalukse.** Measurement uncertainty estimation in amperometric dissolved oxygen concentration measurement. Tartu, 2007, 112 p.
68. **Aime Lust.** Charge state of dopants and ordered clusters formation in CaF_2:Mn and CaF_2:Eu luminophors. Tartu, 2007, 100 p.
69. **Iiris Kahn**. Quantitative Structure-Activity Relationships of environmentally relevant properties. Tartu, 2007, 98 p.
70. **Mari Reinik.** Nitrates, nitrites, N-nitrosamines and polycyclic aromatic hydrocarbons in food: analytical methods, occurrence and dietary intake. Tartu, 2007, 172 p.
71. **Heili Kasuk.** Thermodynamic parameters and adsorption kinetics of organic compounds forming the compact adsorption layer at Bi single crystal electrodes. Tartu, 2007, 212 p.
72. **Erki Enkvist.** Synthesis of adenosine-peptide conjugates for biological applications. Tartu, 2007, 114 p.
73. **Svetoslav Hristov Slavov**. Biomedical applications of the QSAR approach. Tartu, 2007, 146 p.
74. **Eneli Härk.** Electroreduction of complex cations on electrochemically polished Bi(*hkl*) single crystal electrodes. Tartu, 2008, 158 p.
75. **Priit Möller.** Electrochemical characteristics of some cathodes for medium temperature solid oxide fuel cells, synthesized by solid state reaction technique. Tartu, 2008, 90 p.
76. **Signe Viggor.** Impact of biochemical parameters of genetically different pseudomonads at the degradation of phenolic compounds. Tartu, 2008, 122 p.
77. **Ave Sarapuu.** Electrochemical reduction of oxygen on quinone-modified carbon electrodes and on thin films of platinum and gold. Tartu, 2008, 134 p.
78. **Agnes Kütt.** Studies of acid-base equilibria in non-aqueous media. Tartu, 2008, 198 p.
79. **Rouvim Kadis.** Evaluation of measurement uncertainty in analytical chemistry: related concepts and some points of misinterpretation. Tartu, 2008, 118 p.
80. **Valter Reedo.** Elaboration of IVB group metal oxide structures and their possible applications. Tartu, 2008, 98 p.
81. **Aleksei Kuznetsov.** Allosteric effects in reactions catalyzed by the cAMP-dependent protein kinase catalytic subunit. Tartu, 2009, 133 p.

82. **Aleksei Bredihhin.** Use of mono- and polyanions in the synthesis of multisubstituted hydrazine derivatives. Tartu, 2009, 105 p.
83. **Anu Ploom.** Quantitative structure-reactivity analysis in organosilicon chemistry. Tartu, 2009, 99 p.
84. **Argo Vonk.** Determination of adenosine A_{2A}- and dopamine D_1 receptor-specific modulation of adenylate cyclase activity in rat striatum. Tartu, 2009, 129 p.
85. **Indrek Kivi.** Synthesis and electrochemical characterization of porous cathode materials for intermediate temperature solid oxide fuel cells. Tartu, 2009, 177 p.
86. **Jaanus Eskusson.** Synthesis and characterisation of diamond-like carbon thin films prepared by pulsed laser deposition method. Tartu, 2009, 117 p.
87. **Marko Lätt.** Carbide derived microporous carbon and electrical double layer capacitors. Tartu, 2009, 107 p.
88. **Vladimir Stepanov.** Slow conformational changes in dopamine transporter interaction with its ligands. Tartu, 2009, 103 p.
89. **Aleksander Trummal.** Computational Study of Structural and Solvent Effects on Acidities of Some Brønsted Acids. Tartu, 2009, 103 p.
90. **Eerold Vellemäe.** Applications of mischmetal in organic synthesis. Tartu, 2009, 93 p.
91. **Sven Parkel.** Ligand binding to $5\text{-}HT_{1A}$ receptors and its regulation by Mg^{2+} and Mn^{2+}. Tartu, 2010, 99 p.
92. **Signe Vahur.** Expanding the possibilities of ATR-FT-IR spectroscopy in determination of inorganic pigments. Tartu, 2010, 184 p.
93. **Tavo Romann**. Preparation and surface modification of bismuth thin film, porous, and microelectrodes. Tartu, 2010, 155 p.
94. **Nadežda Aleksejeva.** Electrocatalytic reduction of oxygen on carbon nanotube-based nanocomposite materials. Tartu, 2010, 147 p.
95. **Marko Kullapere.** Electrochemical properties of glassy carbon, nickel and gold electrodes modified with aryl groups. Tartu, 2010, 233 p.
96. **Liis Siinor.** Adsorption kinetics of ions at Bi single crystal planes from aqueous electrolyte solutions and room-temperature ionic liquids. Tartu, 2010, 101 p.
97. **Angela Vaasa.** Development of fluorescence-based kinetic and binding assays for characterization of protein kinases and their inhibitors. Tartu 2010, 101 p.
98. **Indrek Tulp.** Multivariate analysis of chemical and biological properties. Tartu 2010, 105 p.
99. **Aare Selberg.** Evaluation of environmental quality in Northern Estonia by the analysis of leachate. Tartu 2010, 117 p.
100. **Darja Lavõgina.** Development of protein kinase inhibitors based on adenosine analogue-oligoarginine conjugates. Tartu 2010, 248 p.
101. **Laura Herm.** Biochemistry of dopamine D_2 receptors and its association with motivated behaviour. Tartu 2010, 156 p.

102. **Terje Raudsepp.** Influence of dopant anions on the electrochemical properties of polypyrrole films. Tartu 2010, 112 p.
103. **Margus Marandi.** Electroformation of Polypyrrole Films: *In-situ* AFM and STM Study. Tartu 2011, 116 p.
104. **Kairi Kivirand.** Diamine oxidase-based biosensors: construction and working principles. Tartu, 2011, 140 p.
105. **Anneli Kruve.** Matrix effects in liquid-chromatography electrospray mass-spectrometry. Tartu, 2011, 156 p.
106. **Gary Urb.** Assessment of environmental impact of oil shale fly ash from PF and CFB combustion. Tartu, 2011, 108 p.
107. **Nikita Oskolkov.** A novel strategy for peptide-mediated cellular delivery and induction of endosomal escape. Tartu, 2011, 106 p.
108. **Dana Martin.** The QSPR/QSAR approach for the prediction of properties of fullerene derivatives. Tartu, 2011, 98 p.
109. **Säde Viirlaid.** Novel glutathione analogues and their antioxidant activity. Tartu, 2011, 106 p.
110. **Ülis Sõukand.** Simultaneous adsorption of Cd^{2+}, Ni^{2+}, and Pb^{2+} on peat. Tartu, 2011, 124 p.
111. **Lauri Lipping.** The acidity of strong and superstrong Brønsted acids, an outreach for the "limits of growth": a quantum chemical study. Tartu, 2011, 124 p.
112. **Heisi Kurig.** Electrical double-layer capacitors based on ionic liquids as electrolytes. Tartu, 2011, 146 p.
113. **Marje Kasari.** Bisubstrate luminescent probes, optical sensors and affinity adsorbents for measurement of active protein kinases in biological samples. Tartu, 2012, 126 p.
114. **Kalev Takkis.** Virtual screening of chemical databases for bioactive molecules. Tartu, 2012, 122 p.
115. **Ksenija Kisseljova**. Synthesis of aza-β^3-amino acid containing peptides and kinetic study of their phosphorylation by protein kinase A. Tartu, 2012, 104 p.
116. **Riin Rebane.** Advanced method development strategy for derivatization LC/ESI/MS. Tartu, 2012, 184 p.
117. **Vladislav Ivaništšev.** Double layer structure and adsorption kinetics of ions at metal electrodes in room temperature ionic liquids. Tartu, 2012, 128 p.
118. **Irja Helm.** High accuracy gravimetric Winkler method for determination of dissolved oxygen. Tartu, 2012, 139 p.
119. **Karin Kipper.** Fluoroalcohols as Components of LC-ESI-MS Eluents: Usage and Applications. Tartu, 2012, 164 p.
120. **Arno Ratas.** Energy storage and transfer in dosimetric luminescent materials. Tartu, 2012, 163 p.
121. **Reet Reinart-Okugbeni**. Assay systems for characterisation of subtype-selective binding and functional activity of ligands on dopamine receptors. Tartu, 2012, 159 p.

122. **Lauri Sikk.** Computational study of the Sonogashira cross-coupling reaction. Tartu, 2012, 81 p.
123. **Karita Raudkivi.** Neurochemical studies on inter-individual differences in affect-related behaviour of the laboratory rat. Tartu, 2012, 161 p.
124. **Indrek Saar.** Design of GalR2 subtype specific ligands: their role in depression-like behavior and feeding regulation. Tartu, 2013, 126 p.
125. **Ann Laheäär.** Electrochemical characterization of alkali metal salt based non-aqueous electrolytes for supercapacitors. Tartu, 2013, 127 p.
126. **Kerli Tõnurist.** Influence of electrospun separator materials properties on electrochemical performance of electrical double-layer capacitors. Tartu, 2013, 147 p.
127. **Kaija Põhako-Esko.** Novel organic and inorganic ionogels: preparation and characterization. Tartu, 2013, 124 p.
128. **Ivar Kruusenberg.** Electroreduction of oxygen on carbon nanomaterial-based catalysts. Tartu, 2013, 191 p.
129. **Sander Piiskop.** Kinetic effects of ultrasound in aqueous acetonitrile solutions. Tartu, 2013, 95 p.
130. **Ilona Faustova**. Regulatory role of L-type pyruvate kinase N-terminal domain. Tartu, 2013, 109 p.
131. **Kadi Tamm.** Synthesis and characterization of the micro-mesoporous anode materials and testing of the medium temperature solid oxide fuel cell single cells. Tartu, 2013, 138 p.
132. **Iva Bozhidarova Stoyanova-Slavova.** Validation of QSAR/QSPR for regulatory purposes. Tartu, 2013, 109 p.
133. **Vitali Grozovski**. Adsorption of organic molecules at single crystal electrodes studied by *in situ* STM method. Tartu, 2014, 146 p.
134. **Santa Veikšina**. Development of assay systems for characterisation of ligand binding properties to melanocortin 4 receptors. Tartu, 2014, 151 p.
135. **Jüri Liiv.** PVDF (polyvinylidene difluoride) as material for active element of twisting-ball displays. Tartu, 2014, 111 p.
136. **Kersti Vaarmets.** Electrochemical and physical characterization of pristine and activated molybdenum carbide-derived carbon electrodes for the oxygen electroreduction reaction. Tartu, 2014, 131 p.
137. **Lauri Tõntson**. Regulation of G-protein subtypes by receptors, guanine nucleotides and Mn^{2+}. Tartu, 2014, 105 p.
138. **Aiko Adamson.** Properties of amine-boranes and phosphorus analogues in the gas phase. Tartu, 2014, 78 p.
139. **Elo Kibena**. Electrochemical grafting of glassy carbon, gold, highly oriented pyrolytic graphite and chemical vapour deposition-grown graphene electrodes by diazonium reduction method. Tartu, 2014, 184 p.
140. **Teemu Näykki.** Novel Tools for Water Quality Monitoring – From Field to Laboratory. Tartu, 2014, 202 p.
141. **Karl Kaupmees.** Acidity and basicity in non-aqueous media: importance of solvent properties and purity. Tartu, 2014, 128 p.

142. **Oleg Lebedev**. Hydrazine polyanions: different strategies in the synthesis of heterocycles. Tartu, 2015, 118 p.
143. **Geven Piir.** Environmental risk assessment of chemicals using QSAR methods. Tartu, 2015, 123 p.
144. **Olga Mazina.** Development and application of the biosensor assay for measurements of cyclic adenosine monophosphate in studies of G protein-coupled receptor signalinga. Tartu, 2015, 116 p.
145. **Sandip Ashokrao Kadam.** Anion receptors: synthesis and accurate binding measurements. Tartu, 2015, 116 p.
146. **Indrek Tallo.** Synthesis and characterization of new micro-mesoporous carbide derived carbon materials for high energy and power density electrical double layer capacitors. Tartu, 2015, 148 p.
147. **Heiki Erikson.** Electrochemical reduction of oxygen on nanostructured palladium and gold catalysts. Tartu, 2015, 204 p.
148. **Erik Anderson.** *In situ* Scanning Tunnelling Microscopy studies of the interfacial structure between Bi(111) electrode and a room temperature ionic liquid. Tartu, 2015, 118 p.
149. **Girinath G. Pillai.** Computational Modelling of Diverse Chemical, Biochemical and Biomedical Properties. Tartu, 2015, 140 p.
150. **Piret Pikma.** Interfacial structure and adsorption of organic compounds at Cd(0001) and Sb(111) electrodes from ionic liquid and aqueous electrolytes: an *in situ* STM study. Tartu, 2015, 126 p.
151. **Ganesh babu Manoharan.** Combining chemical and genetic approaches for photoluminescence assays of protein kinases. Tartu, 2016, 126 p.
152. **Carolin Siimenson**. Electrochemical characterization of halide ion adsorption from liquid mixtures at Bi(111) and pyrolytic graphite electrode surface. Tartu, 2016, 110 p.
153. **Asko Laaniste.** Comparison and optimisation of novel mass spectrometry ionisation sources. Tartu, 2016, 156 p.
154. **Hanno Evard.** Estimating limit of detection for mass spectrometric analysis methods. Tartu, 2016, 224 p.
155. **Kadri Ligi.** Characterization and application of protein kinase-responsive organic probes with triplet-singlet energy transfer. Tartu, 2016, 122 p.
156. **Margarita Kagan.** Biosensing penicillins' residues in milk flows. Tartu, 2016, 130 p.
157. **Marie Kriisa.** Development of protein kinase-responsive photoluminescent probes and cellular regulators of protein phosphorylation. Tartu, 2016, 106 p.
158. **Mihkel Vestli.** Ultrasonic spray pyrolysis deposited electrolyte layers for intermediate temperature solid oxide fuel cells. Tartu, 2016, 156 p.
159. **Silver Sepp**. Influence of porosity of the carbide-derived carbon on the properties of the composite electrocatalysts and characteristics of polymer electrolyte fuel cells. Tartu, 2016, 137 p.
160. **Kristjan Haav**. Quantitative relative equilibrium constant measurements in supramolecular chemistry. Tartu, 2017, 158 p.

161. **Anu Teearu**. Development of MALDI-FT-ICR-MS methodology for the analysis of resinous materials. Tartu, 2017, 205 p.
162. **Taavi Ivan**. Bifunctional inhibitors and photoluminescent probes for studies on protein complexes. Tartu, 2017, 140 p.
163. **Maarja-Liisa Oldekop**. Characterization of amino acid derivatization reagents for LC-MS analysis. Tartu, 2017, 147 p.
164. **Kristel Jukk**. Electrochemical reduction of oxygen on platinum- and palladium-based nanocatalysts. Tartu, 2017, 250 p.
165. **Siim Kukk**. Kinetic aspects of interaction between dopamine transporter and *N*-substituted nortropane derivatives. Tartu, 2017, 107 p.
166. **Birgit Viira**. Design and modelling in early drug development in targeting HIV-1 reverse transcriptase and Malaria. Tartu, 2017, 172 p.
167. **Rait Kivi**. Allostery in cAMP dependent protein kinase catalytic subunit. Tartu, 2017, 115 p.
168. **Agnes Heering**. Experimental realization and applications of the unified acidity scale. Tartu, 2017, 123 p.
169. **Delia Juronen**. Biosensing system for the rapid multiplex detection of mastitis-causing pathogens in milk. Tartu, 2018, 85 p.
170. **Hedi Rahnel.** ARC-inhibitors: from reliable biochemical assays to regulators of physiology of cells. Tartu, 2018, 176 p.
171. **Anton Ruzanov.** Computational investigation of the electrical double layer at metal–aqueous solution and metal–ionic liquid interfaces. Tartu, 2018, 129 p.
172. **Katrin Kestav.** Crystal Structure-Guided Development of Bisubstrate-Analogue Inhibitors of Mitotic Protein Kinase Haspin. Tartu, 2018, 166 p.
173. **Mihkel Ilisson.** Synthesis of novel heterocyclic hydrazine derivatives and their conjugates. Tartu, 2018, 101 p.
174. **Anni Allikalt.** Development of assay systems for studying ligand binding to dopamine receptors. Tartu, 2018, 160 p.
175. **Ove Oll.** Electrical double layer structure and energy storage characteristics of ionic liquid based capacitors. Tartu, 2018, 187 p.
176. **Rasmus Palm.** Carbon materials for energy storage applications. Tartu, 2018, 114 p.
177. **Jörgen Metsik.** Preparation and stability of poly(3,4-ethylenedioxythiophene) thin films for transparent electrode applications. Tartu, 2018, 111 p.
178. **Sofja Tšepelevitš.** Experimental studies and modeling of solute-solvent interactions. Tartu, 2018, 109 p.
179. **Märt Lõkov.** Basicity of some nitrogen, phosphorus and carbon bases in acetonitrile. Tartu, 2018, 104 p.
180. **Anton Mastitski**. Preparation of α-aza-amino acid precursors and related compounds by novel methods of reductive one-pot alkylation and direct alkylation. Tartu, 2018, 155 p.
181. **Jürgen Vahter**. Development of bisubstrate inhibitors for protein kinase CK2. Tartu, 2019, 186 p.

182. **Piia Liigand.** Expanding and improving methodology and applications of ionization efficiency measurements. Tartu, 2019, 189 p.
183. **Sigrid Selberg.** Synthesis and properties of lipophilic phosphazene-based indicator molecules. Tartu, 2019, 74 p.
184. **Jaanus Liigand.** Standard substance free quantification for LC/ESI/MS analysis based on the predicted ionization efficiencies. Tartu, 2019, 254 p.
185. **Marek Mooste.** Surface and electrochemical characterisation of aryl film and nanocomposite material modified carbon and metal-based electrodes. Tartu, 2019, 304 p.
186. **Mare Oja.** Experimental investigation and modelling of pH profiles for effective membrane permeability of drug substances. Tartu, 2019, 306 p.
187. **Sajid Hussain.** Electrochemical reduction of oxygen on supported Pt catalysts. Tartu, 2019, 220 p.
188. **Ronald Väli.** Glucose-derived hard carbon electrode materials for sodium-ion batteries. Tartu, 2019, 180 p.
189. **Ester Tee.** Analysis and development of selective synthesis methods of hierarchical micro- and mesoporous carbons. Tartu, 2019, 210 p.
190. **Martin Maide.** Influence of the microstructure and chemical composition of the fuel electrode on the electrochemical performance of reversible solid oxide fuel cell. Tartu, 2020, 144 p.
191. **Edith Viirlaid.** Biosensing Pesticides in Water Samples. Tartu, 2020, 102 p.
192. **Maike Käärik.** Nanoporous carbon: the controlled nanostructure, and structure-property relationships. Tartu, 2020, 162 p.
193. **Artur Gornischeff.** Study of ionization efficiencies for derivatized compounds in LC/ESI/MS and their application for targeted analysis. Tartu, 2020, 124 p.
194. **Reet Link.** Ligand binding, allosteric modulation and constitutive activity of melanocortin-4 receptors. Tartu, 2020, 108 p.
195. **Pilleriin Peets.** Development of instrumental methods for the analysis of textile fibres and dyes. Tartu, 2020, 150 p.
196. **Larisa Ivanova.** Design of active compounds against neurodegenerative diseases. Tartu, 2020, 152 p.
197. **Meelis Härmas.** Impact of activated carbon microstructure and porosity on electrochemical performance of electrical double-layer capacitors. Tartu, 2020, 122 p.
198. **Ruta Hecht.** Novel Eluent Additives for LC-MS Based Bioanalytical Methods. Tartu, 2020, 202 p.
199. **Max Hecht.** Advances in the Development of a Point-of-Care Mass Spectrometer Test. Tartu, 2020, 168 p.
200. **Ida Rahu.** Bromine formation in inorganic bromide/nitrate mixtures and its application for oxidative aromatic bromination. Tartu, 2020, 116 p.
201. **Sander Ratso**. Electrocatalysis of oxygen reduction on non-precious metal catalysts. Tartu, 2020, 371 p.
202. **Astrid Darnell.** Computational design of anion receptors and evaluation of host-guest binding. Tartu, 2021, 150 p.

203. **Ove Korjus.** The development of ceramic fuel electrode for solid oxide cells. Tartu, 2021, 150 p.
204. **Merit Oss.** Ionization efficiency in electrospray ionization source and its relations to compounds' physico-chemical properties. Tartu, 2021, 124 p.
205. **Madis Lüsi**. Electroreduction of oxygen on nanostructured palladium catalysts. Tartu, 2021, 180 p.
206. **Eliise Tammekivi.** Derivatization and quantitative gas-chromatographic analysis of oils. Tartu, 2021, 122 p.
207. **Simona Selberg.** Development of Small-Molecule Regulators of Epitranscriptomic Processes. Tartu, 2021, 122 p.
208. **Olivier Etebe Nonga.** Inhibitors and photoluminescent probes for in vitro studies on protein kinases PKA and PIM. Tartu, 2021, 189 p.
209. **Riinu Härmas.** The structure and H2 diffusion in porous carbide-derived carbon particles. Tartu, 2022, 123 p.